DYNAMICS OF HORIZONTAL AXIS WIND TURBINES AND SYSTEMS WITH
PARAMETRIC STIFFNESS

By

Gizem Dilber Acar

A DISSERTATION

Submitted to
Michigan State University
in partial fulfillment of the requirements
for the degree of

Mechanical Engineering – Doctor of Philosophy

2017

ABSTRACT

DYNAMICS OF HORIZONTAL AXIS WIND TURBINES AND SYSTEMS WITH
PARAMETRIC STIFFNESS

By

Gizem Dilber Acar

The dynamics of a wind turbine blade under bend-bend-twist coupled vibrations is investigated. The potential and kinetic energy expressions for a straight nonuniform blade are written in terms of beam parameters. Then, the energies are expressed in terms of modal coordinates by using the assumed modes method, and the equations of motion are found by applying Lagrange's formula. The bend-bend-twist equations are coupled with each other, and have stiffness variations due to centrifugal effects and gravitational parametric terms which vary cyclicly with the hub angle. To determine the natural frequencies and mode shapes of the system, a modal analysis is applied on the linearized coupled equations of constant angle snapshots of a blade with effects of constant speed rotation. Lower modes of the coupled bend-bend-twist model are dominantly in-plane or out-of-plane modes. To investigate the parametric effects, several blade models are analyzed at different angular positions. The stiffness terms involving centrifugal and gravitational effects can be significant for long blades. To further see the effect of blade length on relative parametric stiffness change, the blade models are scaled in size, and analyzed at constant rotational speeds, at horizontal and vertical orientations.

Blade-hub dynamics of a horizontal-axis wind turbine is also studied. Blade equations are coupled through the hub equation, and have parametric terms due to cyclic aerodynamic forces, centrifugal effects and gravitational forces. The modal inertia of a single blade is defined by the linear mass density times the square of transverse displacements from blade's undeflected axis. For reasonable transverse displacements, the modal inertia of a blade is usually small compared to the rotor inertia which is the combined inertia of the hub plus

all three blades about the shaft. This enables us to treat the effect of blade motion as a perturbation on the rotor motion. The rotor speed is not constant, and the cyclic variations cannot be expressed as explicit functions of time. By casting the rotor angle as the independent variable, and assuming small variations in rotor speed, the leading order blade equations are decoupled from the rotor equation. The interdependent blade equations constitute a three-degree-of-freedom system with periodic parametric and direct excitation. The response is analyzed by using the method of multiple scales. The system has superharmonic and subharmonic resonances due to direct and parametric effects introduced by gravity. Amplitude-frequency relations and stabilities of these resonances are studied.

The Mathieu equation represents the transient dynamics of a single-mode blade model. Approximate solutions to the linear unforced Mathieu equation, and their stabilities, are investigated. Floquet theory shows that the solution can be written as a product between an exponential part and a periodic part at the same frequency or half the frequency of excitation. An approach combining Floquet theory with the harmonic balance method is investigated. A Floquet solution having an exponential part with an unknown exponential argument and a periodic part consisting of a truncated series of harmonics is assumed. Then, performing harmonic balance, the Floquet exponents and and harmonic coefficients are found. From this frequencies of the response and stability of the solution are determined. The truncated solution is consistent with an existing infinite series solution for the undamped case. The truncated solution is then applied to the damped Mathieu equation and to parametric excitation with two harmonics.

Solutions and stability of multi-degree-of-freedom Mathieu-type systems are also investigated. A procedure similar to the one applied for the Mathieu equation is used to find the initial conditions response, frequency content, and stability characteristics. The approach is applied to two- and three-degrees-of-freedom examples. For a few parameter sets, the results obtained from this method are compared to the numerical solutions. This study provides a framework for a transient analysis of three-blade turbine equations.

ACKNOWLEDGMENTS

the pursuit of the PhD and this journey in life. I would not be the same person if I did not meet you. No matter how far from home I am, to me, home is right where you are.

I would like to thank my family, who always supported me in my decisions. Sinem and Enes are not just my siblings, but also two of my best friends, and no distance can change this. I also thank my mom, for being the most warm-hearted and least judgmental mom there is. I would not accomplish any of these without her and my siblings' support.

Finally thanks to everyone who I chatted with about research, science and life, who I made paintings with, who I shared a beer with, who touched my life one way or the other. Really, thank you!

TABLE OF CONTENTS

viii

LIST OF TABLES

LIST OF FIGURES

1.1 Motivation and Objectives

Through the past few decades, wind power has attracted considerable attention as a renew-able energy source. In 2015, wind energy comprised 4.7% of the electricity production in the U.S. [5]. The Department of Energy has studied scenarios where the aim is to increase the wind energy's share in electricity production to 20% by 2030, and to 35% by 2050 [1, 6], as shown in Figure 1.1. As the global energy industry has started to invest in wind power as a clean energy source, research on wind turbines has been of great importance. Since the installation and maintenance costs are significant, efforts have been made on reliable designs for wind turbine parts.
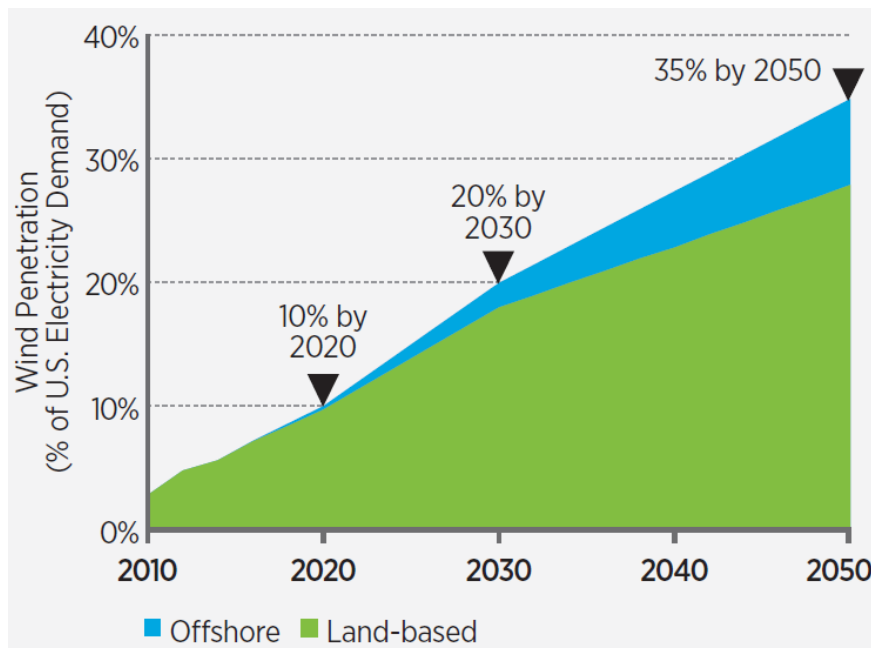
Figure 1.1 Wind energy's share in electricity production in the U.S. [1]

The amount of energy produced by a wind turbine is proportional to the area swept by

its blades, and hence larger blade designs have become more popular recently. The Dutch Offshore Wind Energy Project has a blade design with 62.6 m, The National Renewable Energy Laboratory (NREL) has a model of 61.5 m blade for a turbine with a 5 MW capacity, and Sandia National Laboratory (SNL) has a design for a 100 m blade for a turbine with a 13.2 MW capacity [7–9]. However, long blade designs come along with dynamical problems. The gravitational force and centrifugal effects induce variations in blade stiffness, which can be significant for long blades. Also the blade vibrations have coupling between in-plane, out-of-plane and torsional directions, although they have usually been considered separately in industrial applications. These considerations are the motivation behind the wind turbine blade research.

In horizontal-axis wind turbines failure usually takes place in the hub and gearbox. To describe the loadings induced by the blades on the hub, it is important to study the blade dynamics. Then, the interactions between the blades and rotor need to be investigated. Blades apply inertial and parametric loads on the rotor, which are transmitted to each other through the hub. These effects induce parametric and direct secondary resonances in the blades, even when the model is linear. So, even for a simple scenario, the coupled dynamics of blades and the hub is an interesting research problem.

Because of the dynamic variations in the blade stiffness, the blade equations are similar to a forced Mathieu equation. Solutions to the Mathieu equation are therefore of great importance since they apply to the transient dynamics of the blades. Also, three-blade and hub turbine equations can be considered as a multi-degree-of-freedom (MDOF) system with parametric stiffness. The transient dynamics of the single-blade equations and the three-blade turbine equations motivated the study of the general responses of the Mathieu equation and MDOF systems with parametric stiffness, respectively.

Modeling the aerodynamic forces on a turbine blade is important for a complete understanding of forced turbine dynamics. Due to oscillations in the blades, dynamic stall might occur when the blades operate at high angles of attack. An extensive review is done on

existing aerodynamic stall models in order to understand the nature of the external forces on the blades. However application of these models are not included in this thesis.

These motivating issues lead to the objectives of this study, which are

- To model the blade as a beam under bend-bend-twist vibrations, and study its modal dynamics to estimate the degree of coupling between in-plane and out-of-plane vibrations, and to find the importance of the parametric gravitational and centrifugal effects,

- To investigate the interaction between blades and their dynamical effects on the hub, and to determine the secondary resonances in the blades by using a perturbation method,

- To study the general responses of the Mathieu equation to gain insight to the transient dynamics of a single blade,

- To find the general responses of MDOF systems with parametric stiffness to build a framework for the transient dynamics of a three-blade turbine,

- To review the aerodynamic stall models which can represent the aeroelastic loading at high angles of attack, and under unsteady oscillatory conditions.

1.2   Background and Literature Review

1.2.1   Bend-Bend-Twist Vibrations of a Wind Turbine Blade

Vibrational analysis of a wind turbine blade plays an important role in turbine design. In horizontal-axis wind turbines failure often takes place in the hub and gearbox [10]. The cyclic loads applied by the blades are thought to play a large role. To prevent failure and make improvements in turbine design, dynamics of the blades must be investigated.

Blades are under cyclic loading due to turbine rotation. A steady wind speed usually varies with altitude, so as the blade rotates with the hub its altitude varies, and so it is affected by a cyclicly varying amount of wind force. Also the tangential and radial components of gravity force vary cyclicly, changing the effective stiffness of the blade as the hub rotates. These effects introduce parametric terms into the equations of motion.

A blade under bend-bend-twist deformation is shown in Figure 1.2. The deformation in $\hat{y}$ direction is called in-plane (edgewise) bending, whereas the deformation in $\hat{z}$ is called out-of-plane (flapwise) bending. For practical reasons, the blade vibrations are usually investigated in flapwise and edgewise directions separately [8, 11, 12]. These two directions are uncoupled only when the product moment of inertia of a blade cross-section is zero. Yet, for a general airfoil cross-section, it is not zero, which introduces coupling between two bending directions. Dawson [13] studied bend-bend coupled vibrations in pre-twisted beams, and formulated natural frequencies using energy methods. Torsional vibrations are also coupled with bending vibrations for most blades [14–16]. Dokumaci [14] derived the torsion-bending coupled equations analytically, and Bishop *et al.* [15] improved the theory by introducing warping. Cooley and Parker [17] also worked on bend-twist coupled vibration of spinning beams, taking the centrifugal effects into account. Hodges and Dowell [18] found the equations of motion for a blade going under bend-bend-twist motion with a structural twist. Since they worked on a helicopter blade, they did not take the effects of gravity and varying rotor speed into account. Kallesøe [19] used Hodges and Dowell's equations for a turbine blade, adding the effects of gravity and pitching motion. He neglected shear center being offset from the mass center, and shaft tilt and precone.

Wind turbines have been studied through experimental and numerical modal analyses, and finite element method [20–24]. Larsen *et al.* [20] explained a procedure for an experimental modal analysis where each cross-section is modeled with three-degrees-of-freedom and the blade is excited with an impact hammer. Hansen [23] used the HAWCStab simulation tool, where the blade structure is modeled with finite element method and the aeroelastic forces
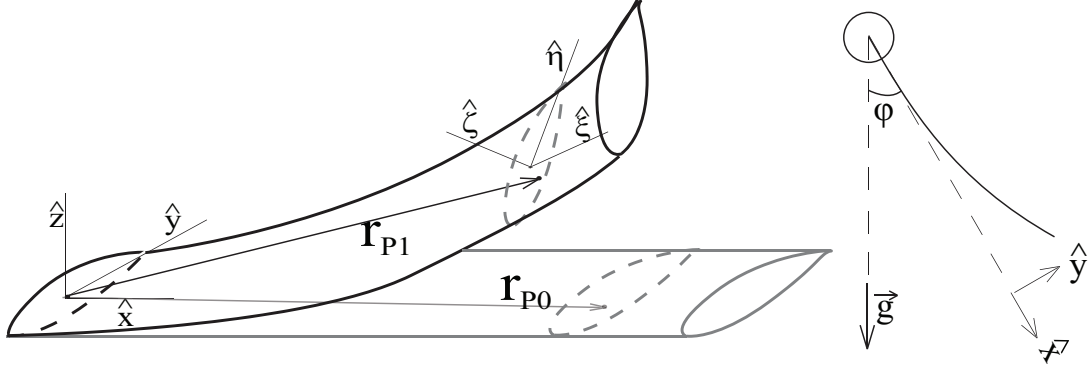
Figure 1.2 Blade under bend-bend-twist deformation.

are modeled with blade element momentum method, to conduct an eigenanalysis to find the aerodynamic stability of a turbine. Bir [24] applied multiblade coordinate transformation method to NREL's 5 MW turbine to find its frequencies.

Crespo da Silva [25] developed a model for beams under bend-bend-twist vibration. Neglecting the parametric effects of gravity, he derived the equations of motion using Hamilton's principle. In Chapter 2, a similar approach is given in detail, where instead of Hamilton's principle, Lagrange's method is used to find the equations of motion, and the modal dynamics of the blade are investigated as well as the parametric effects.

1.2.2   In-Plane Dynamics of a Three Blade Turbine

In Chapter 3, in-plane vibration equations are derived for a three-blade turbine. The blade equations are coupled through the rotor equation, and the modal mass in the blade equation is small compared to the inertia term in the rotor equation. These equations are similar to centrifugal pendulum vibration absorber equations, where the absorber inertia is small compared to the rotor inertia [26, 27].

The blade and rotor equations are coupled through the inertial terms. Using the Fourier matrix explained in Olson *et al.*'s work [28], the coupling can be transferred to the stiffness terms through a coordinate transformation. Then, one can apply the method of averaging to study the steady-state dynamics. In order to decouple the absorber equations from the rotor

equation, Chao *et al.* [29,30] used rotor angle as the independent variable, instead of time, and used a scaling scheme where the absorber motion is considered as small perturbations to the rotor equation. Also, Theisen [31] investigated the effects of gravity on absorber motion, and internal resonances associated with it. A similar approach is used in Chapter 3 in order to investigate the three-blade turbine dynamics, and the resonances introduced by the parametric effects.

1.2.3 The Mathieu Equation and MDOF Systems with Parametric Stiffness

Horizontal-axis wind-turbine blade equations under constant rotation rates have parametric stiffness terms due to gravity [32,33]. Therefore solutions to equations with parametric excitation are important to understand the transient and steady-state dynamics of the blades.

Numerous mechanical systems have parametric terms, such as swings, base-excited pendulums and ship roll [32,34–36]. Parametrically excited systems such as the Mathieu equation have been studied using a variety of methods. Floquet theory has been invoked to provide stability criteria, as discussed in more detail in Chapter 4. Perturbation methods have also been used to approximate the solutions to the undamped and damped Mathieu equations, as well as the forced and unforced Mathieu equations [32,34,37–45]. These include the application of second-order multiple scales [32], and the method of van der Pol [34] to determine stability characteristics, and the use of averaging [37], multiple scales [38], and harmonic balance [46] to analyze forced Mathieu equations. Ecker [47,48] worked on parametrically excited vibration absorbers which are represented by a Mathieu-type equation. He used numerical integration to solve for the monodromy matrix and its eigenvalues to find the stability characteristics of the system. Rand [45] found an expression for stability transition curves of a Mathieu-type system with three harmonics by applying a perturbation analysis, whereas Klotter and Kotowski [49] used Hill's method to investigate stability of a parametrically excited system with two harmonics. Sofroniou and Bishop [50] worked on a more generic equation with periodic and quasi-periodic excitation, and investigated bifurcation

characteristics. System identification methods have been used to investigate the response characteristics of the time-periodic systems. Allen *et al.* [51] used an output-only system identification method to find the Floquet exponents and the modal functions of the damped Mathieu equation.

According to Floquet theory, solutions to the Mathieu equation are composed of an exponential part and a periodic part [52]. An analysis of the Floquet-type solution suggests that the response can be (i) quasi-periodic, (ii) periodic, or (iii) unstable. As the system parameters vary, the solution can travel between the quasi-periodic and unstable zones, and at the transitions, it is periodic [53]. Therefore the stability boundaries can be found by assuming a periodic solution [46, 54–56]. However this approach does not provide the response itself. In Chapter 4, instead of assuming a periodic solution, the Floquet-type solution is kept as is, and harmonic balance method is applied. This approach is presented to approximate the general responses to the undamped, damped and two-harmonic excitation Mathieu equations, as well as the stability of the solutions.

The approach followed in the Mathieu problem is extended to multi-degree-of-freedom systems with parametric stiffness in order to find the solutions and the stabilities. This study can be applied to three-blade turbine equations in order to understand the transient dynamics of the turbine.

1.2.4 Aerodynamic Stall

The aerodynamic loads depend on the angle of attack, that is the angle between the relative wind speed and the airfoil cross-section, as shown in Figure 1.3. For small angles, the lift force increases with the angle of attack in a linear-like fashion. However around a critical angle (i.e. stall angle), the lift force drops suddenly. This phenomenon is called aerodynamic stall [57, 58].

When the angle of attack varies slowly, a quasi static aerodynamic load can be modeled, where the lift force is a direct function of angle of attack. However, when the angle of attack
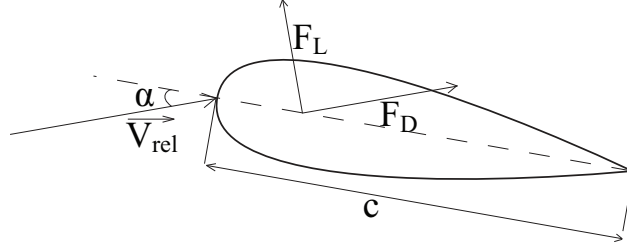
Figure 1.3 An airfoil cross-section.

oscillates, the airfoil might go under dynamic loading, where the lift force is much more complicated and affected by the dynamics of the angle of attack. In dynamic stall, there is a hysteresis in lift the force curve during increasing and decreasing angles of attack [2, 59].

Lift force on an airfoil has been studied many researchers [2, 4, 60–63]. Theodorsen [60] explained a method using potential flow and Kutta condition to determine the aerodynamic forces and moments, and to study flutter conditions. Peters *et al.* [62] developed a theory where the time history of the circulatory lift is treated as a feedback induced flow on the blade. Also vortex lattice method, where the airfoil is divided into a finite number of elements with a vortex, can be used to calculate the lift force numerically [61].

The lift function can be modeled via semi-empirical methods, where the dynamics of the function is modeled with differential equations, parameters of which are estimated experimentally [2, 4, 63]. In Appendix C, ONERA's and Larsen *et al.*'s semi-empirical dynamic stall models are reviewed in detail.

1.3   Thesis Overview

This thesis contains modeling of a single wind-turbine blade under bend-bend-twist vibrations, and derivation of equations of motion using Lagrange's method together with assumed modes. A linear modal analysis is shown to find the modal frequencies as well as the mode shapes of the blade. Blade stiffness varies with the rotor angle due to parametric effects of gravity, which are more significant for long blades. An analysis on the effect of length on

the parametric stiffness is provided.

Then a three-blade turbine model which represents the coupled blade-hub dynamics is studied. Only in-plane bending vibrations are taken into account, and a single cantilever beam mode is assumed for each blade. The linearized blade and rotor equations are coupled with each other in the time domain. To decouple the rotor equation from the blade equations, the independent variable is transformed from time to rotor angle, and a scaling scheme and a nondimensionalization procedure are followed. The method of multiple scales is applied to explore the effects of the parametric stiffness on the blade response.

This thesis presents an analytical approach for approximating the general responses of the Mathieu equation. A general non-periodic Floquet-type solution is assumed, and the frequency content and the stability of the solution are determined via the harmonic balance method. General responses are constructed by using the characteristic exponents and Fourier coefficients found through the harmonic balance. An extension of the approach to MDOF systems with parametric stiffness is also provided. The results of both the SDOF and the MDOF examples are verified through simulations. This method can be used to approximate the transient response of parametrically excited turbine equations.

Lastly, an extensive review on aerodynamic modeling of the lift force is given. The variations in angle of the relative wind speed during blade oscillations can introduce dynamic stall, where the lift force drops dramatically, and cause hysteresis in the lift force. This phenomenon can be modeled by semi-empirical methods, where the parameters in the mathematical models are determined experimentally. A comprehensive review of two of the existing semi-empirical methods are given. These methods can be used to build a framework for a forced turbine model.

1.4 Contributions

The contributions of this thesis to the literature are:

- The energies of slender nonuniform pretwisted blade are formulated for bend-bend-twist vibration, and are presented in terms of familiar beam parameters.

- The modal equations of motion are found for a blade under bend-bend-twist vibration, and the frequencies and mode shapes are found by applying a modal analysis. It is shown that the degree of coupling between in-plane and out-of-plane vibrations depend on the beam parameters.

- The parametric and the centrifugal effects in blade stiffness are investigated. The stiffness variations are found to be more serious for longer blades.

- In-plane equations of motion for a three-blade turbine are derived. The secondary resonances introduced by the direct and the parametric effects are investigated.

- An approach is developed to determine approximate general responses to the undamped, damped and two-harmonic excitation Mathieu equations. The approach allows us to determine the response frequency content and damping rate, and can be applied to other linear second order differential equations with periodic coefficients. The approach is also extended to MDOF systems with parametric stiffness.

CHAPTER 2

EQUATIONS OF MOTION OF A BLADE UNDER BEND-BEND-TWIST VIBRATIONS

2.1 Introduction

A horizontal axis wind turbine blade is considered as a cantilever beam under bend-bend-twist coupled vibration, rotating at a constant speed. The kinetic and strain energies are formulated by the help of Crespo da Silva's method [25]. Given the energy expressions, Crespo da Silva then used Hamilton's principle to find the partial differential equations of motion of a beam with no gravitational loading. Instead, in this study, the assumed modes method is used. First the energy expressions are written in terms of assumed modal coordinates, and the equations of motion are derived by Lagrange's method applied to the assumed modal coordinates. Under steady rotational effects, the equations have parametric terms involving the hub angle and the angular speed. The gravity introduces periodic stiffness terms, which leads to a forced Mathieu equation in a single mode model [32], and the angular speed leads to an increase in stiffness [64, 65].

In this chapter the structural modal dynamics are studied, separate from the dynamic effects of the parametric terms. As such, the equations are linearized and modal analysis is applied to find the modal frequencies and mode shapes. The mode shapes are composed of bend-bend-twist deformations, and the degree of coupling depends on system parameters, such as the degree of structural twist and the product moment of inertia of the cross-section.

The goal of this study is to gain insight on three aspects of the structural modal behavior. The aim is to examine mode shapes to evaluate the industry's distinction between flapwise and edgewise modes, quantify the effect of angular rotor speed on the modal frequencies, and study the variation in effective stiffness with varying rotor angle position, as it will

11

contribute to parametric excitations under conditions of steady rotation. To demonstrate
the strength of the parametric terms, existing blade models are analyzed at different hub
angles, rotating with different speeds. In order to investigate the relations between the blade
size and the significance of the parametric effects, existing blade models are scaled in volume,
by keeping their shape the same. The downward/upright frequency ratios are investigated
for the scaled models, and found to be increasing almost linearly with the blade size. As
a separate study the blade models are scaled in length only, by keeping their thickness the
same, and the frequency ratios are estimated as a function of length. These studies show that
the parametric effects become more important as the horizontal axis wind turbine blades get
larger.

2.2 Methodology

The wind turbine blade is modeled as a straight beam with a varying cross-section, under
bend-bend-twist coupled deformation, as shown in Figure 2.1. The coordinate system $(\hat{x}, \hat{y}, \hat{z})$
is fixed to the undeformed blade at the fixed end with its origin at an arbitrary point, whereas
$(\hat{\xi}, \hat{\eta}, \hat{\zeta})$ is fixed to a cross-section in the deformed blade. The position vector to the origin
of $(\hat{\xi}, \hat{\eta}, \hat{\zeta})$ is $\mathbf{r}_0 = x\hat{x}$ before deformation.
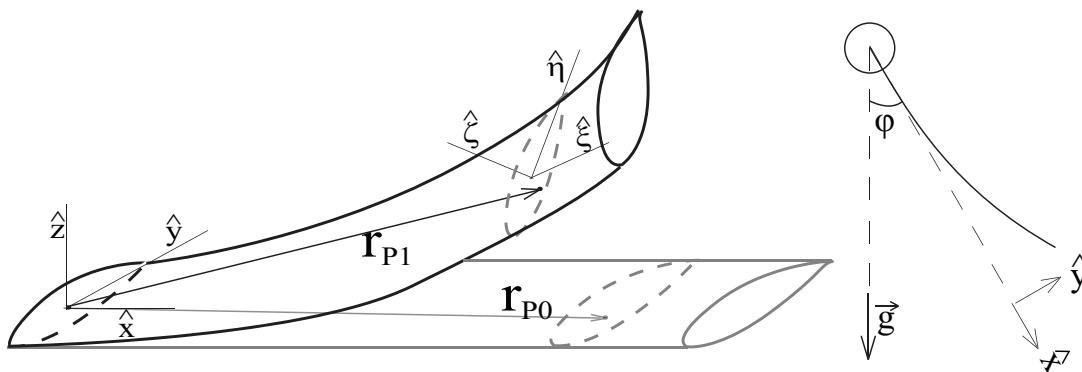
Figure 2.1 Coordinate systems in the deformed and undeformed blade.

The combined motion is modeled as three translational and three rotational displace-

12

ments: u, v, w are the translational, and θ_x, θ_y, θ_z are the rotational displacements in $\hat{x}$, $\hat{y}$ and $\hat{z}$ directions, respectively. The cross-section of the blade is assumed to remain planar, and the displacements are functions of x and t only. v and w are bending deflections in in-plane and out-of-plane directions, and θ_y and θ_z are the corresponding slopes, so they can be written in terms of v and w. The position vector to the origin of $(\hat{\xi}, \hat{\eta}, \hat{\zeta})$ is $\mathbf{r}_1 = x\hat{x} + v\hat{y} + w\hat{z}$ after deformation.

The beam is assumed to be inextensible, which means the axial deflection, u, is only due to the foreshortening of bending motion. Its slope can be expressed through derivatives of v and w as

$$u' = 1 - \sqrt{1 - v'^2 - w'^2},\tag{2.1}$$

where $(\ )'$ denotes the partial derivative with respect to x.

2.2.1 Energy Formulations

The strain energy is formulated in terms of the deformations v, w and θ_x, and their spatial derivatives, by using the relations in Crespo da Silva's study [25]. The strain energy density at an arbitrary point is found first, and then the total strain energy is calculated by integrating the energy density through the volume. To find the strain energy density, the strain and stress distributions are found through the displacements. The position of an arbitrary point P before deformation is written as $\mathbf{r}_{P0} = x\hat{x} + \eta\hat{y} + \zeta\hat{z}$, whereas it is given as $\mathbf{r}_{P1} = (x+u)\hat{x} + v\hat{y} + w\hat{z} + \eta\hat{\eta} + \zeta\hat{\zeta}$ after deformation. It is convenient to express $\mathbf{r}_{P1}$ in the $(\hat{x}, \hat{y}, \hat{z})$ coordinate system. Transformation from $(\hat{\xi}, \hat{\eta}, \hat{\zeta})$ to $(\hat{x}, \hat{y}, \hat{z})$ can be written in terms of the rotations as $\hat{\eta} = \hat{y} + \theta_x\hat{z} - v'\hat{x}$ and $\hat{\zeta} = \hat{z} - \theta_x\hat{y} - w'\hat{x}$. Therefore $\mathbf{r}_{P1}$ can be written as $\mathbf{r}_{P1} = (x + u - \eta v' - \zeta w')\hat{x} + (v + \eta - \zeta\theta_x)\hat{y} + (w + \zeta + \eta\theta_x)\hat{z}$.

Using Green's formula the strain state at a point can be written in terms of $\mathbf{r}_{P0}$ and

$\mathbf{r}_{P1}$ [66, 67], as

$$2 \begin{pmatrix} dx & d\eta & d\zeta \end{pmatrix} (\boldsymbol{\varepsilon}) \begin{pmatrix} dx \\ d\eta \\ d\zeta \end{pmatrix} = d\mathbf{r}_{P1} \cdot d\mathbf{r}_{P1} - d\mathbf{r}_{P0} \cdot d\mathbf{r}_{P0}, \tag{2.2}$$

where $\boldsymbol{\varepsilon}$ is the Lagrangian strain tensor. Strain components are expressed up to quadratic terms in Appendix A.1. The stress distribution is found using Hooke's law, $\sigma_{ij} = C_{ijkl}\varepsilon_{kl}$, where $\varepsilon_{kl} = \frac{1}{2}\gamma_{kl}$ (for $k \neq l$) with shear strains γ_{kl}. The strain energy is expressed with the following volume integral [68]:

$$U = \frac{1}{2} \int_V \left(\sigma_{xx}\varepsilon_{xx} + \sigma_{\eta\eta}\varepsilon_{\eta\eta} + \sigma_{\zeta\zeta}\varepsilon_{\zeta\zeta} + \sigma_{x\eta}\gamma_{x\eta} + \sigma_{x\zeta}\gamma_{x\zeta} + \sigma_{\eta\zeta}\gamma_{\eta\zeta} \right) dV. \tag{2.3}$$

Note that the strain components $\varepsilon_{\eta\eta}$, $\varepsilon_{\zeta\zeta}$ and $\gamma_{\eta\zeta}$ have only quadratic terms, as shown in Appendix A.1, and hence they do not appear in the strain energy expression of the linear model.

The kinetic energy of the blade can be written as

$$T = \frac{1}{2} \int_V (\mathbf{v}_{P1} \cdot \mathbf{v}_{P1}) \, dm, \tag{2.4}$$

where $\mathbf{v}_{P1} = \dot{\mathbf{r}}_{P1} + \dot{\phi}\hat{z} \times \mathbf{r}_{P1}$. The first term corresponds to the derivative of $\mathbf{r}_{P1}$ with respect to time, written in the rotating $(\hat{x}, \hat{y}, \hat{z})$ coordinates, and the second term stands for the rotation of the coordinate system.

The gravitational potential energy can be written as

$$V_g = \int_V -\mathbf{r}_{P1} \cdot \mathbf{g} \, dm. \tag{2.5}$$

Since $\mathbf{r}_{P1}$ is given in $(\hat{x}, \hat{y}, \hat{z})$ coordinates, the gravity vector is also written in the same coordinates, $\mathbf{g} = \mathrm{g}(\cos\phi\hat{x} - \sin\phi\hat{y})$, where ϕ is the rotor angle, such that $\phi = 0$ when the blade is in downward position, as shown in Figure 2.1. Therefore the effect of gravity changes with the rotor angle which results in cyclic changes in the blade stiffness.

All three energy expressions are volume integrals, the calculations of which are not straightforward. Yet they can be reduced to an area integral inside an integral along the

14

length. Since the cross section is assumed to be planar (no warping assumed) with shearing only due to θ_x, the deflections are functions of x only (independent of η and ζ), and they can be pulled out from the area integrals (e.g. $\int_V \left(\dot{w}(x,t)\,\eta^2\right) dV$ can be written as $\int_0^L \int_A \left(\dot{w}(x,t)\,\eta^2\right) dA\,dx = \int_0^L \dot{w}(x,t) \int_A \eta^2\,dA\,dx$). Then, the area integrals are left with terms involving η and ζ only, as given below:

$$\int_A dA = A, \quad \int_A \eta dA = \eta_0 A, \quad \int_A \zeta dA = \zeta_0 A,$$
$$\int_A \eta^2 dA = I_{\zeta\zeta} + \eta_0^2 A, \quad \int_A \zeta^2 dA = I_{\eta\eta} + \zeta_0^2 A, \quad \int_A \eta\zeta dA = I_{\eta\zeta} + \eta_0\zeta_0 A,$$

where $I_{\eta\eta}$, $I_{\eta\zeta}$, $I_{\zeta\zeta}$ are second moments of area about the centroid, and η_0 and ζ_0 are components of the offset of the origin of the coordinate system (O) from the centroid (C), as shown in Figure 2.2. Fixing the origin to the centroid (i.e. $\eta_0 = 0, \zeta_0 = 0$) greatly simplifies these expressions. The resulting potential and kinetic energies are given for a linear model in Appendix A.2 for the centroid-based coordinate system.
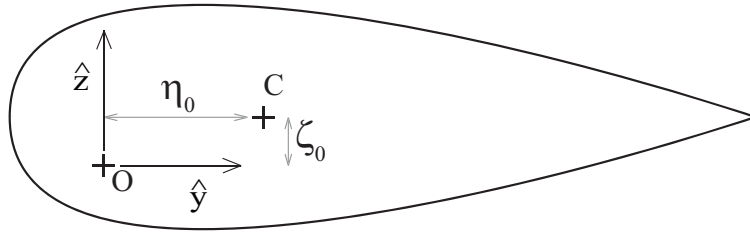
Figure 2.2 Blade cross-section before deformation.

A shear force applied on a cross-section creates a torsional moment if the force is not applied at the shear center. For most airfoil cross-sections, the shear center is offset from the centroid. Therefore, one might wish to write the energy expressions for the shear center displacements. When written in terms of shear center deflections, kinetic and potential energies have a few extra terms involving the offset from the centroid, as shown in Appendix A.2. These terms lead to torsion-bending coupling in the kinetic and gravitational potential energies even when the rotor is non-rotating (i.e. $\dot{\phi} = 0$), whereas centroid based energy formulations do not have torsion-bending coupling when $\dot{\phi} = 0$. The shear center based

energy formulations were consistent with those in Weaver *et al.*'s study on coupled in-plane flexural and torsional vibrations for non-rotating beam ($\dot{\phi} = 0$) [69].

2.2.2 Assumed Modes and Equations of Motion

In order to derive the equations of motion, energy expressions are written in terms of modal coordinates by using the "assumed modes" method, in which the displacements are expanded in terms of spatial trial functions [70]. The deflections, v, w and θ_x, are written as

$$v(x,t) = \sum_{i=1}^{n} \gamma_{vi}(x) q_{vi}(t), \quad w(x,t) = \sum_{i=1}^{n} \gamma_{wi}(x) q_{wi}(t), \quad \theta_x(x,t) = \sum_{i=1}^{n} \gamma_{\theta i}(x) q_{\theta i}(t),$$

where $\gamma_{ji}(x)$'s are assumed modes or trial functions, $q_{ji}(t)$'s are modal coordinates and n is the number of assumed modes in each coordinate. For each displacement, cantilever beam modes are assumed, such that

$$\gamma_{vi}(x) = \cosh\left(k_i \frac{x}{l}\right) - \cos\left(k_i \frac{x}{l}\right) - r_i \left(\sinh\left(k_i \frac{x}{l}\right) - \sin\left(k_i \frac{x}{l}\right)\right), \tag{2.6}$$

$$\gamma_{wi}(x) = \cosh\left(k_i \frac{x}{l}\right) - \cos\left(k_i \frac{x}{l}\right) - r_i \left(\sinh\left(k_i \frac{x}{l}\right) - \sin\left(k_i \frac{x}{l}\right)\right), \tag{2.7}$$

$$\gamma_{\theta i}(x) = \sin\frac{x\pi}{2l}. \tag{2.8}$$

The deflections are written in terms of assumed modes and inserted into the energy expressions. The Lagrangian is found in terms of the modal coordinates, and then, the equations of motion are found by applying Lagrange's equations to the modal coordinates.

For the case of only one assumed mode in each direction, the equations of motion are given in Appendix A.3. For most airfoil cross-sections, the product moments of area and inertia ($I_{\eta\zeta}, J_{\eta\zeta}$) are nonzero, and this leads to a coupling between the q_v and q_w equations. Furthermore the torsion equation is coupled with the bending equations through the gyroscopic terms.

2.2.3 Modal Analysis

The equations of motion are put into matrix form, given as

$$
\begin{bmatrix} \mathbf{M}_{vv} & \mathbf{M}_{vw} & \mathbf{0} \\ \mathbf{M}_{vw} & \mathbf{M}_{ww} & \mathbf{0} \\ \mathbf{0} & \mathbf{0} & \mathbf{M}_{\theta\theta} \end{bmatrix} \begin{pmatrix} \ddot{\mathbf{q}}_v \\ \ddot{\mathbf{q}}_w \\ \ddot{\mathbf{q}}_\theta \end{pmatrix} + \begin{bmatrix} \mathbf{0} & \mathbf{0} & -\mathbf{G}_{v\theta} \\ \mathbf{0} & \mathbf{0} & -\mathbf{G}_{w\theta} \\ \mathbf{G}_{v\theta} & \mathbf{G}_{w\theta} & \mathbf{0} \end{bmatrix} \begin{pmatrix} \dot{\mathbf{q}}_v \\ \dot{\mathbf{q}}_w \\ \dot{\mathbf{q}}_\theta \end{pmatrix}
$$
$$
+ \begin{bmatrix} \mathbf{K}_{vv} & \mathbf{K}_{vw} & \mathbf{0} \\ \mathbf{K}_{vw} & \mathbf{K}_{ww} & \mathbf{0} \\ \mathbf{0} & \mathbf{0} & \mathbf{K}_{\theta\theta} \end{bmatrix} \begin{pmatrix} \mathbf{q}_v \\ \mathbf{q}_w \\ \mathbf{q}_\theta \end{pmatrix} = \begin{pmatrix} \mathbf{Q}_v \\ \mathbf{Q}_w \\ \mathbf{Q}_\theta \end{pmatrix}, \quad (2.9)
$$

where $\mathbf{q}_i$'s are vectors consisting assumed modal coordinates, $\mathbf{Q}_i$'s are corresponding generalized forcing terms, and $\mathbf{M}_{ij}$, $\mathbf{G}_{ij}$ and $\mathbf{K}_{ij}$ are block matrices denoting coupling between coordinates i and j. The mass matrix is a constant matrix whereas $\mathbf{G}_{ij}$'s contain $\dot{\phi}$ and the stiffness matrix has parametric terms involving ϕ and $\dot{\phi}$. For a system with parametric stiffness, finding the natural frequencies and mode shapes is not straightforward. Parametrically excited systems with direct forcing have been studied using various perturbation methods, including an application of second order multiple scales [71], averaging [37], the method of van der Pol [34], harmonic balance [46] and system identification methods [51]. In this chapter, modal response of a single blade is studied, and instead of working on dynamic effects of parametric terms, the homogeneous system is solved assuming steady conditions. The aim is to see whether the parametric terms may be strong enough to risk the parametric resonances uncovered in the previous works, and also to evaluate the distinction between flapwise and edgewise modes. A modal analysis is applied to different angle snapshots of a blade rotating at a constant speed in order to find its natural frequencies and mode shapes.

The generalized forces $\mathbf{Q}_i$ accommodate aeroelastic loading and damping terms. Although these are important for the operation of the wind turbine, we do not treat their details for this modal analysis work. The equation of motion with aeroelastic and gravita-

tional loads is considered to be of the form $\mathbf{M\ddot{q}} + \mathbf{G\dot{q}} + \mathbf{Kq} = \mathbf{Q}_g(\phi) + \mathbf{Q}_0 + \epsilon\mathbf{Q}_1(\mathbf{q}, \dot{\mathbf{q}})$, such that the aerodynamics is dominated by mean load $\mathbf{Q}_0$ and has a small variation, in which the cyclic variation is neglected. One can consider an equilibrium deflection such that $\mathbf{Kq}_0 = \mathbf{Q}_g(\phi) + \mathbf{Q}_0 + \epsilon\mathbf{Q}_1(\mathbf{q}_0)$. Applying a small deformation $\mathbf{q}_1$ about equilibrium, such that $\mathbf{q} = \mathbf{q}_0 + \mathbf{q}_1$, the equation of motion becomes $\mathbf{M\ddot{q}}_1 + \mathbf{G\dot{q}}_1 + \mathbf{Kq}_0 + \mathbf{Kq}_1 = \mathbf{Q}_g(\phi) + \mathbf{Q}_0 + \epsilon(\mathbf{Q}_1(\mathbf{q}_0) + \mathbf{q}_1 \frac{\partial\mathbf{Q}_1}{\partial q}(\mathbf{q}_0))$. Then, the first approximation is $\mathbf{M\ddot{q}}_1 + \mathbf{G\dot{q}}_1 + \mathbf{Kq}_1 \approx 0$. As such, a modal analysis is performed based on the structural model in Equation (2.9).

2.3 Results

The modal analysis explained in the previous section is first applied to a hollow, pre-twisted beam to find the natural frequencies and mode shapes. A finite element analysis is also conducted on the same beam, to verify the method developed. Then, the analytical method is applied to existing blade models, and the results are compared to those found in the literature. The modal analysis is conducted for different hub angles and rotor speeds, and the effects of these parameters are investigated.

2.3.1 A Hollow Rectangular Beam with a Structural Twist

A pre-twisted beam with a hollow rectangular cross-section, as shown in Figure 2.3, was analyzed. The beam has dimensions 3 m $\times$ 1.5 m $\times$ 50 m with 0.2 m thickness, and structural twist angle changing linearly with axial position, given by the relation $\beta(x) = \frac{\pi x}{3l}$. The material is assumed to be linearly elastic and isotropic, having Young's modulus $E = 40$ GPa, Poisson's ratio $\nu = 0.3$, and mass density $\rho = 2500$ kg/m^3.

The modal analysis is applied to beam in horizontal and vertical positions, by assuming static conditions, such that $\dot{\phi} = 0$ and $\phi = \phi_0$. The first two natural frequencies and mode shapes were found by assuming up to four modes in each direction (Table 2.1). As the number of assumed modes is increased, the natural frequencies approached convergence to
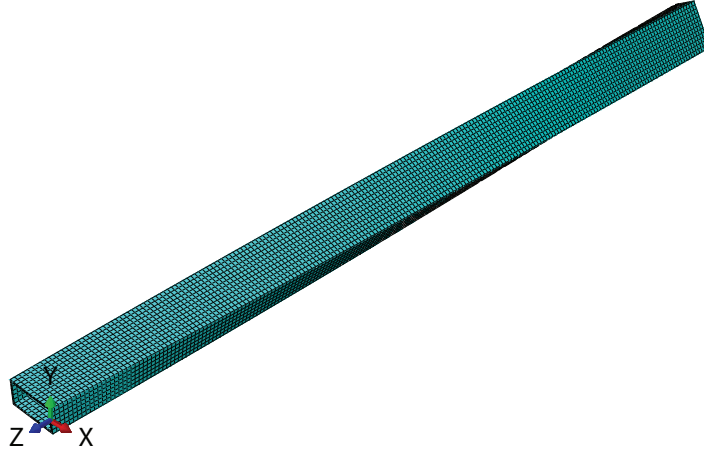
Figure 2.3 Isometric view of the hollow rectangular pre twisted beam.

their final values. Then, analyzing the same beam on a finite element analysis software, natural frequencies were found, and it is shown that the analytical model predicted the same frequencies with $< 1\%$ error, as given in Table 2.1.

		$n = 1$	$n = 2$	$n = 3$	$n = 4$	FEA
1st mode	downward	0.6157	0.6092	0.6069	0.6069	0.6046
	horizontal	0.6093	0.6027	0.6004	0.6004	0.5982
2nd mode	downward	0.9990	0.9868	0.9839	0.9837	0.9784
	horizontal	0.9951	0.9830	0.9799	0.9797	0.9744

Table 2.1 Natural frequencies (Hz) of the rectangular pre-twisted beam, $\Omega = 0$

To give an indication of the significance of the gravity's parametric effect, natural frequencies are found at different rotation angles. Since the gravity has stiffening and softening effects, the beam's natural frequencies change with the rotor angle. When the beam is upright, $\phi = \pi$, the gravitational force compresses it, and makes it less stiff in bending. When the rotor angle is $\phi = 0$, the gravitational force pulls the beam and makes it stiffer. These variations in stiffness can be estimated from the natural frequencies. For a blade with elastic stiffness k_0 and parametric stiffness k_1, the ratio of the frequencies of downward and horizontal orientations is

$$\frac{\omega_d}{\omega_h} = \sqrt{\frac{k_0 + k_1}{k_0}},$$

19

where ω_d and ω_h are downward and horizontal beam frequencies, respectively. Therefore the ratio of the parametric stiffness to elastic stiffness can be found as

$$\frac{k_1}{k_0} = \left(\frac{\omega_d}{\omega_h}\right)^2 - 1.$$

For the 50 m rectangular beam the stiffness contribution of the parametric effect is around 2.2%.

The first two mode shapes of the beam are plotted analytically for the downward position, as shown in Figure 2.4. There is no visible distinction between mode shapes calculated at different rotor angles. Both modes are coupled bending modes, and they do not have any contribution from torsional modes. The first mode is dominantly in the in-plane direction, whereas the second mode is in the out-of-plane direction. The mode shapes are also plotted through a finite element analysis, as shown in Figure 2.5, and they are consistent with the analytical ones.

In order to investigate the centrifugal effects, the beam is analyzed with different hub speeds. The first natural frequency increased by 4% for $\dot{\phi} = 1$ rad/s and 15% for $\dot{\phi} = 2$ rad/s, with the corresponding change in stiffness 8.2% and 32%, respectively. The centrifugal effect gets larger as the beam spins faster. Although in general horizontal-axis wind-turbines do not spin at high speeds, the centrifugal effects on the stiffness should be taken into account while designing turbine blades.

	$n = 3$	FEA
$\dot{\phi} = 1$	0.6243	0.6219
$\dot{\phi} = 2$	0.6904	0.6875

Table 2.2 Natural frequencies (Hz) of the rectangular pre-twisted horizontal beam.

The stiffness contributions of the gravity and the centrifugal force are carried through the inertial terms, as can be seen in equations of motion in Appendix A.3. In order to show the parametric effects on a less stiff beam, the same model is analyzed with half the Young's modulus, $E = 20$ GPa. The resulting frequencies are given in Table 2.3. The parametric
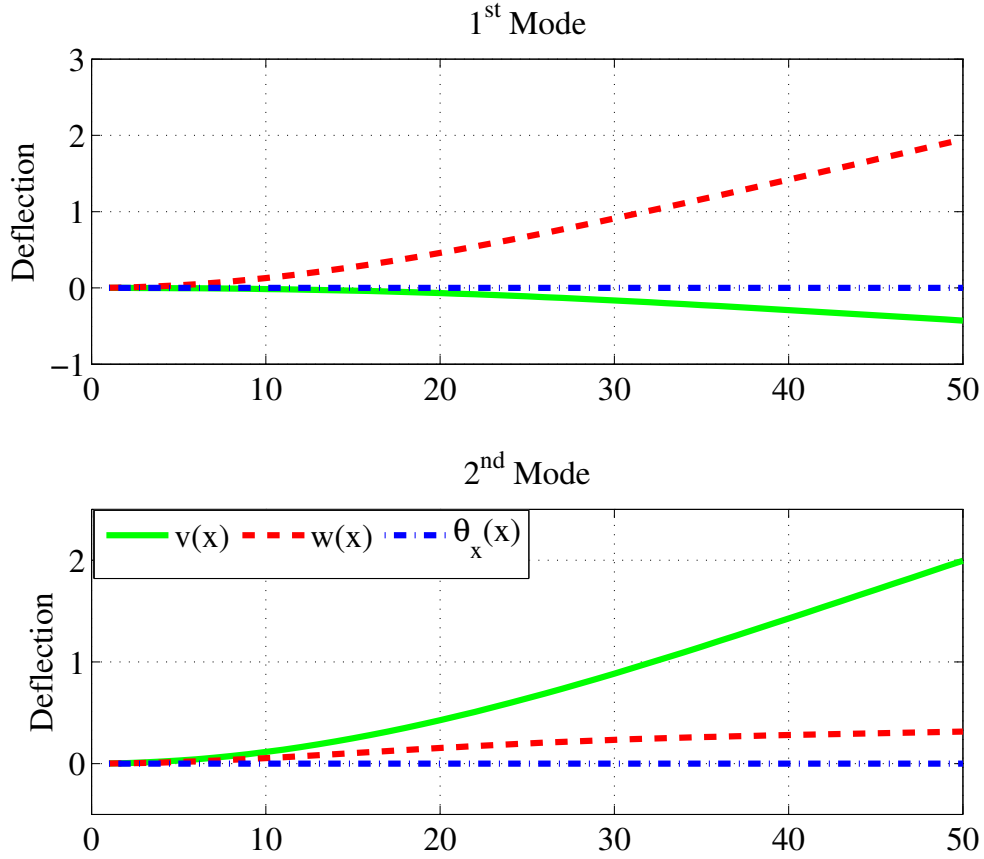
Figure 2.4 Analytical mode shapes for the stationary 50 m beam in downward position.

stiffness contribution to the modal stiffness of the lowest frequency mode is around 4.3%, which is twice as large as that of the beam with $E = 40$ GPa. Besides, for $\dot{\phi} = 1$ rad/s, the stiffness increased by 16.1%, which is almost twice that of the beam with $E = 40$ GPa. Therefore one can deduce that the parametric effects of the gravity and the centrifugal force are larger for less stiff blades.

	$n = 3$	FEA
$\dot{\phi} = 0$, downward	0.4337	0.4321
$\dot{\phi} = 0$, horizontal	0.4246	0.4229
$\dot{\phi} = 1$, horizontal	0.4576	0.4557

Table 2.3 The lowest natural frequency (Hz) of the rectangular pre-twisted beam with $E = 20$ GPa.
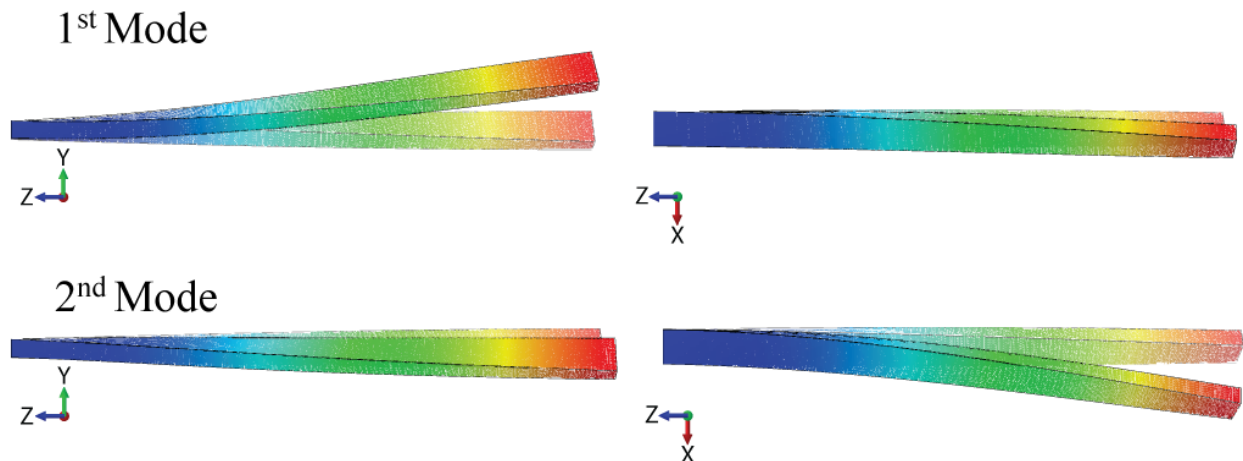
Figure 2.5 Side and top views of the FEA mode shapes for the stationary 50 m beam in downward position.

2.3.2 NREL's 23 m Blade

The National Renewable Energy Laboratory's (NREL's) 23 m blade is analyzed using $n = 4$ assumed modes. Distributed blade parameters and natural frequencies obtained from the experiments are tabulated in Bir and Oyague's study [72]. The frequencies calculated with our model and NREL's study are given in Table 2.4. In order to see the parametric effect of gravity, the blade is analyzed both in horizontal and downward positions, and to see the centrifugal effects we compared the stationary and spinning blade frequencies.

	1st mode	2nd mode
NREL's	1.72	2.41
$\dot{\phi} = 0$, downward	1.767	2.523
$\dot{\phi} = 0$, horizontal	1.760	2.519
$\dot{\phi} = 1$, horizontal	1.765	2.526

Table 2.4 Natural frequencies (Hz) for NREL's 23 m turbine blade.

For horizontal and downward blades, variation in the first natural frequency is about 0.4%, corresponding to a 0.8% change in modal stiffness. Furthermore, when the turbine is rotating with $\dot{\phi} = 1$ rad/s, the first natural frequency increases by 0.3%, corresponding to a 0.6% increase in modal stiffness. These variations are not significant since the centrifugal

and gravitational effects are smaller for shorter blades. Therefore it is acceptable to neglect these effects while designing short blades.

2.3.3 NREL's 5 MW Turbine Blade

NREL's 5 MW turbine blade is based on a model used in the Dutch Offshore Wind Energy Converter (DOWEC) project [7]. The blade is 61.5 m long, having a varying cross-section and a structural twist. In order to find the system natural frequencies, Jonkman *et al.* [8] conducted a linear eigen-analysis on ADAMS and also on FAST for the horizontal blade. These frequencies are given in Table 2.5 together with the frequencies calculated analytically by our method, both in downward and horizontal positions. For the horizontal blade, spinning blade frequencies are also provided to show the centrifugal effects.

	1st mode	2nd mode
NREL's	0.6664	1.0900
$\dot{\phi} = 0$, downward	0.6736	1.1088
$\dot{\phi} = 0$, horizontal	0.6668	1.1052
$\dot{\phi} = 1$, horizontal	0.6820	1.1211
[73], horizontal	0.698	0.975
[73], upright		0.951

Table 2.5 Natural frequencies (Hz) of NREL's 5 MW turbine blade.

The method used here predicted the first two frequencies of the stationary horizontal blade in $> 99\%$ agreement with [8]. The first natural frequency differs by 1% for downward and horizontal blades. This implies a 2% difference in modal stiffness of the first mode. This probably indicates a parametric effect that is too small to contribute significant parametric resonances. For a 61.5 m blade turbine, the rotor speed is expected to be around 1 rad/s. For this rotor speed, the first frequency increases by 2.3%, corresponding to a 4.6% increase in the modal stiffness. The effect of $\dot{\phi}$ on the second mode is less significant. Both the gravity's parametric effect and the centrifugal effect are larger compared to those we found for the 23 m blade, which supports the claim that these effects are more significant for

larger blades. Chauhan et al. also calculated the blade frequencies through simulating the stationary turbine [73]. They found the edgewise stiffness varies 4.9% which is higher than our prediction (which might be large enough to induce observable parametric resonances). This is probably because the tower dynamics are involved in the response of the upright bending mode in simulations.

The mode shapes for NREL's 61.5 m blade are given in Figure 2.6 for downward blade. The first two modes are coupled in bending directions. The first mode is dominantly in the flapwise direction, whereas the second mode is dominantly in the edgewise direction. This study shows that instead of studying the two bending directions separately, taking the coupling into account gives more accurate results. However, the mode shapes presented are dominated by an in-plane or an out-of-plane deflection, and so it is reasonable for engineers to speak of in-plane and out-of-plane modes, at least for low order models.

2.3.4 Sandia's 100 m Blade

Sandia National Laboratory (SNL) has a prototype blade design for a 100 m blade. SNL's 100 m baseline blade was developed by scaling up NREL's 61.5 m blade's dimensions. Scaling up all dimensions by a factor of α causes the horizontal natural frequencies to drop by a factor of α, although the scaling of the parametric effect is less clear. The blade's distributed parameters are tabulated in Griffith and Ashwill's study [9]. The frequencies for different blade orientations and different rotor speeds are tabulated in Table 2.6.

	1st mode	2nd mode
$\dot{\phi} = 0$, downward	0.4319	0.7450
$\dot{\phi} = 0$, horizontal	0.4255	0.7417
$\dot{\phi} = 1$, horizontal	0.4453	0.7646

Table 2.6 Natural frequencies (Hz) for SNL's 100 m turbine blade.

The first natural frequency varies 1.5%, between the horizontal and downward positions, and this corresponds to 3% change in modal stiffness. It is higher than that of the NREL's
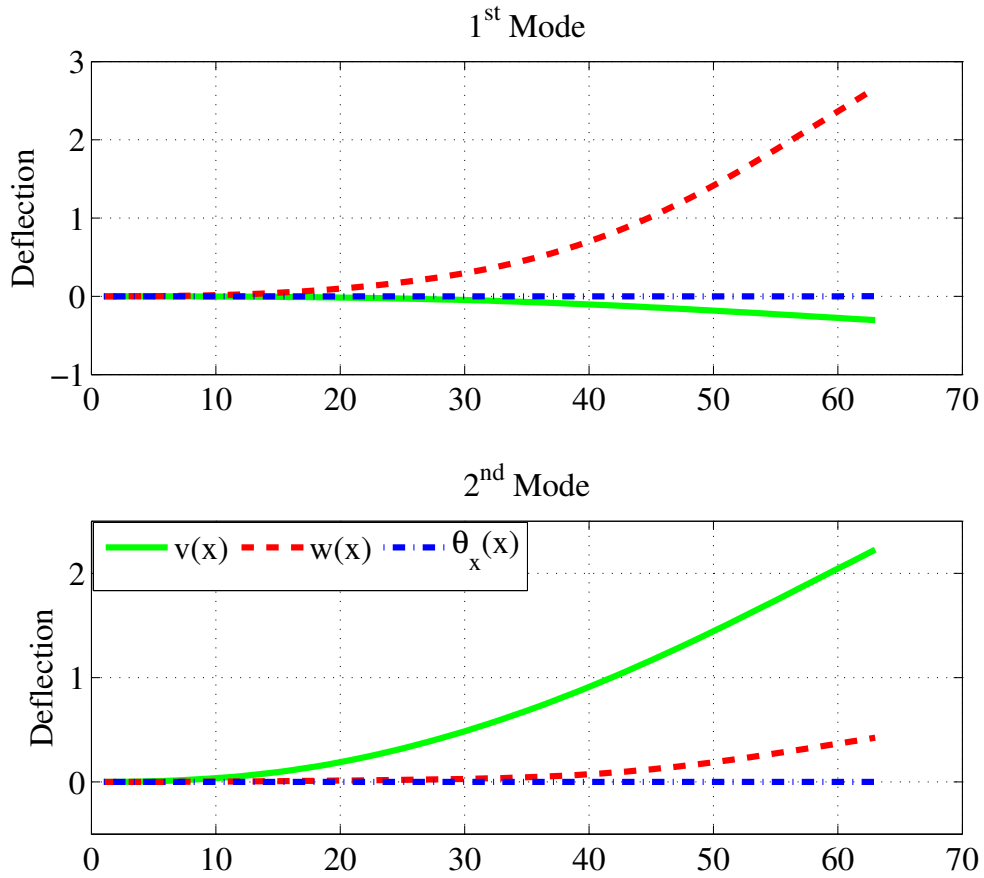
Figure 2.6 First two mode shapes for NREL's 61.5 m blade with $\dot{\phi} = 0$ and $\phi = \pi/2$.

61.5 m blade, because for longer blades the bending stiffness is lower while the gravitational load is higher. Therefore the relative effect of gravitational forces is higher. Also, for $\dot{\phi} = 1$ rad/s, the first frequency increases by 4.7%, which means a 9.5% change in the modal stiffness. While this difference is a lot larger than that of the 61.5 m blade, note that the 100 m blade will tend to operate at lower rotor speeds than the 61.5 m blade. This study shows that both the centrifugal and gravitational effects on stiffness must be taken into account while designing large blades.

2.3.5 The Relation Between the Blade Size and the Parametric Effects

As horizontal axis wind turbine blades get larger the parametric effects become more significant. In order to quantify the relation between the size of the blade and the parametric effects, the effect of the geometric parameters on the first natural frequency are investigated. To simplify the model for this study, we consider only in-plane bending. For a blade with modal mass m_b, elastic stiffness k_0 and parametric stiffness k_1, the first natural frequency in upright, horizontal and downward positions are

$$\omega_u = \sqrt{\frac{k_0 - k_1}{m_b}}, \quad \omega_h = \sqrt{\frac{k_0}{m_b}}, \quad \omega_d = \sqrt{\frac{k_0 + k_1}{m_b}},$$

where $m_b \propto AL$, $k_0 \propto \frac{EI_{\zeta\zeta}}{L^3}$ and $k_1 \propto \frac{AL}{L}$, as can be seen from the equations of motion in Appendix A.3.

2.3.5.1 A Scaling Study: Each Dimension Scaled Equally

For a scaled up model with each dimension increased by α while keeping the material properties fixed, the modal mass and stiffnesses are increased by the relations

$$m_b^{\alpha} = \alpha^3 m_b, \quad k_0^{\alpha} = \alpha k_0, \quad k_1^{\alpha} = \alpha^2 k_1.$$

For example, the rectangular hollow beam model in Section 2.3.1 is scaled up by doubling each dimension ($\alpha = 2$), and the natural frequencies are estimated by using the scaling relations. Also a finite element analysis is applied to find the corresponding frequencies, and results are compared as given in the first two columns of Table 2.7. The estimations are able to predict the modal frequencies with 99.6% accuracy. For the scaled up beam, the variation in the modal stiffness for the horizontal and the downward positions is 4.3% which is about twice of that for the original beam (2.2%). Therefore one can deduce that as the blades get bigger in size, the parametric effects become more significant.

Beam	$L^\alpha = 2L,\ A^\alpha = 4A$		$L^\alpha = 2L,\ A^\alpha = A$	
angle	est.	FEA	est.	FEA
downward	0.3055	0.3067	0.1625	0.1627
horizontal	0.2991	0.3002	0.1501	0.1502

Table 2.7 First modal frequencies (Hz) for the scaled up hollow rectangular beams: estimations from the scaling relations and FEA results, for $\alpha = 2$.

2.3.5.2 A Scaling Study: Only the Length Scaled

As horizontal axis wind turbine blades are designed longer, their thickness is not necessarily changed in the same proportion, and is more likely to change in a smaller proportion such that the blades become relatively more slender with increasing size. Consider another special case of a scaling pattern, where the length of the blade is scaled while the other dimensions are kept the same. This leads to

$$m_b^\alpha = \alpha m_b, \quad k_0^\alpha = k_0/\alpha^3, \quad k_1^\alpha = k_1.$$

As an example, the length of the beam in Section 2.3.1 is doubled ($\alpha = 2$), while the cross-sectional area is kept the same. The modal frequencies are estimated by using these scaling relations and are compared to the ones calculated via the finite element analysis, as shown in the two right-hand columns of Table 2.7. The variation in the modal stiffness for the horizontal and the downward positions is 17.2% whereas it is 2.2% for the original beam. Therefore, one can conclude that the parametric effects become a more serious issue if blade lengths increase proportionally more than cross-sectional dimensions.

2.3.5.3 A Scaling Study: NREL's 5 MW Turbine Blade

To show the relation between the blade size and the parametric effects, the ratio of the parametric and elastic modal stiffnesses $\left(k_1/k_0 = \omega_d^2/\omega_h^2 - 1\right)$ is estimated for scaled versions of the NREL's 61.5 m blade, as shown in Figure 2.7. There are two cases shown: 1) the whole volume is scaled, 2) only the blade length is scaled. We expect a realistic trend to be somewhere between the two. SNL's 100 m blade and NREL's 23 m blade are also shown in

this plot, and they lay on the scaled volume curve. This makes sense for the 100 m blade, since it is developed by scaling the whole volume of the 61.5 m blade.
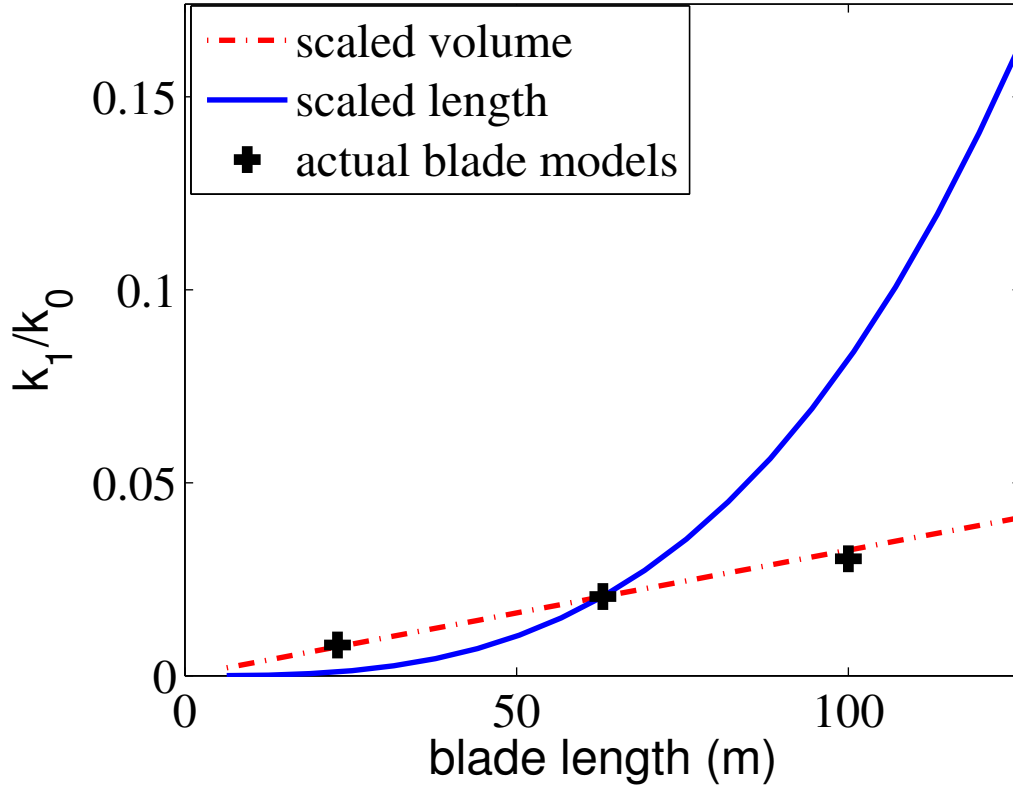
Figure 2.7 Parametric stiffness ratios for scaled blade models and actual blade models.

2.4 Conclusion

Bend-bend-twist blade vibration equations for a horizontal axis wind turbine were found by using Lagrange's equations and the assumed modes method. The kinetic and the potential energies of the blade as an inextensible nonuniform straight rotating slender beam in bend-bend-twist deformation were expressed in terms of familiar beam parameters. The coupled equations of motion were linearized, and a modal analysis was applied to the unexcited system to find the natural frequencies and mode shapes. Results suggest that while the bend-bend-twist coordinates are coupled, the lower flexural modes are dominated by either

in-plane or out-of-plane deflections. Thus, it is reasonable for engineers to speak of in-plane and out-of-plane models in approximation, although better accuracy is held in the coupled model.

The linearized equations have stiffness terms that vary with the angular speed, and have a dependence on the rotor angle. The analysis was applied to existing blade models, and the effects of rotor angle and rotation speed on natural frequencies were investigated. Results suggest that the rotor angle dependence on stiffness on existing blade models may not be strong enough to induce significant parametric effects. However, this result is for blades alone, and factoring in the tower may increase the parametric effect. The centrifugal stiffening and parametric effects become more significant as the blades get longer.

To show the effect of blade size on the parametric effects, a twisted beam model was scaled by changing only the length and also by changing the whole volume. Scaling only the length resulted in dramatic changes in the parametric effects, whereas scaling the whole blade resulted in a linear-like increase in the parametric effects with increasing length. Real blade designs are expected to scale somewhere between these two trends, suggesting that very long blades will have significant parametric stiffness effects.

CHAPTER 3

THREE-BLADE TURBINE EQUATIONS FOR IN-PLANE BENDING

3.1   Introduction

Dynamics of a three-blade horizontal-axis wind turbine is studied. The blade and the hub equations are found first. Then, applying a perturbation method, steady-state dynamics are investigated.

The energy expressions derived in Chapter 2 were approximated by assuming a single uniform cantilever beam mode for each blade. Tower motion is neglected, and the equations for blades and the hub were derived by using Lagrange's method. The tangential and normal components of the gravity force acting on a single blade change periodically with the blade angle. This causes a cyclic variation in the effective blade stiffness. As the rotor spins, centrifugal forces introduce a stiffening effect. Furthermore, wind speed usually varies with altitude, which causes the amount of wind force applied on a blade to change periodically as the blade rotates. These parametric stiffness and direct forcing effects were taken into account.

The independent variable is changed from time to rotor angle, for convenience. Then, a non-dimensionalization and a scaling procedure are applied to decouple the blade equations from the rotor equations.

A first-order method of multiple scales is applied to the coupled three-blade equations. The parametric and direct excitation of gravity introduces a superharmonic resonance, and the parametric excitation leads to a subharmonic resonance. The steady-state amplitude-frequency relations are found for each case, and the stabilities of the solutions are studied.

3.2   Three-Blade Turbine Equations

The total energy of the turbine is written by using the energy expressions for a single blade, as found in Chapter 2, and assuming a single cantilever beam mode for each blade. A simplified model is used where only in-plane vibrations are taken into account as shown in Figure 3.1, and tower motion is neglected. The hub is modeled as an unrestrained rigid body in a fixed axis rotation with damping that coarsely accomodates energy removal. The total kinetic and potential energies of the system can be written in the form

$$T_T = \frac{1}{2} J_{hub} \dot{\phi}^2 + \sum_{j=1}^{3} T(q_j, \dot{q}_j, \dot{\phi}), \tag{3.1}$$

$$U_T = \sum_{j=1}^{3} U(q_j), \tag{3.2}$$

$$V_{gT} = \sum_{j=1}^{3} V_g(q_j, \phi_j). \tag{3.3}$$

The four-degree-of-freedom system has the state variables q_1, q_2, q_3 and ϕ, where q_j are the assumed in-plane modal coordinates of each blade, and ϕ is the rotor angle. ϕ_j is the horizontal-axis rotation angle of the jth blade, which differs from ϕ by a constant (i.e. $\phi_j = \phi + \frac{2\pi}{3} j$). The energy expressions for a single blade are given in Appendix B.1. Applying Lagrange's equations, the blade and the rotor equations of motion are found. The blade equations are coupled through the rotor equation.

The linearized equations of motion for the jth blade and for the rotor are, (for $j = 1, 2, 3$)

$$m_b \ddot{q}_j + c_b \dot{q}_j + (k_0 + k_1 \dot{\phi}^2 + k_2 \cos \phi_j) q_j + d \sin \phi_j + e \ddot{\phi} = Q_j, \tag{3.4}$$

$$J_r \ddot{\phi} + c_r \dot{\phi} + \sum_{k=1}^{3} (d \cos \phi_k q_k + e \ddot{q}_k) = Q_\phi, \tag{3.5}$$

where m_b is the inertia of a single blade about the axis of its own undeflected shape, as shown with dashed lines in Figure 3.1, J_r is the total inertia of three blades plus the hub about the shaft axis, k_0 is the blades' elastic stiffness, and k_1 and k_2 are stiffness contributions of
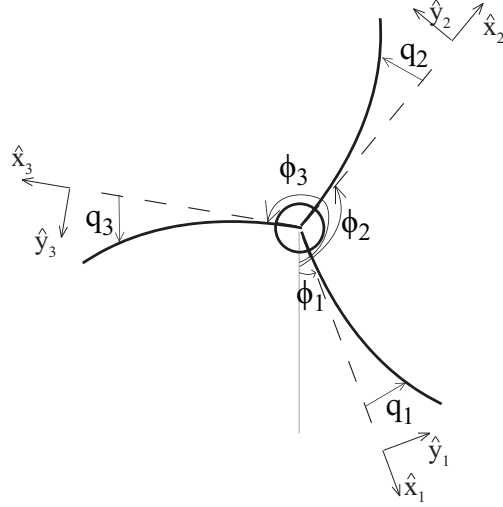
Figure 3.1 A three-blade turbine with blades under in-plane bending.

centrifugal and gravitational effects. The centrifugal stiffness term k_1 has a stiffening and a softening part [74], as shown in the Appendix B.2, but its stiffening part overcomes the softening part for the cantilever beam mode shape we used. Q_j and Q_ϕ are generalized forcing terms due to aeroelastic loading, and c_b and c_r are damping coefficients which are yet to be determined. These coefficients are modal parameters which depend on the assumed mode shapes, and are expressed in the Appendix B.2.

The zero-gravity system has modal frequencies $\omega_{n1} = 0$ with mode shape $v_1 = (0,\, 0,\, 0,\, 1)$ (rigid body rotation), $\omega_{n2,3} = \sqrt{\frac{k_0 + k_1 \Omega^2}{m_b}}$ (frequency of a single blade) with $v_2 = (1,\, -1,\, 0,\, 0)$ and $v_3 = (1,\, 0,\, -1,\, 0)$, $\omega_{n4} = \sqrt{\frac{k_0 + k_1 \Omega^2}{m_b - 3e^2/J_r}}$ (with coupling e) with $v_4 = (-\frac{J_r}{3e},\, -\frac{J_r}{3e},\, -\frac{J_r}{3e},\, 1)$. Blade-rotor mode shapes are shown in Figure 3.2.
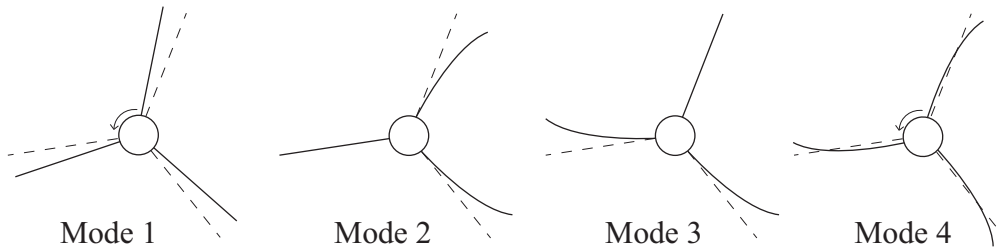
Figure 3.2 In-plane mode shapes of a three-blade turbine.

The rotor speed $\dot{\phi}$ is not constant, but assumed to vary a small amount around a mean

value. We introduce $\nu = \dot{\phi}/\Omega$, where Ω is the mean speed, and change the independent variable to ϕ, as done, for example, in the analysis of centrifugal pendulum vibration absorber systems [26, 29, 30]. This results in the derivative relations $\frac{d}{dt} = \frac{d\phi}{dt}\frac{d}{d\phi}$ and $\frac{d2}{dt^2} = \frac{d\nu}{d\phi}\nu\Omega^2\frac{d}{d\phi} + \nu^2\Omega^2\frac{d2}{d\phi^2}$. Re-writing Equations (3.4) and (3.5) with ϕ as the independent variable, one can obtain

$$\nu^2\frac{d^2 q_j}{d\phi^2} + \nu\frac{d\nu}{d\phi}\frac{dq_j}{d\phi} + \tilde{c}_b\nu\frac{dq_j}{d\phi} + (\tilde{k}_0 + \tilde{k}_1\nu^2 + \tilde{k}_2\cos\phi_j)q_j + \tilde{d}\sin\phi_j + \tilde{e}\nu\frac{d\nu}{d\phi} = \tilde{Q}_j, \quad (3.6)$$

$$\nu\frac{d\nu}{d\phi} + \tilde{c}_r\nu + \chi\sum_{k=1}^{3}\left[\tilde{d}\cos\phi_k q_k + \tilde{e}(\nu^2\frac{d^2 q_k}{d\phi^2} + \nu\frac{d\nu}{d\phi}\frac{dq_k}{d\phi})\right] = \tilde{Q}_\phi, \quad (3.7)$$

where

$$\tilde{c}_b = \frac{c_b}{m_b\Omega}, \quad \tilde{k}_0 = \frac{k_0}{m_b\Omega^2}, \quad \tilde{k}_1 = \frac{k_1}{m_b}, \quad \tilde{k}_2 = \frac{k_2}{m_b\Omega^2}, \quad \tilde{d} = \frac{d}{m_b\Omega^2},$$

$$\tilde{Q}_j = \frac{Q_j}{m_b\Omega^2}, \quad \tilde{e} = \frac{e}{m_b}, \quad \tilde{c}_r = \frac{c_r}{J_r\Omega}, \quad \chi = \frac{m_b}{J_r}, \quad \tilde{Q}_\phi = \frac{Q_\phi}{J_r\Omega^2}.$$

The quantity $\nu\frac{d\nu}{d\phi}$ accounts for the variations in the rotor speed, and it can be thought of as the dimensionless rotor acceleration ($\frac{d\nu}{dt} = \frac{d\nu}{d\phi}\frac{d\phi}{dt} = \frac{d\nu}{d\phi}(\Omega\nu)$). This can be seen by considering the summation in Equation (3.7), which stands for the loads applied by the blades on the rotor.

The rotor inertia J_r includes both the hub inertia and the inertia of the blades about the hub when undeformed, whereas m_b is the inertia of a single deflected blade about its own neutral axis. We define a small parameter as $\epsilon = m_b/J_r$. This is a legitimate assumption, since $\gamma_v(x)$ can be scaled such that $m_b << J_r$. In order to decouple the blade equation from the rotor equation, the following scaling relations are used:

$$\nu = 1 + \epsilon^2\nu_1, \quad \tilde{c}_b = \epsilon\hat{c}_b, \quad \tilde{k}_2 = \epsilon\hat{k}_2, \quad \tilde{d} = \epsilon\hat{d}, \quad \tilde{c}_r = \epsilon^2\hat{c}_r,$$

$$\chi = \epsilon, \quad q_j = \epsilon s_j, \quad \tilde{Q}_j = \epsilon\hat{Q}_j \quad \tilde{Q}_\phi = \epsilon^2\hat{Q}_\phi.$$

Parameters $\tilde{k}_1$ and $\tilde{k}_2$ are the stiffness terms contributed by centrifugal effects and gravity, and are small compared to the constant stiffness term, $\tilde{k}_0$. These physical parameters can be found in the Appendix B.2. An alternative scaling scheme is studied in Appendix B.3 where $\nu = 1 + \epsilon\nu_1$, and it is shown that the scaling used in this chapter ($\nu = 1 + \epsilon^2\nu_1$) is valid.

Equations (3.6) and (3.7) are rewritten in terms of the scaled blade coordinates, s_j, and the scaled hub coordinate, ν_1, as

$$\frac{d^2 s_j}{d\phi^2} + \epsilon\hat{c}_b\frac{ds_j}{d\phi} + (\tilde{k}_0 + \tilde{k}_1 + \epsilon\hat{k}_2\cos\phi_j)s_j + \hat{d}\sin\phi_j + \epsilon\tilde{e}\frac{d\nu_1}{d\phi} = \hat{Q}_j + H.O.T., \qquad (3.8)$$

$$\frac{d\nu_1}{d\phi} + \hat{c}_r + \sum_{k=1}^{3}(\epsilon\hat{d}\cos\phi_k s_k + \tilde{e}\frac{d^2 s_k}{d\phi^2}) = \hat{Q}_\phi + H.O.T. \qquad (3.9)$$

where $H.O.T.$ stands for higher-order terms. Obtained from Equation (3.9), $\frac{d\nu_1}{d\phi}$ is plugged into Equation (3.8) to obtain

$$\frac{d^2 s_j}{d\phi^2} + \epsilon\hat{c}_b\frac{ds_j}{d\phi} + (\tilde{k}_0 + \tilde{k}_1 + \epsilon\hat{k}_2\cos\phi_j)s_j + \hat{d}\sin\phi_j$$
$$+ \epsilon\tilde{e}\left[\hat{Q}_\phi - \hat{c}_r - \sum_{k=1}^{3}(\epsilon\hat{d}\cos\phi_k s_k + \tilde{e}\frac{d^2 s_k}{d\phi^2})\right] = \hat{Q}_j + H.O.T. \quad (3.10)$$

Forcing terms $\hat{Q}_j$ and $\hat{Q}_\phi$ accommodate aerodynamic loadings, and are assumed to have small variations, so that $\hat{Q}_j = Q_{j0} + \epsilon\hat{Q}_{j1}(\phi)$ and $\hat{Q}_\phi = Q_{\phi0} + \epsilon\hat{Q}_{\phi1}(\phi)$. For this analysis, we use a simplified model where the flow is assumed to be steady, and the wind speed is assumed to be slightly increasing linearly with height h (i.e. $u_{wind} = u_0 + \epsilon h u_1 = u_0 - \epsilon\cos\phi_j u_1$). The blade speed is governed by the rotor speed (i.e. $u_{blade} = \dot{\phi}x$). Therefore the relative flow velocity consists of ϕ and $\dot{\phi}$ terms. Assuming constant angle of attack (i.e. neglecting the contribution of state variations in the angle of attack), the lift force is proportional to

u_{rel}^2 (i.e. $\hat{Q}_j \propto u_{rel}^2$). Therefore, the assumed form of the aerodynamic force is

$$\hat{Q}_j = Q_{j0} + \epsilon Q_{j1} \cos \phi_j. \tag{3.11}$$

The details behind this assumed form in $\hat{Q}_j$ are given in the Appendix B.2. By neglecting the state-variable contributions to $\hat{Q}_j$, we are seeking to model the leading-order effects of resonance, and are not seeking to describe other aeroelastic instabilities or self-excitation effects.

Recall that the blade angles are such that $\phi_j = \phi + \frac{2\pi}{3}j$. Then plugging Equation (3.11) into Equation (3.10) and arranging terms, the blade equation is obtained as

$$\frac{d^2 s_j}{d\phi^2} + \hat{k}_0 s_j = Q_{j0} - \hat{d}\sin\left(\phi + \frac{2\pi}{3}j\right) + \epsilon \left[Q_{j1}\cos\left(\phi + \frac{2\pi}{3}j\right) \right.$$
$$\left. - \tilde{e}Q_{\phi 0} + \tilde{e}\hat{c}_r - \hat{c}_b\frac{ds_j}{d\phi} - \hat{k}_2\cos\left(\phi + \frac{2\pi}{3}j\right)s_j + \tilde{e}^2\sum_{k=1}^{3}\frac{d^2 s_k}{d\phi^2} \right], \tag{3.12}$$

where $\hat{k}_0 = \tilde{k}_0 + \tilde{k}_1$, and the term with $\hat{k}_2$ is the parametric excitation associated with gravity. The modal orders of the unexcited angle-based system equations are $p_{1,2} = \sqrt{\frac{k_0/\Omega^2 + k_1}{m_b}}$, $p_3 = \sqrt{\frac{k_0/\Omega^2 + k_1}{m_b - 3e^2/J_r}}$. These are scaled versions of the time-based system frequencies, such as $p_{1,2} = \omega_{n2,3}/\Omega$ and $p_3 = \omega_{n4}/\Omega$.

Notice that the coupling between the blades is through the inertial terms. One way to handle this is to use a coordinate transformation to make the equations coupled through stiffness terms, and then apply averaging. This can be done by making use of Fourier matrix, as explained in [28]. Or one can use the method of multiple scales to find the slow flow relations. The latter is used in this study to investigate the internal resonances one by one.

3.3   Application of Method of Multiple Scales

We rescale the independent variable from ϕ to $\psi = p_1\phi$, where $p_1 = \sqrt{\hat{k_0}} = \sqrt{\frac{k_0/\Omega^2 + k_1}{m_b}}$.
The equations of motion in ψ are

$$s_j'' + s_j = F_{j0} - \delta \sin\left(r_1\psi + \frac{2\pi}{3}j\right) + \epsilon\left[F_{j1}\cos\left(r_1\psi + \frac{2\pi}{3}j\right)\right.$$

$$\left. + f - \zeta s_j' - \kappa \cos\left(r_1\psi + \frac{2\pi}{3}j\right)s_j + \tilde{e}^2 \sum_{k=1}^{3} s_k''\right], \quad (3.13)$$

where $(\;)'$ stands for $d/d\psi$ and

$$F_{j0} = Q_{j0}/\hat{k_0}, \quad \delta = \hat{d}/\hat{k_0}, \quad r_1 = 1/p_1, \quad F_{j1} = Q_{j1}/\hat{k_0},$$

$$f = \tilde{e}(\hat{c}_r - Q_{\phi0})/\hat{k_0}, \quad \zeta = \hat{c}_b/p_1, \quad \kappa = \hat{k}_2/\hat{k_0}.$$

Equation (3.13) is both directly excited with constant load F_{j0} and cyclic load strengths δ and F_{j1}, and parametrically excited with strength κ. The quantity r_1 is a scaled "excitation order", and is given by

$$r_1 = \frac{\Omega}{\omega_{n2}},$$

where $\omega_{n2} = \sqrt{\frac{k0 + k_1\Omega^2}{m_b}}$ is a modal frequency of the turbine. Therefore variations in mean rotor speed, Ω, will result in variations in the excitation order r_1.

To investigate the steady state dynamics of interdependent blade equations, a first order method of multiple scales is applied [38]. s_j is divided into a dominant part and a correction, with each part dependent on a "slow scale" and a "fast scale", as $s_j = s_{j0}(\psi_0, \psi_1) + \epsilon s_{j1}(\psi_0, \psi_1)$, where $\psi_1 = \epsilon\psi_0$. Derivative relations are $d/d\psi = D_0 + \epsilon D_1$ where $D_0 = \partial/\partial\psi_0$ and $D_1 = \partial/\partial\psi_1$. This form of s_j is applied to Equation (3.13), and coefficients of like powers of ϵ are collected below.

ϵ^0 equation:

$$D_0^2 s_{j0} + s_{j0} = F_{j0} - \delta \sin\left(r_1 \psi_0 + \frac{2\pi}{3} j\right) \qquad (3.14)$$

ϵ^1 equation:

$$2D_0 D_1 s_{j0} + D_0^2 s_{j1} + s_{j1} = F_{j1} \cos\left(r_1 \psi_0 + \frac{2\pi}{3} j\right) + f$$

$$- \zeta D_0 s_{j0} - \kappa \cos\left(r_1 \psi_0 + \frac{2\pi}{3} j\right) s_{j0} + \tilde{e}^2 \sum_{k=1}^{3} D_0^2 s_{k0} \quad (3.15)$$

Solving Equation (3.14), s_{j0} is found as

$$s_{j0} = \frac{F_{j0}}{2} + A_j e^{i\psi_0} + iB e^{i(r_1 \psi_0 + \frac{2\pi}{3} j)} + \text{c.c.} \qquad (3.16)$$

where $A_j = \frac{1}{2} a_j e^{i\beta_j}$ is complex (such that $A_j e^{i\psi_0} + \text{c.c.} = a_j \cos(\psi_0 + \beta_j)$) and $B = \frac{\delta}{2(1-r_1^2)}$.

Plugging Equation (3.16) and the relations, $D_0 s_{j0} = iA_j e^{i\psi_0} - Br_1 e^{i(r_1 \psi_0 + \frac{2\pi}{3} j)} +$ c.c., and $D_0 D_1 s_{j0} = iA_j' e^{i\psi_0} +$ c.c., into Equation (3.15), we obtain the governing equation for s_{j1}:

$$D_0^2 s_{j1} + s_{j1} = \frac{F_{j1}}{2} e^{i(r_1 \psi_0 + \frac{2\pi}{3} j)} + \frac{f}{2} - 2iA_j' e^{i\psi_0} - \frac{F_{j0}}{2} \kappa e^{i(r_1 \psi_0 + \frac{2\pi}{3} j)} - \kappa i \frac{B}{2} e^{2i(r_1 \psi_0 + \frac{2\pi}{3} j)}$$

$$- \zeta \left(A_j i e^{i\psi_0} - r_1 B e^{i(r_1 \psi_0 + \frac{2\pi}{3} j)}\right) - \frac{\kappa}{2}\left(A_j e^{i(r_1+1)\psi_0 + i\frac{2\pi}{3} j} + \bar{A}_j e^{i(r_1-1)\psi_0 + i\frac{2\pi}{3} j}\right)$$

$$+ \tilde{e}^2 \sum_{k=1}^{3}\left(-A_k e^{i\psi_0} - ir_1^2 B e^{i(r_1 \psi_0 + \frac{2\pi}{3} k)}\right) + \text{c.c.} \quad (3.17)$$

37

3.3.1 Nonresonant Case

Equating the terms that are leading to an unbounded solution (i.e. secular terms) to zero, the solvability condition can be found. For an arbitrary r_1,

$$-2iA'_j - i\zeta A_j - \tilde{e}^2 \sum_{k=1}^{3} A_k = 0.$$

In Cartesian form, $A_j = X_j + iY_j$ is inserted, and real and imaginary parts are separated as

Re part:

$$Y'_j = -\frac{\zeta}{2}Y_j + \frac{\tilde{e}^2}{2} \sum_{k=1}^{3} X_k, \tag{3.18}$$

Im part:

$$X'_j = -\frac{\zeta}{2}X_j - \frac{\tilde{e}^2}{2} \sum_{k=1}^{3} Y_k. \tag{3.19}$$

In matrix form

$$
\begin{pmatrix} X'_1 \\ X'_2 \\ X'_3 \\ Y'_1 \\ Y'_2 \\ Y'_3 \end{pmatrix} = \frac{1}{2}
\begin{bmatrix}
-\zeta & 0 & 0 & -\tilde{e}^2 & -\tilde{e}^2 & -\tilde{e}^2 \\
0 & -\zeta & 0 & -\tilde{e}^2 & -\tilde{e}^2 & -\tilde{e}^2 \\
0 & 0 & -\zeta & -\tilde{e}^2 & -\tilde{e}^2 & -\tilde{e}^2 \\
\tilde{e}^2 & \tilde{e}^2 & \tilde{e}^2 & -\zeta & 0 & 0 \\
\tilde{e}^2 & \tilde{e}^2 & \tilde{e}^2 & 0 & -\zeta & 0 \\
\tilde{e}^2 & \tilde{e}^2 & \tilde{e}^2 & 0 & 0 & -\zeta
\end{bmatrix}
\begin{pmatrix} X_1 \\ X_2 \\ X_3 \\ Y_1 \\ Y_2 \\ Y_3 \end{pmatrix}. \tag{3.20}
$$

At steady state, the solution is $X_j = 0$ and $Y_j = 0$. Eigenvalues of the coefficient matrix are $\lambda_{1,2,3,4} = -\zeta$, $\lambda_{5,6} = -\zeta \pm i3\tilde{e}^2$. For all λ, $\text{Re}(\lambda) \leq 0$. Therefore the nonresonant solution is stable.

3.3.2 Superharmonic Resonance ($2r_1 \approx 1$ or $2\Omega \approx \omega_{n2}$)

$2r_1 = 1 + \epsilon\sigma$

Superharmonic resonances may be of significance to wind turbine blades, as the turbines are designed to operate well below the blades fundamental modal frequencies. A super-harmonic of order $1/2$ may still be outside of typical design ranges, but it is possible that these trends are pushed as the turbine sizes continue to increase or if operating regimes are pushed. Furthermore, studies have shown that superharmonics of order $1/3$ can be revealed in single-mode blade dynamics by second-order perturbation analyses [71]. In any case, it is important for designers to be aware of superharmonic behavior. Furthermore, they may also be excited by higher harmonics of cyclic excitations.

Equating the terms that are leading to an unbounded solution (i.e. secular terms) to zero, the solvability condition can be found for $2r_1 \approx 1$ as

$$-2\mathrm{i}A_j' - \mathrm{i}\zeta A_j - \mathrm{i}\frac{B\kappa}{2}\mathrm{e}^{\mathrm{i}(\sigma\psi_1 + \frac{4\pi}{3}j)} - \tilde{e}^2\sum_{k=1}^{3} A_k = 0.$$

Putting $A_j = \Lambda_j \mathrm{e}^{\mathrm{i}(\sigma\psi_1 + \frac{4\pi}{3}j)}$ with $\Lambda_j = X_j + \mathrm{i}Y_j$, we can separate the real and imaginary parts as below.

Re part:

$$Y_j' = -\sigma X_j - \frac{\zeta}{2}Y_j + \frac{\tilde{e}^2}{2}\sum_{k=1}^{3}\left[X_k \cos\left(\frac{4\pi}{3}(k-j)\right) - Y_k \sin\left(\frac{4\pi}{3}(k-j)\right)\right], \qquad (3.21)$$

Im part:

$$X_j' = \sigma Y_j - \frac{\zeta}{2}X_j - \frac{B\kappa}{4} - \frac{\tilde{e}^2}{2}\sum_{k=1}^{3}\left[X_k \sin\left(\frac{4\pi}{3}(k-j)\right) + Y_k \cos\left(\frac{4\pi}{3}(k-j)\right)\right]. \quad (3.22)$$

At steady state the solution is $X_j = -\dfrac{B\zeta\kappa}{2\left(\zeta^2 + 4\sigma^2\right)}$, $Y_j = \dfrac{B\kappa\sigma}{\zeta^2 + 4\sigma^2}$, which means $A_j = \dfrac{-\zeta + \mathrm{i}2\sigma}{2\left(\zeta^2 + 4\sigma^2\right)}B\kappa\mathrm{e}^{\mathrm{i}(\sigma\psi_1 + \frac{4\pi}{3}j)}$. Eigenvalues of the coefficient matrix are $\lambda_{1,2} = -\frac{\zeta}{2} - \mathrm{i}\sigma$, $\lambda_{3,4} = -\frac{\zeta}{2} + \mathrm{i}\sigma$ and $\lambda_{5,6} = -\frac{\zeta}{2} \pm \mathrm{i}\frac{(2\sigma - 3\tilde{e}^2)}{2}$. For all λ, $\mathrm{Re}(\lambda) \leq 0$. Therefore the solution is stable.

The amplitude and the phase of A_j are

$$|A_j| = \frac{|B\kappa|}{2\sqrt{(\zeta^2 + 4\sigma^2)}}, \tag{3.23}$$

$$\angle A_j = -\arctan\left(\frac{2\sigma}{\zeta}\right) + \sigma\psi_1 + \frac{4\pi}{3}j, \tag{3.24}$$

and the homogeneous solution for the jth blade is

$$s_{jh} = a\cos\left(\psi_0 + \sigma\psi_1 + \beta + \frac{4\pi}{3}j\right), \tag{3.25}$$

where $a = 2|A_j| = \frac{|B\kappa|}{\sqrt{(\zeta^2 + 4\sigma^2)}}$, and $\beta = -\arctan\left(\frac{2\sigma}{\zeta}\right)$. Since $1 + \epsilon\sigma = 2r_1$, for the specific superharmonic case the homogeneous solution can also be written as

$$s_{jh} = a\cos\left(2r_1\psi_0 + \beta + \frac{4\pi}{3}j\right), \tag{3.26}$$

and in ϕ domain

$$s_{jh} = a\cos\left(2\phi + \beta + \frac{4\pi}{3}j\right). \tag{3.27}$$

The system has a unison amplitude response. The amplitude does not depend on the coupling term, $\tilde{e}$, and it is directly affected by the direct and the parametric excitation terms, B and κ. The peak amplitude is $A_p = |\delta\kappa|/3\zeta$. Amplitude-frequency plots are given in Figure 3.3 and Figure 3.4. Decreasing ζ sharpens the resonance, while increasing $|\delta\kappa|$ raises the whole curve.

Since variations in ν_1 are order of ϵ and $\dot{\phi} = \Omega(1 + \epsilon^2\nu_1)$, these variations will appear in $\dot{\phi}$ with order of ϵ^3. Therefore the rotor angle can be approximated as $\phi = \Omega t + \epsilon^3\nu_{11}\cos((p_1 + 1)\Omega t)$. In time domain, the blade response can be approximated by

$$q_j = \epsilon\left(F_{j0} - 2B\sin\left(\Omega t + \frac{2\pi}{3}j\right) + a\cos\left(2\Omega t + \beta + \frac{4\pi}{3}j\right)\right) + O(\epsilon^4). \tag{3.28}$$

In order to investigate the response of the rotor, the solution is written in ϕ domain as $s_j = F_{j0} - 2B\sin\left(\phi + \frac{2\pi}{3}j\right) + a\cos\left(2\phi + \beta + \frac{4\pi}{3}j\right)$, and inserted into Equation (3.9). This
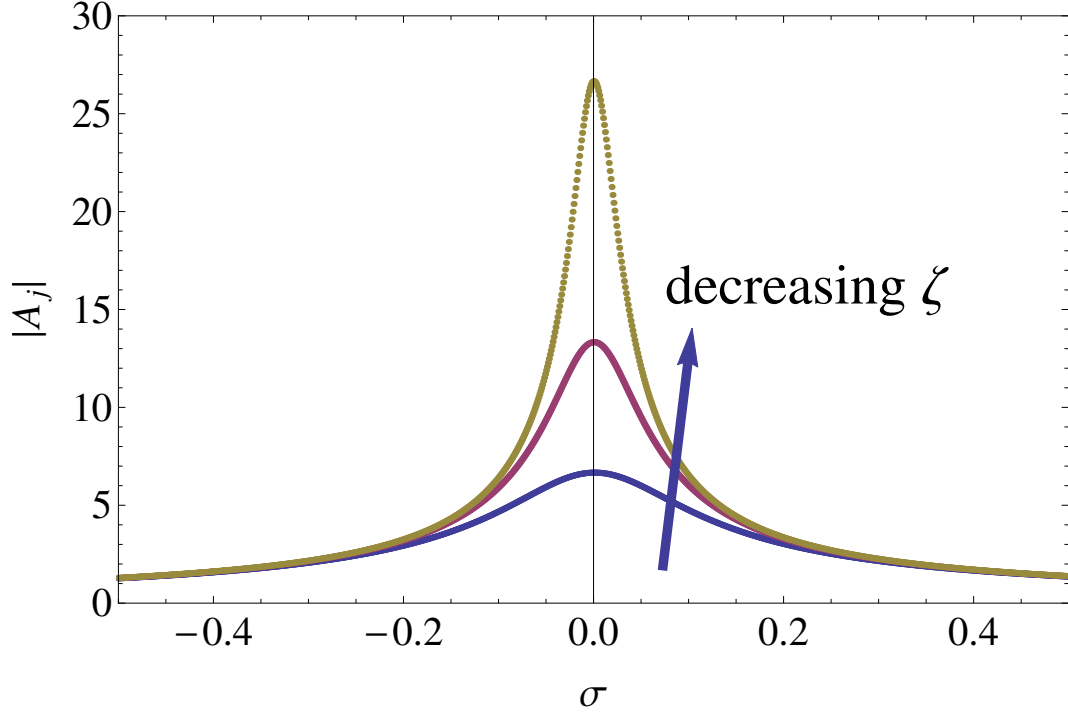
Figure 3.3 Steady state superharmonic resonance response amplitude, frequency plots for $\kappa = 1$, $\delta = 4$, $\zeta = 0.05, 0.1, 0.2$.

leads to

$$\frac{d\nu_1}{d\phi} = \hat{Q}_\phi - \hat{c}_r + \epsilon\hat{d}\left(\sin{(\phi)}\sum_{k=1}^{3}F_{k0}\sin{(\frac{2\pi}{3}k)}\right.$$
$$\left. - \cos{(\phi)}\sum_{k=1}^{3}F_{k0}\cos{(\frac{2\pi}{3}k)} - \frac{3}{2}a\cos{(3\phi + \beta)}\right). \quad (3.29)$$

The leading order component of the nondimensionalized aerodynamic force $F_{k0} = Q_{k0}/\hat{k}_0$ is the same for all k, as can be seen in the Appendix B.2. Plugging $F_{k0} = F_0$ into the above equation, we obtain

$$\frac{d\nu_1}{d\phi} = \hat{Q}_\phi - \hat{c}_r - \frac{3}{2}\epsilon\hat{d}a\cos{(3\phi + \beta)}. \quad (3.30)$$

41
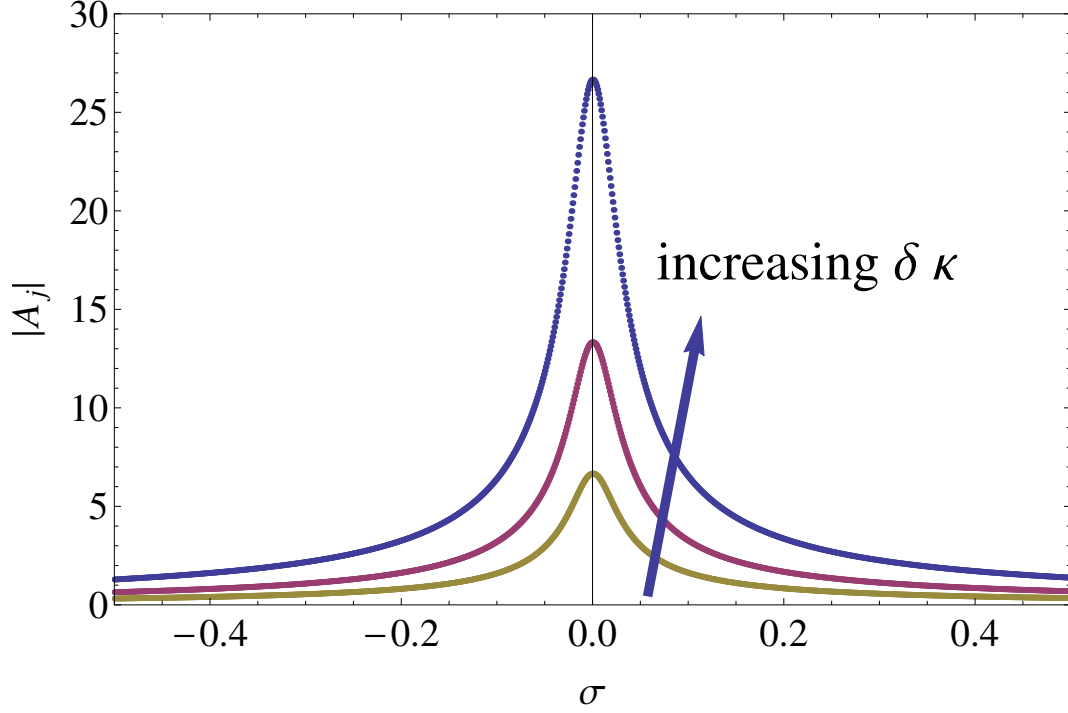
Figure 3.4 Steady state superharmonic resonance response amplitude, frequency plots for $\zeta = 0.05$, $\kappa = 1$, $\delta = 1, 2, 4$.

3.3.3 Primary Resonance ($r_1 \approx 1$ or $\Omega \approx \omega_{n2}$)

$r_1 = 1 + \epsilon\sigma$

By design, turbines are unlikely to operate near primary resonance except in rare situations such as runaway rotor speeds. In order to investigate the primary resonance response, the harmonic forcing is modeled as "weak forcing" (i.e. $\delta = \epsilon\hat{\delta}$). This changes the forms of Equations (3.13) and (3.14), and leads to a solution in the form

$$s_{j0} = \frac{F_{j0}}{2} + A_j e^{i\psi_0} \tag{3.31}$$

and an ϵ^1 equation of the form

$$2D_0 D_1 s_{j0} + D_0^2 s_{j1} + s_{j1} = F_{j1} \cos\left(r_1\psi_0 + \frac{2\pi}{3}j\right) - \hat{\delta}\sin\left(r_1\psi_0 + \frac{2\pi}{3}j\right)$$

$$+ f - \zeta D_0 s_{j0} - \kappa\cos\left(r_1\psi_0 + \frac{2\pi}{3}j\right)s_{j0} + \tilde{e}^2\sum_{k=1}^{3} D_0^2 s_{k0}. \tag{3.32}$$

Equating the terms that are leading to an unbounded solution (i.e. secular terms) to zero, the solvability condition can be found for $r_1 \approx 1$ as

$$- 2\mathrm{i}A'_j - \mathrm{i}\zeta A_j + \left(\frac{F_{j1}}{2} - \frac{F_{j0}}{2}\kappa + \mathrm{i}\frac{\hat{\delta}}{2} \right) e^{\mathrm{i}(\sigma\psi_1 + \frac{2\pi}{3}j)} - \tilde{e}^2 \sum_{k=1}^{3} A_k = 0.$$

Putting $A_j = \Lambda_j e^{\mathrm{i}(\sigma\psi_1 + \frac{2\pi}{3}j)}$ with $\Lambda_j = X_j + \mathrm{i}Y_j$, we can separate the real and imaginary parts as below.

Re part:

$$Y'_j = -\sigma X_j - \frac{\zeta}{2}Y_j - c_1 + \frac{\tilde{e}^2}{2}\sum_{k=1}^{3}\left[X_k \cos\left(\frac{2\pi}{3}(k-j) \right) - Y_k \sin\left(\frac{2\pi}{3}(k-j) \right) \right], \quad (3.33)$$

Im part:

$$X'_j = \sigma Y_j - \frac{\zeta}{2}X_j - \frac{\hat{\delta}}{2} - \frac{\tilde{e}^2}{2}\sum_{k=1}^{3}\left[X_k \sin\left(\frac{2\pi}{3}(k-j) \right) + Y_k \cos\left(\frac{2\pi}{3}(k-j) \right) \right], \quad (3.34)$$

where $c_1 = \frac{F_{j1}}{4} - \frac{F_{j0}}{4}\kappa$. At steady state the solution is $X_j = -\frac{\hat{\delta}\zeta + 4\sigma c_1}{\zeta^2 + 4\sigma^2}$, $Y_j = \frac{2\hat{\delta}\sigma - 2\zeta c_1}{\zeta^2 + 4\sigma^2}$, which means $A_j = \sqrt{\frac{\hat{\delta}^2 + 4c_1^2}{\zeta^2 + 4\sigma^2}}e^{\mathrm{i}(\sigma\psi_1 + \frac{2\pi}{3}j + \beta)}$, where $\beta = \tan^{-1}\left(\frac{2\zeta c_1 - 2\hat{\delta}\sigma}{\hat{\delta}\zeta + 4\sigma c_1} \right)$. The equations have the same eigenvalues as those in the superharmonic case. Therefore to a first-order approximation the solution is stable.

Single-degree-of-freedom parametrically excited systems can have slender instability wedges near primary resonance, but a second-order MMS would be needed to uncover it [38, 71]. Thus we have not ruled out that such a phenomenon exists in this system as well.

In order to investigate the response of the rotor, the solution $s_j = F_{j0} + a\cos\left(\phi + \beta + \frac{2\pi}{3}j \right)$ is inserted into Equation (3.9), where $a = 2\sqrt{X^2 + Y^2}$ and $\beta = \tan^{-1}(\frac{Y}{X})$. This results in

$$\frac{d\nu_1}{d\phi} = \hat{Q}_\phi - \hat{c}_r - \frac{3}{2}\epsilon\hat{d}a\cos\beta. \quad (3.35)$$

Note that ν_1 stands for the small oscillations from the mean speed. Therefore speed variations introduced by the constant terms (direct forcing) can be considered as a variation in the mean speed. So, one can conclude that the blade responses do not have any effect on ν dynamics.

3.3.4 Subharmonic Resonance ($r_1 \approx 2$ or $\Omega \approx 2\omega_{n2}$)

$r_1 = 2 + \epsilon\sigma$

Subharmonic resonances are well out of the range of turbine designs. However, the phenomena are of general dynamical interest, and are therefore included here. Equating the terms that are leading to an unbounded solution (i.e. secular terms) to zero, the solvability condition can be found for $r_1 \approx 2$ as

$$-2A'_j i - i\zeta A_j - \kappa\frac{\bar{A}_j}{2}e^{i(\sigma\psi_1 + \frac{2\pi}{3}j)} - \tilde{e}^2\sum_{k=1}^{3}A_k = 0$$

Putting $A_j = \Lambda_j e^{i(\frac{\sigma\psi_1}{2} + \frac{\pi}{3}j)}$ with $\Lambda_j = X_j + iY_j$, we can separate the real and imaginary parts as below.

Re part:

$$Y'_j = -\frac{\sigma}{2}X_j - \frac{\zeta}{2}Y_j + \frac{\kappa}{4}X_j + \frac{\tilde{e}^2}{2}\sum_{k=1}^{3}\left[X_k\cos\left(\frac{\pi}{3}(k-j)\right) - Y_k\sin\left(\frac{\pi}{3}(k-j)\right)\right], \quad (3.36)$$

Im part:

$$X'_j = \frac{\sigma}{2}Y_j - \frac{\zeta}{2}X_j + \frac{\kappa}{4}Y_j - \frac{\tilde{e}^2}{2}\sum_{k=1}^{3}\left[X_k\sin\left(\frac{\pi}{3}(k-j)\right) + Y_k\cos\left(\frac{\pi}{3}(k-j)\right)\right]. \quad (3.37)$$

Equations (3.36) and (3.37) are autonomous. At steady state, the solution is $X_j = 0$, $Y_j = 0$. Eigenvalues of this system are $\lambda_{1,2} = -\frac{\zeta}{2} \pm \frac{\sqrt{\kappa^2 - 4\sigma^2}}{4}$, $\lambda_{3,4,5,6} = -\frac{\zeta}{2} \pm \sqrt{\frac{\kappa^2 - 9\tilde{e}^4 - (2\sigma - 3\tilde{e}^2)^2 \pm 6\tilde{e}^2\sqrt{(2\sigma - 3\tilde{e}^2)^2 - \kappa^2}}{4}}$. The solution is stable if $\text{Re}(\lambda) \leq 0$ for all λ, and unstable if $\text{Re}(\lambda) > 0$ for at least one λ. Stability curves of this system are given in Figure 3.5 and Figure 3.6.

When there is no coupling between blades (i.e. $\tilde{e} = 0$), the system effectively is of a single degree of freedom, and there is only one instability wedge starting at $\sigma = 0$, bounded by the $\sigma = \pm\frac{\kappa}{2}$ lines (Figure 3.5). This corresponds to the well known subharmonic instability wedge as seen in the Mathieu equation [75].

However when there is coupling (Figure 3.6), a second instability region emerges from the $\sigma = \frac{3}{2}\tilde{e}^2$ point, bounded by lines defined according to

$$\sigma = \frac{3}{2}\tilde{e}^2 \pm \frac{\kappa}{2}. \tag{3.38}$$

Therefore coupling between the blades introduces a new instability. For multi-degree-of-freedom systems, the observed instability wedges have been generally identified with $(\omega_{nj} + \omega_{nk})/N$, where ω_{nj} and ω_{nk} are modal frequencies and N is a positive integer [76] (See also Chapter 5). The system given in Equation (3.13) has the modal orders $r_{n1,2} = 1$ and $r_{n3} = 1 + \frac{3}{2}\epsilon\tilde{e}^2 + O(\epsilon^2)$. The second instability wedge in Figure 3.6 is based at $\sigma = \frac{3}{2}\tilde{e}^2$. For the subharmonic resonance at $r_1 = 2 + \epsilon\sigma$, this corresponds to $r_1 = 2 + \frac{3}{2}\epsilon\tilde{e}^2 = r_{n1} + r_{n3}$.

In order to verify the analytical results, Equation (3.13) was simulated near $r_1 = 2$, and stability of the solution was studied. The system was simulated from $\psi = 0$ to 500, over a grid on the $\kappa - \omega$ plane. As a stability criterion, we checked if the norm of the s_j at $\psi = 500$ was smaller or larger than that of the initial conditions (i.e. stable if $s_j(500) < s_j(0)$, unstable otherwise). Simulation results are shown in Figures 3.5 and 3.6, and it can be seen that the analytical results from perturbation analysis with a small parameter are consistent with the simulations.

3.3.5 Existence of Resonance Conditions

The resonance conditions found from Equation (3.17) are $\omega_{n2} \approx \Omega/2$, Ω, 2Ω, where $\omega_{n2} = \sqrt{\frac{k_0 + k_1\Omega^2}{m_b}}$. Existence of the resonance conditions depends on the parameters involved in the modal frequency. For $\omega_{n2} = \alpha\Omega$ (where $\alpha = 1/2$ for superharmonic, 1 for primary, and 2 for superharmonic resonances), we have

$$\frac{k_0 + k_1\Omega^2}{m_b} = \alpha^2\Omega^2, \tag{3.39}$$

which leads to the excitation frequency condition

$$\Omega = \sqrt{\frac{k_0}{m_b\alpha^2 - k_1}}. \tag{3.40}$$

45
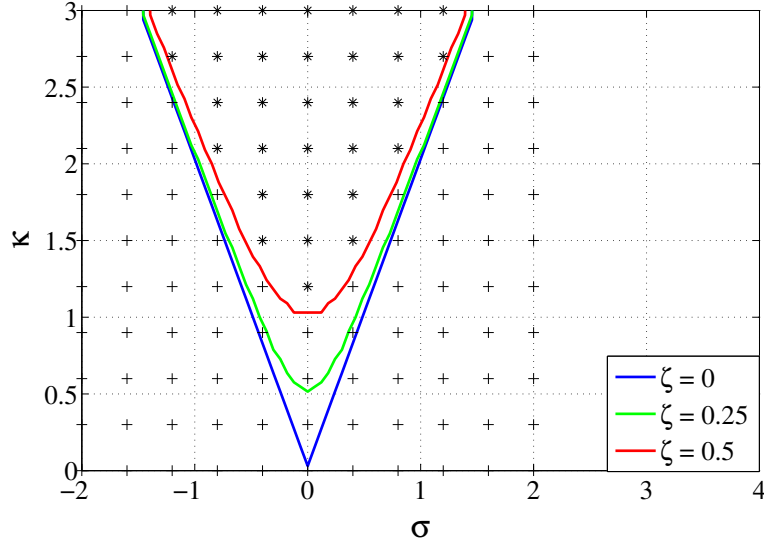
Figure 3.5 Stability plots for the subharmonic response for $\tilde{e} = 0$, $\zeta = 0, 0.25, 0.5$. Simulations are done for $\zeta = 0.5$, $\epsilon = 0.1$, $F_{j0} = 0.1$, $F_{j1} = 0.1$, $\delta = 1.5$, $f = 0.1$, (+): stable, (∗): unstable.

Therefore for the resonance condition associated with α to exist, $k_1 < m_b \alpha^2$ must hold. An example Campbell plot is given in Figure 3.7. It shows ω_{n2} as a function of Ω, and the frequencies that are exciting resonance conditions can be found by looking at the intersections of $\alpha\Omega$ lines with the ω_{n2} curve. If a $\alpha\Omega$ line does not cross the ω_{n2} curve, then the resonance condition associated with it does not exist.

3.4 Conclusions

In this study, in-plane vibrations of a three-blade wind turbine and hub were investigated. The rotor was modeled as a rigid inertia with no stiffness, and the blades were each modeled with a single in-plane mode. Effects of gravity and centrifugal forces were taken into account. The blade and the rotor equations were put in an angle-dependent form for convenience. The blade equations were then separated from the rotor equation.

In the blade equations, gravity introduces direct and parametric excitation terms, which lead to a superharmonic and a subharmonic resonance, respectively. The amplitude and
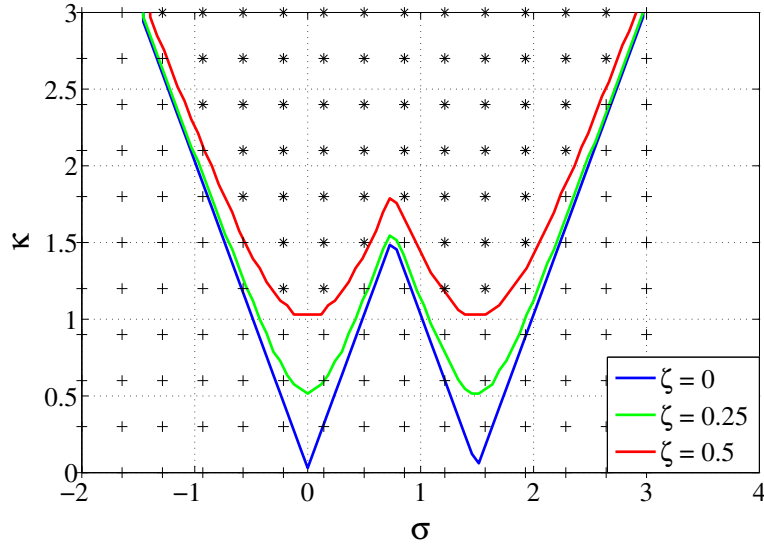
Figure 3.6 Stability plots for the subharmonic response for $\tilde{e} = 1$, $\zeta = 0$, 0.25, 0.5. Simulations are done for $\zeta = 0.5$, $\epsilon = 0.1$, $F_{j0} = 0.1$, $F_{j1} = 0.1$, $\delta = 1.5$, $f = 0.1$, (+): stable, (*): unstable.
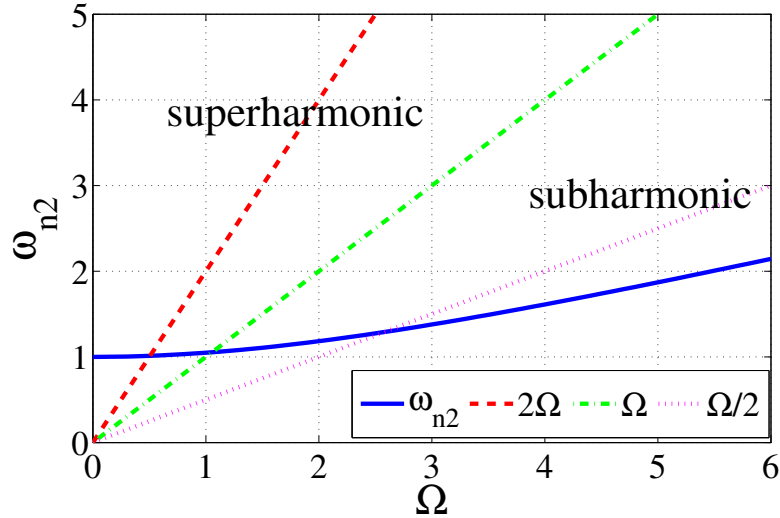
Figure 3.7 Campbell plot showing ω_{n2} as a function of Ω, for $k_0 = 1$, $k_1 = 0.1$, $m_b = 1$.

phase equations were found for the primary, superharmonic and subharmonic resonances. These equations were then solved analytically for each case. For the primary and superharmonic resonances, the blades possess a unison amplitude response which is stable for both cases. However, for the subharmonic case, the blades have a zero response. Stability of this

solution, and the effect of coupling between the blades were investigated. These results were then verified with simulations.

CHAPTER 4

AN ANALYSIS OF THE MATHIEU EQUATION

4.1 Introduction

A linear oscillator model with periodic coefficients in the inertial, damping, and stiffness terms is known as Ince's equation. If the periodic coefficient is only in the stiffness term and there is no damping, the system can be written as a Hill's equation:

$$\ddot{x} + f(t)x = 0, \tag{4.1}$$

where $f(t)$ is periodic. If $f(t) = 1 + \delta \cos \omega t$, Hill's equation reduces to the nondimensional Mathieu equation, where ω is the nondimensional excitation frequency, and δ is the relative strength of parametric excitation.

The Mathieu equation is amenable to Floquet theory, which can be applied to systems of the form

$$\dot{\mathbf{x}} = \mathbf{A}(t)\mathbf{x}, \tag{4.2}$$

where $\mathbf{x}$ is an $N \times 1$ vector and $\mathbf{A}(t)$ is an $N \times N$ matrix that is periodic with period T. According to Floquet theory, Equation (4.2) has solutions of the form $\mathbf{x}_r = e^{\hat{\mu}_r t}\mathbf{p}_r(t)$, for $r = 1, \ldots, N$, where $\mathbf{p}_r(t)$ is an $N \times 1$ vector of period T or $2T$ [75]. Depending on the nature of $\hat{\mu}$, solutions may be stable or unstable. When applied to Hill's equation, Floquet theory suggests that on the boundaries between the stable and unstable regions, the solution is periodic with period T or $2T$ [53]. Therefore the most common approach to the problem is to assume a periodic solution ($\hat{\mu} = 0$), and find the conditions on parameters for existence of the solution by solving a Hill's determinant [46, 54–56]. These conditions result in transition curves between stable and unstable regions on the parameter plane [38, 52, 77–84].

In this study, instead of assuming a periodic solution for describing transitional behavior, the general Floquet solution is kept as it is, with a nonzero $\hat{\mu}$ and a periodic part composed of a series of harmonics.

For a single-degree-of-freedom system, such as the Mathieu equation, the displacement variable x has two independent solutions of the form $x_r = e^{\hat{\mu}_r t} p_r(t) = e^{\hat{\mu}_r t} \sum_{j=-\infty}^{\infty} c_j^{(r)} e^{ij\omega t}$, for $r = 1, 2$. A finite series truncation would represent an approximation. Indeed, the full infinite series solution was used by McLachlan [54] and Coïsson *et al.* [85], to find the stability curves through the transitions in μ values. The characteristic equation and its roots for the solution with infinite harmonics can be found by using McLachlan's calculations [54], using a procedure that involves finding the determinant of an infinite matrix. The solution to the infinite determinant is abstruse, and it may not be amenable to other Floquet type equations, such as the damped Mathieu equation, Ince's equations or parametric excitation with multiple harmonics. Furthermore, it is not convenient for obtaining the eigenvectors, nor a solution for the time response.

To find the time response, and to make the method applicable to other problems, and also more accessible to engineers and scientists with broad backgrounds, an approximate truncated Floquet solution is applied. To check the validity of the truncated solution, its characteristic exponents are compared to those obtained from the infinite series solution. After finding that the results are consistent, the truncated solution is applied to the damped Mathieu equation and to another parametric excitation problem.

Plugging the assumed Floquet solution into the equation of motion, and applying harmonic balance, a homogeneous set of algebraic equations for the unknown c_j's is obtained. These equations are then put in matrix form. To enable a nonzero c_j solution, the determinant of the coefficient matrix is equated to zero, and a characteristic equation for $\hat{\mu}$ is found. Floquet theory suggests that solving this equation for the undamped Mathieu equation results in two distinct $\hat{\mu}$'s, satisfying $\hat{\mu}_1 = -\hat{\mu}_2 + i\omega k$, where k is an integer, and by which the $k = 0$ case defines principal exponents. For $\text{Re}(\hat{\mu}) \neq 0$, the solution grows exponentially,

whereas for $\text{Re}(\hat{\mu}) = 0$, the solution is bounded. Therefore transition curves can be found by examining changes in $\hat{\mu}$ in the parameter space. Associated with each of μ_1 and μ_2 are distinct sets of coefficients $c_j^{(1)}$ and $c_j^{(2)}$, which, if found, would complete the expressions of x_1 and x_2 which could then be combined to express the response to initial conditions.

A truncated Floquet-type solution was also used by Insperger and Stépán to find the stability regions of the undamped and damped Mathieu equations with a time delay [86, 87]. They plugged the assumed solution into the equations with delay terms, and applied a harmonic balance procedure. Then, assuming a periodic solution, they determined the relations between the parameters on the stability boundaries. In this study, instead of assuming a periodic solution and finding parameters that define transitional behavior, a generally non-periodic solution is retained to find the roots for the characteristic exponents, $\hat{\mu}'s$.

4.2 Floquet-based Series Solution

In this section, the series solution, $x = e^{\hat{\mu}t} \sum_{j=-n}^{n} c_j e^{ij\omega t}$, is applied to the Mathieu equation. The nondimensional undamped Mathieu equation,

$$\ddot{x} + (1 + \delta \cos \omega t)\, x = 0, \tag{4.3}$$

can be written in state space form as

$$\dot{\mathbf{x}} = \begin{pmatrix} \dot{x} \\ \ddot{x} \end{pmatrix} = \begin{bmatrix} 0 & 1 \\ -(1 + \delta \cos \omega t) & 0 \end{bmatrix} \begin{pmatrix} x \\ \dot{x} \end{pmatrix} = \mathbf{A}(t)\mathbf{x}, \tag{4.4}$$

for which $\mathbf{A}(t)$ has period $T = 2\pi/\omega$.

In the following sections, the infinite series solution $(n \to \infty)$ is reviewed. Then, a truncated solution is applied, and its stability characteristics are compared to those of the infinite series solution. The truncated solution leads to an eigenvalue problem, by solving which the two independent elements of the time response can be constructed, and then combined for responses to specified initial conditions.

4.2.1 Infinite Series Solution

In this case, the assumed solution is

$$x_r(t) = e^{i\mu_r t} \sum_{j=-\infty}^{\infty} c_j^{(r)} e^{ij\omega t}, \tag{4.5}$$

where $\mu_r = -i\hat{\mu}_r$, such that the exponential part is expressed more conveniently for the analysis as $e^{i\mu_r t}$ instead of $e^{\hat{\mu}_r t}$. According to Floquet theory [53], there exist two distinct μ's, which satisfy

$$e^{(i\mu_1+i\mu_2)T} = \exp\left(\int_0^T \text{tr}(A(s))ds\right). \tag{4.6}$$

Since $\text{tr}(A) = 0$ for the undamped Mathieu equation, the relation between the μ's is $(i\mu_1 + i\mu_2)T = 2i\pi k$ (i.e. $\mu_1 + \mu_2 = 0 \pm \omega k$).

Inserting the assumed solution into Equation (4.3) and balancing coefficients of $e^{ij\omega t}$ leads to the jth equation in the form

$$\frac{\delta}{2}c_{j-1} + \left[1 - (\mu + j\omega)^2\right] c_j + \frac{\delta}{2}c_{j+1} = 0, \tag{4.7}$$

for $j = -\infty, \ldots, \infty$,

In matrix form,

$$\begin{bmatrix} \ddots & \ddots & 0 & \cdots & 0 \\ a_{-1} & 1 & a_{-1} & 0 & \vdots \\ 0 & a_0 & 1 & a_0 & 0 \\ \vdots & 0 & a_1 & 1 & a_1 \\ 0 & \cdots & 0 & \ddots & \ddots \end{bmatrix} \begin{pmatrix} \vdots \\ c_{-1} \\ c_0 \\ c_1 \\ \vdots \end{pmatrix} = \begin{pmatrix} 0 \\ 0 \\ \vdots \\ \vdots \\ 0 \end{pmatrix}, \tag{4.8}$$

where

$$a_j = \frac{\delta}{2\left(1 - (\mu + j\omega)^2\right)}. \tag{4.9}$$

Note that each c_j equation is divided by $1 - (\mu + j\omega)^2$ to make the diagonal elements 1. This is required to show that the infinite determinant is convergent [54]. For non-zero

c_j's, the determinant of the coefficient matrix has to be zero. Much like an eigenvalue problem, this yields an equation involving μ. A value of μ satisfying this condition is called characteristic exponent. According to McLachlan [54], and works cited therein, μ is given as

$$\mu = \cos^{-1}\left(1 - \Delta(0)\left(1 - \cos[\frac{2\pi}{\omega}]\right)\right), \tag{4.10}$$

where $\Delta(0)$ is the determinant of the matrix for $\mu = 0$, which, for small δ, can be approximated by

$$\Delta(0) \approx 1 - \frac{\pi \cot\left(\frac{\pi}{\omega}\right)\delta^2}{2\omega\left(4 - \omega^2\right)}. \tag{4.11}$$

By solving Equation (4.10) and Equation (4.11) together, two distinct μ values, satisfying $\mu_1 = -\mu_2$, can be found for any (δ, ω) pair. Since μ appears in the term $e^{i\mu t}$, it gives information about the frequency of the response, and stability. For $\text{Im}(\mu) \neq 0$, the solution is unstable, whereas $\text{Im}(\mu) = 0$ leads to a bounded solution. Using this information, approximate transition curves between stable and unstable regions can be plotted on the $\delta - \omega$ plane. The approximation improves as δ decreases in magnitude. Although this analysis provides a closed form solution for characteristic exponents, McLachlan [54] did not provide the associated eigenvectors, and time responses to initial conditions. Therefore to obtain the frequency content and time response, a truncated solution is useful, since it is easier to solve the eigenvalue problem.

4.2.2 Truncated Series Solution

While an infinite determinant leads to a closed-form expression approximating μ in the case of the undamped Mathieu equation, it may not be so if additional terms were included in Equation (4.3). In such case, a truncated solution may be practical. Here a truncated series solution is applied to Equation (4.3) and it is compared to the infinite series approximation.

A truncated solution has the form

$$x_r(t) = e^{i\mu_r t}\sum_{j=-n}^{n}c_j e^{ij\omega t}. \tag{4.12}$$

53

Inserting this into Equation (4.3) leads to

$$
\mathbf{Kc} = \begin{bmatrix} k_{-n} & \frac{\delta}{2} & 0 & 0 & 0 \\ \frac{\delta}{2} & \ddots & \frac{\delta}{2} & 0 & 0 \\ 0 & \frac{\delta}{2} & k_0 & \ddots & 0 \\ 0 & 0 & \ddots & \ddots & \frac{\delta}{2} \\ 0 & 0 & 0 & \frac{\delta}{2} & k_n \end{bmatrix} \begin{pmatrix} c_{-n} \\ \vdots \\ c_0 \\ \vdots \\ c_n \end{pmatrix} = \begin{pmatrix} 0 \\ \vdots \\ 0 \\ \vdots \\ 0 \end{pmatrix}, \tag{4.13}
$$

where $k_j = 1 - (\mu_1 + j\omega)^2$, for $j = -n, \dots, n$. Notice that this is consistent with Equation (4.8), except the rows (i.e. c_j equations), are not divided by $(1 - (\mu + j\omega)^2)$.

Nonzero solutions of vector $\mathbf{c}$ require the determinant of $\mathbf{K}$ to be zero. This is a finite determinant, and by equating it to 0, the characteristic equation for μ is found. The characteristic equation is a $(2n + 1)^{th}$ order polynomial in terms of μ^2, which results in $(4n + 2)$ roots satisfying $\mu_{2r-1} = -\mu_{2r}$, $r = 1, 2 \dots, 2n + 1$. Yet, Floquet theory states that the number of μ's should be equal to the dimension N of the state space, which in the case of the Mathieu equation is 2. While the truncated solution results in $(4n + 2)$ roots for μ, it turns out that not all of them are independent. As the number n of assumed harmonics is increased, the characteristic exponents converge to a set of elements which satisfy

$$
\mu_i = \pm\mu_r \pm k\omega, \tag{4.14}
$$

where k is an integer. The difference $\pm k\omega$ does not lead to distinct solutions, since $e^{ik\omega t}$ is of period T and can be put into $\mathbf{p}(t)$. To see this, consider $e^{i\mu t}p_1(t) = e^{i(\mu_r \pm k\omega t)} \sum_{j=-n}^{j=n} e^{ij\omega t} = e^{i\mu_r t} \sum_{j=-n}^{j=n} e^{i(j\pm k)\omega t} = e^{i\mu_r t} p_2(t)$, for which $p_1(t)$ and $p_2(t)$ have the same period. Therefore there are effectively two distinct principal roots, $\mu_1 = -\mu_2$. For a few (ω, δ) pairs, the principal roots are given in Table 4.1, for $n = 1, \dots, 4$. In each case, the roots converge to their final values for $n = 2$. Therefore, $n = 2$ truncated solution is studied here to compare with the infinite series solution.

Equation (4.13) is essentially an eigenvalue problem (EVP), with principal eigenvalues $\mu_1 = -\mu_2$. To find the relationship between the eigenvectors satisfying $\mathbf{K}(\mu_r)\mathbf{c}_r = \mathbf{0}$, the

	Principal characteristic exponents, μ_r			
	$n = 1$	$n = 2$	$n = 3$	$n = 4$
$\omega = 0.6, \delta = 0.4$	± 0.3752	± 0.2250	± 0.2119	± 0.2118
$\omega = 0.8, \delta = 0.6$	± 0.1436	± 0.1671	± 0.1673	± 0.1673
$\omega = 1.3, \delta = 0.8$	± 0.3896	± 0.3657	± 0.3656	± 0.3656
$\omega = 2.5, \delta = 0.7$	± 1.0606	± 1.0611	± 1.0611	± 1.0611

Table 4.1 Principal characteristic exponents μ_1 and μ_2 for truncated solutions with $n = 1, \ldots, 4$

equation for $n = 2$ is evaluated for both principal μ's. For μ_1, $\mathbf{c}_1$ satisfies

$$
\begin{bmatrix}
k_{-2} & \frac{\delta}{2} & 0 & 0 & 0 \\
\frac{\delta}{2} & k_{-1} & \frac{\delta}{2} & 0 & 0 \\
0 & \frac{\delta}{2} & k_0 & \frac{\delta}{2} & 0 \\
0 & 0 & \frac{\delta}{2} & k_1 & \frac{\delta}{2} \\
0 & 0 & 0 & \frac{\delta}{2} & k_2
\end{bmatrix}
\begin{pmatrix}
c_{-21} \\
c_{-11} \\
c_{01} \\
c_{11} \\
c_{21}
\end{pmatrix}
=
\begin{pmatrix}
0 \\
0 \\
0 \\
0 \\
0
\end{pmatrix}.
\tag{4.15}
$$

On the other hand, the eigenvector associated with $\mu_2 = -\mu_1$ satisfies

$$
\begin{bmatrix}
k_2 & \frac{\delta}{2} & 0 & 0 & 0 \\
\frac{\delta}{2} & k_1 & \frac{\delta}{2} & 0 & 0 \\
0 & \frac{\delta}{2} & k_0 & \frac{\delta}{2} & 0 \\
0 & 0 & \frac{\delta}{2} & k_{-1} & \frac{\delta}{2} \\
0 & 0 & 0 & \frac{\delta}{2} & k_{-2}
\end{bmatrix}
\begin{pmatrix}
c_{-22} \\
c_{-12} \\
c_{02} \\
c_{12} \\
c_{22}
\end{pmatrix}
=
\begin{pmatrix}
0 \\
0 \\
0 \\
0 \\
0
\end{pmatrix}.
\tag{4.16}
$$

The difference between Equation (4.15) and Equation (4.16) is that the order of the diagonal entries is reversed, since $k_j^{(1)} = 1 - (\mu_1 + j\omega)^2 = 1 - (-\mu_2 + j\omega)^2 = 1 - (\mu_2 - j\omega)^2 = k_{-j}^{(2)}$. Therefore the equations for elements of $\mathbf{c}_2$ are the same with those associated with the elements of $\mathbf{c}_1$, except that the order of the equations is changed. Specifically, if

$$
\mathbf{c}_1 = [c_{-21} \quad c_{-11} \quad c_{01} \quad c_{11} \quad c_{21}]^T,
\tag{4.17}
$$

then

$$
\mathbf{c}_2 = [c_{21} \quad c_{11} \quad c_{01} \quad c_{-11} \quad c_{-21}]^T.
\tag{4.18}
$$

The pattern carries over for other values of n.

The general solution is composed of two independent solutions,

$$x(t) = A_1 x_1(t) + A_2 x_2(t), \tag{4.19}$$

where $x_j(t) = e^{i\mu_j t} \mathbf{c}_j(t)^{\mathrm{T}} \cdot [e^{-2i\omega t}, e^{-i\omega t}, 1, e^{i\omega t}, e^{2i\omega t}]^{\mathrm{T}}$, and A_1 and A_2 can be determined from the initial conditions.

As an example, the initial conditions $x(0) = 0$ and $\dot{x}(0) = v_0$ result in $A_1 = -A_2$ and the solution is given by

$$x(t) = A_1 \left[\left(c_{-21} e^{i(\mu_1 - 2\omega)t} + c_{-11} e^{i(\mu_1 - \omega)t} + c_{01} e^{i\mu_1 t} \right. \right.$$

$$\left. + c_{11} e^{i(\mu_1 + \omega)t} + c_{21} e^{i(\mu_1 + 2\omega)t} \right) - \left(c_{21} e^{i(-\mu_1 - 2\omega)t} \right.$$

$$+ c_{11} e^{i(-\mu_1 - \omega)t} + c_{01} e^{-i\mu_1 t} + c_{-11} e^{i(-\mu_1 + \omega)t}$$

$$\left. \left. + c_{-21} e^{i(-\mu_1 + 2\omega)t} \right) \right], \tag{4.20}$$

where

$$A_1 = v_0 / \left(2i \sum_{j=-2}^{2} (\mu_1 + j\omega) c_{j1} \right). \tag{4.21}$$

For the case of a stable solution $(\mathrm{Im}(\mu) = 0)$, this reduces to

$$x(t) = \left(v_0 / \sum_{j=-2}^{2} (\mu_1 + j\omega) c_{j1} \right) [c_{-21} \sin(\mu_1 - 2\omega)t$$

$$+ c_{-11} \sin(\mu_1 - \omega)t + c_{01} \sin\mu_1 t + c_{11} \sin(\mu_1 + \omega)t$$

$$+ c_{21} \sin(\mu_1 + 2\omega)t]. \tag{4.22}$$

Thus, this truncated expansion predicts response frequencies $\mu_1 - 2\omega$, $\mu_1 - \omega$, μ_1, $\mu_1 + \omega$, and $\mu_1 + 2\omega$.

Depending on the initial conditions, A_r's might be real or complex, and together with $\mathbf{c}_r$'s they determine the amplitudes and the phases of the solution harmonics. Thus, by looking at the individual elements of $\mathbf{c}_r$'s, the dominant harmonics can be determined.

4.3 Response Characteristics of the Undamped Mathieu Equation

Solving the EVP given in Equation (4.13) allows us to predict the characteristics of the response, such as the response frequencies and stability of the solution. These characteristics are investigated for the $n = 2$ truncated solution and the infinite series solution.

4.3.1 Stability Analysis

Stability of the assumed solution depends on the value of μ. For a μ having a zero imaginary part, $e^{i\mu t}$ is periodic and the solution is bounded, whereas a nonzero imaginary part leads to an exponentially growing solution, since the principal values are $\mu_1 = -\mu_2$. Therefore the transition curves between μ's having zero and nonzero imaginary parts are essentially the boundaries between stable and unstable regions. These boundaries are plotted for the infinite solution and for the $n = 2$ approximation, and these are compared to the curves obtained from the classical Hill's determinant solution ($n = 2$), as given in Figure 4.1. While there are an infinite number of transition curves, the truncated solution is capable of predicting $2n$ of them. As δ increases, the deviation between the transition curves gets larger, since the approximation in each solution is valid for small δ.

4.3.2 Response Frequencies

The assumed solution is a product of an exponential part and a periodic part. The frequency of the response is a combination of the frequencies of the two parts. The exponential part is of frequency $\text{Re}(\mu)$, and by using trigonometric identities, the predicted response frequencies are $\text{Re}(\mu) + j\omega$, where $j = \pm 1, 2 \ldots, n$. For a given value of δ, response frequencies can be plotted as a function of ω. As an example, for $\delta = 0.8$, the predicted lower response frequencies are plotted versus ω in Figure 4.2.

Figure 4.2 shows that with variations in ω, two frequency branches can collide and merge into one branch. These frequency collisions correspond to stability transitions. The top
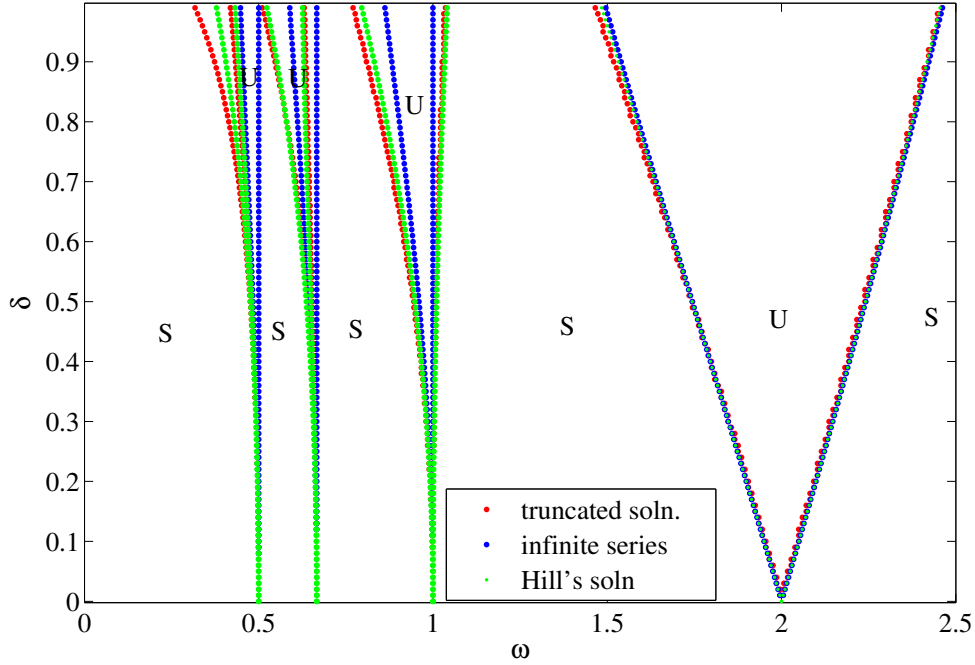
Figure 4.1 Transition curves for the $n = 2$ Floquet-based approximation, infinite series solution, and the $n = 2$ Hill's determinant solution.

branch in Figure 4.2 has no collisions. If we choose a larger value of n, we expect to see more branches with which this top branch could collide. Notice that in the unstable regions, the solution consists of an exponential growth and a periodic part with period T or $2T$, which is known since the Floquet multipliers are real positive or negative for the unstable Hill's equation [52]. The response frequencies coming from the periodic part can be clearly seen from the Figure 4.2. For example near the $\omega = 2$ instability, the response frequencies are $\omega/2$, $3\omega/2$ and $5\omega/2$, whereas near the $\omega = 1$ instability, the frequencies are ω, 2ω and 3ω.

To validate the truncated solution, for a number of (δ, ω) pairs, frequencies of stable responses are compared to those found from the fast Fourier transforms (FFTs) of the numerical solutions, as shown in Table 4.2.

By solving the eigenvalue problem given in Equation (4.13) for $n = 2$, the eigenvectors for the truncated solution are found for (ω, δ) pairs given in Table 4.2. The response is then constructed using Equation (4.20) and Equation (4.22) with initial conditions $x(0) = 0$, and
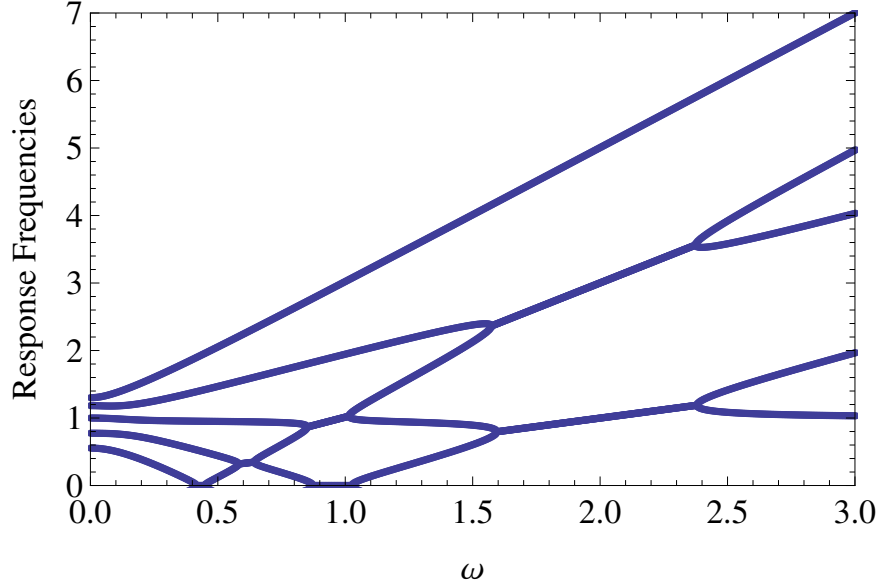
Figure 4.2 Analytically predicted response frequencies for $\delta = 0.8$, $n = 2$.

ω	δ	Lowest Response Frequencies (Hz)		
		$n = 2$	$n = \infty$	Numerical
0.6	0.4	$0.225, 0.388, 0.825,$ $0.988, 1.425$	$0.211, 0.389, 0.811,$ $0.988, 1.411$	$0.211, 0.388, 0.812,$ $0.988, 1.412$
0.8	0.6	$0.167, 0.655, 0.966,$ $1.455, 1.767$	$0.173, 0.627, 0.973,$ $1.423, 1.773$	$0.171, 0.637, 0.969,$ $1.432, 1.768$
1.3	0.8	$0.366, 0.934, 1.690,$ $2.224, 2.966$	$0.369, 0.931, 1.669,$ $2.231, 2.969$	$0.365, 0.930, 1.661,$ $2.265, 2.966$
2.5	0.7	$1.061, 1.439, 3.561,$ $3.945, 6.005$	$1.061, 1.439, 3.561,$ $3.939, 6.061$	$1.061, 1.440, 3.561,$ $3.939, 6.060$

Table 4.2 Lowest response frequencies obtained from the $n = 2$ and $n = \infty$ Floquet solutions, and FFTs of numerical solutions

$\dot{x}(0) = 1$. These solutions are then compared with those found from the numerical solution. The time responses and FFT plots are given in Figures 4.3 and 4.4. The results are consistent for larger ω values, whereas the predicted frequency content and associated amplitudes are a little bit off for smaller values of ω. To achieve better results in the small ω region, the number of harmonics assumed in the truncated solution should be increased. To show the effect of number of assumed harmonics, the free response and FFT plots for $\omega = 0.4$, $\delta = 0.6$ are given for $n = 3$ in Figure 4.5. Comparing these plots to Figure 4.3(a) and 4.4(a), it can

be seen that with the added harmonic, the assumed solution was able to capture the 6th peak in the FFT plot, and the time response matched better with the numerical solution.
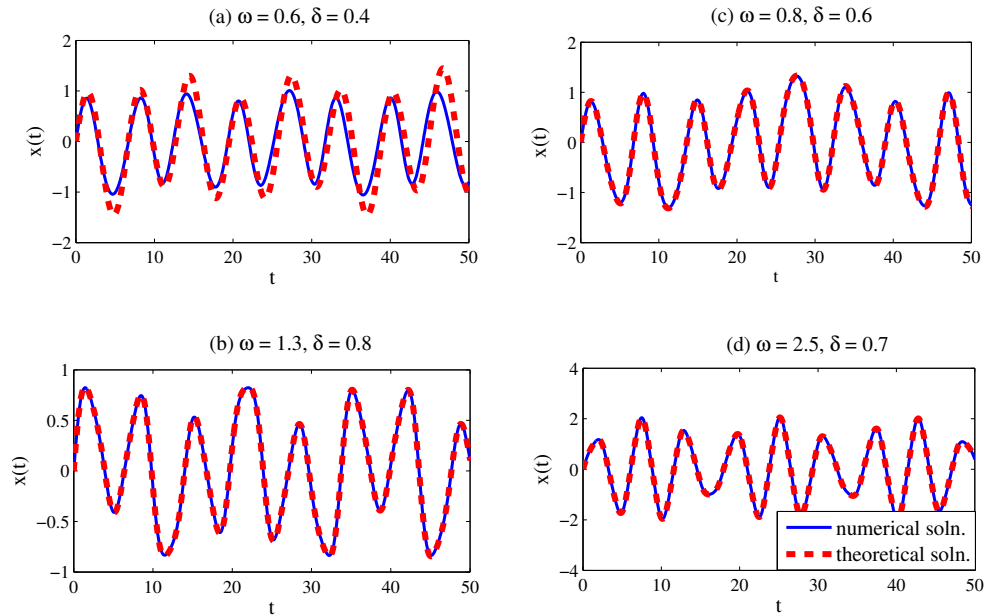
Figure 4.3 Numerical and theoretical ($n = 2$) solutions of the undamped Mathieu equation for $n = 2$.

4.4 Damped Mathieu Equation

A truncated expansion may be desirable for oscillators other than the undamped Mathieu equation, which may therefore not have a simple closed form expression from the infinite determinant. For example the existence of such an expression is not obvious for the damped Mathieu equation. Here, a truncated solution with $n = 2$ is assumed for the damped Mathieu equation, which is given by

$$\ddot{x} + 2\zeta\dot{x} + (1 + \delta \cos \omega t)\, x = 0. \tag{4.23}$$
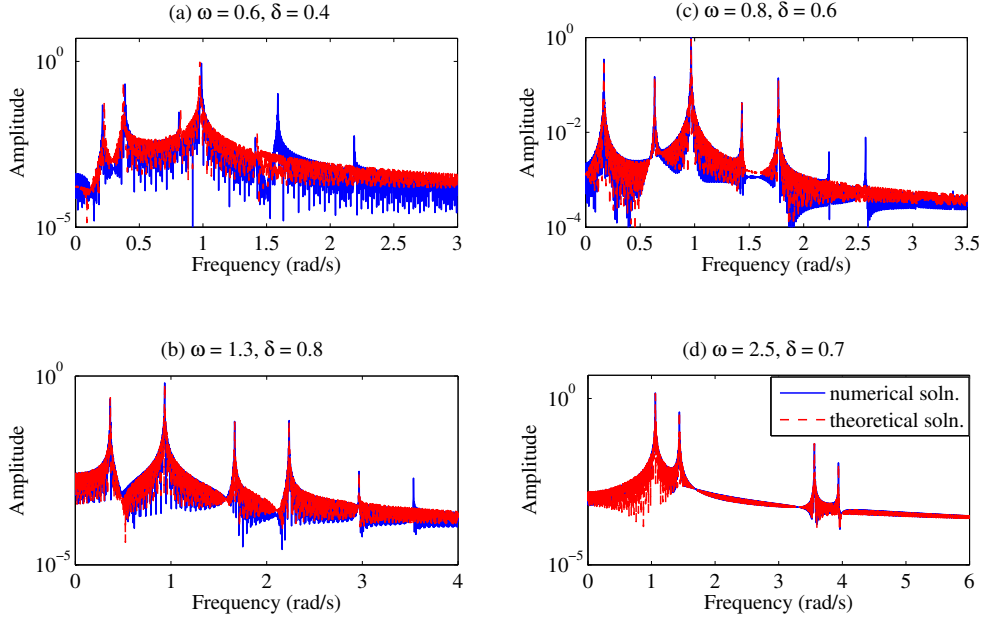
Figure 4.4 FFTs of numerical and theoretical ($n = 2$) solutions of the undamped Mathieu equation for $n = 2$.

Inserting the $n = 2$ expansion, Equation (4.12), into Equation (4.23) results in

$$
\begin{bmatrix}
b_{-2} & \frac{\delta}{2} & 0 & 0 & 0 \\
\frac{\delta}{2} & b_{-1} & \frac{\delta}{2} & 0 & 0 \\
0 & \frac{\delta}{2} & b_0 & \frac{\delta}{2} & 0 \\
0 & 0 & \frac{\delta}{2} & b_1 & \frac{\delta}{2} \\
0 & 0 & 0 & \frac{\delta}{2} & b_2
\end{bmatrix}
\begin{pmatrix}
c_{-2} \\
c_{-1} \\
c_0 \\
c_1 \\
c_2
\end{pmatrix}
=
\begin{pmatrix}
0 \\
0 \\
0 \\
0 \\
0
\end{pmatrix},
\tag{4.24}
$$

where

$$
b_j = 1 - (\mu + j\omega)^2 + i2\zeta(\mu + j\omega).
\tag{4.25}
$$

In this case the condition given in Equation (4.6) results in $\mu_1 + \mu_2 = i2\zeta \pm k\omega$, since $\mathrm{tr}(A(t)) = -2\zeta$. This causes changes in the transition curves, leading to larger stable regions for larger damping ratios. For damping ratios $\zeta = 0.005$, $\zeta = 0.025$, and $\zeta = 0.05$, transition curves are given in Figure 4.6. The curves resulting from the truncated solution are consistent with those found in the literature.

61
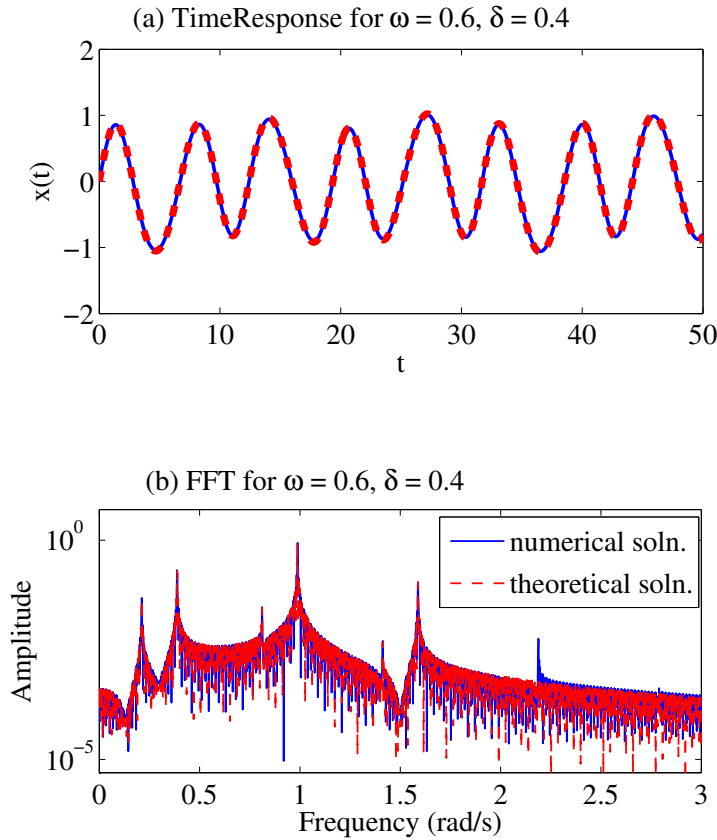
Figure 4.5 Free response and FFT plots for $\omega = 0.4$, $\delta = 0.6$, with $n = 3$ harmonics.

The time constants, and therefore the decay or growth rates, can be determined from the characteristic exponents. The imaginary parts of the μ's govern the exponential part of the solution. As an example, the decay and growth factors are plotted as a function of ω for $\zeta = 0.05$ and $\delta = 0.8$, in Figure 4.7. It can be seen from the figure that the two factors always add up to -2ζ, which is consistent with the Floquet theory. Notice that in some regions we have $\text{Im}(\mu_1) = \text{Im}(\mu_2) = \zeta$, which means the response has a single decay rate independent of ω and δ. To visualize this, for $\zeta = 0.025$, initial condition responses are plotted in Figure 4.8 for two different cases. It can be clearly seen that, the two responses are decaying in the same envelope, $\mathrm{e}^{-0.025t}$. In other regions (i.e. $\text{Im}(\mu_1) \neq \text{Im}(\mu_2)$), there

62
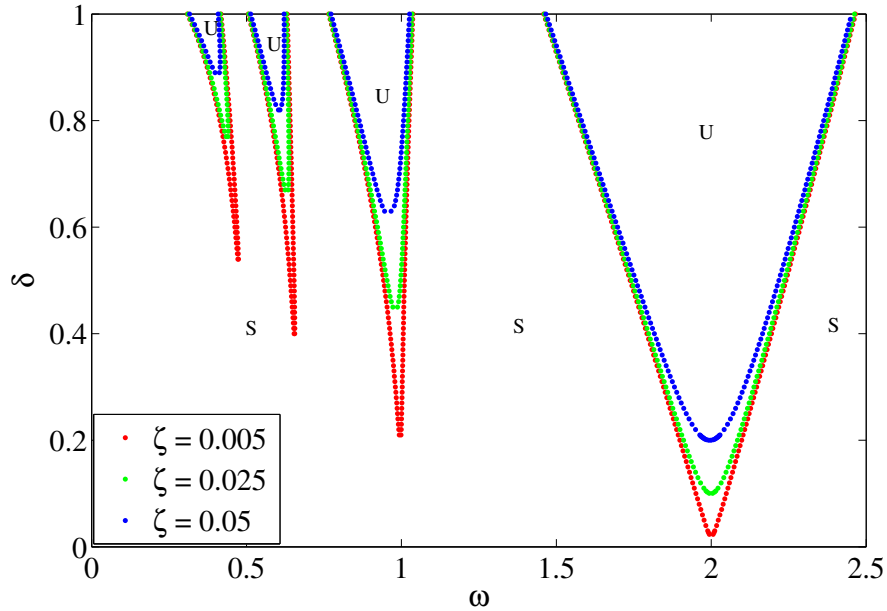
Figure 4.6 Transition curves for the damped Mathieu equation for $\zeta = 0.005$, $\zeta = 0.025$, and $\zeta = 0.05$, approximated with $n = 2$.

are two time constants. This means that for $\text{Im}(\mu_1) > \text{Im}(\mu_2) > 0$, the solution is stable and is composed of a slow and a fast part, whereas for $\text{Im}(\mu_1) > 0 > -\text{Im}(\mu_2)$, the solution is unstable. In the case of Figure 4.8 (a) and (b), $\text{Im}(\mu_1) = \text{Im}(\mu_2) = \zeta$, therefore the response has only one decay rate. However in Figure 4.8 (c) and (d), there are two different decay rates, and the response is dominated by the one having the slower decay rate. For parameter values $\omega = 1, \delta = 0.3, \zeta = 0.025$, the imaginary parts are $\text{Im}(\mu_1) = 0.019$ and $\text{Im}(\mu_2) = 0.031$. The time response has the effects of both decaying parts at the beginning, but then it is dominated by the slowly decaying one, $\text{e}^{-0.019t}$. The same effect can be seen in Figure 4.8 (d), where the imaginary parts are $\text{Im}(\mu_1) = 0.0125$ and $\text{Im}(\mu_2) = 0.0875$. The corresponding FFT plots are given in Figure 4.9.
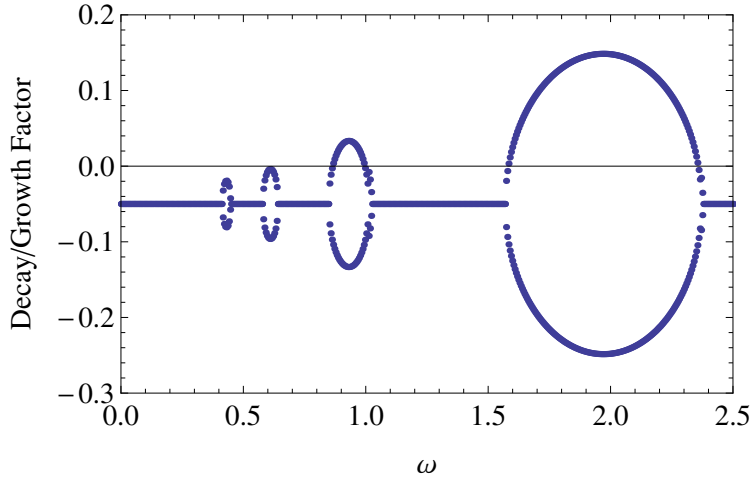
Figure 4.7 Decay and growth factors for $\zeta = 0.05$ and $\delta = 0.8$.
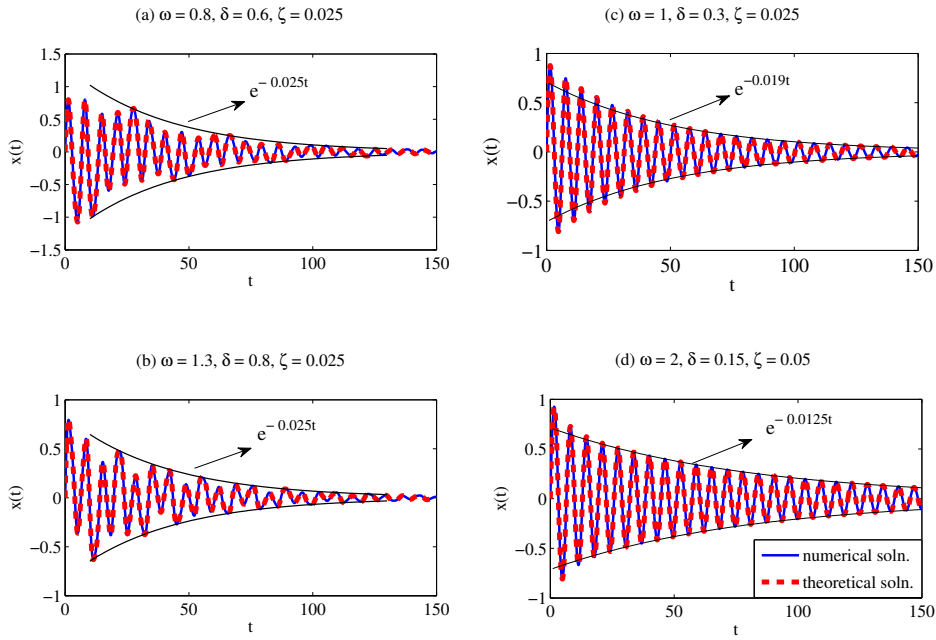
Figure 4.8 Numerical and theoretical $(n = 2)$ solutions of the damped Mathieu equation.

4.5   Parametric Excitation with Two Harmonics

The truncated solution is applied to the problem

$$\ddot{x} + (1 + \delta \cos \omega t + \gamma \delta \cos 2\omega t)\, x = 0. \qquad (4.26)$$
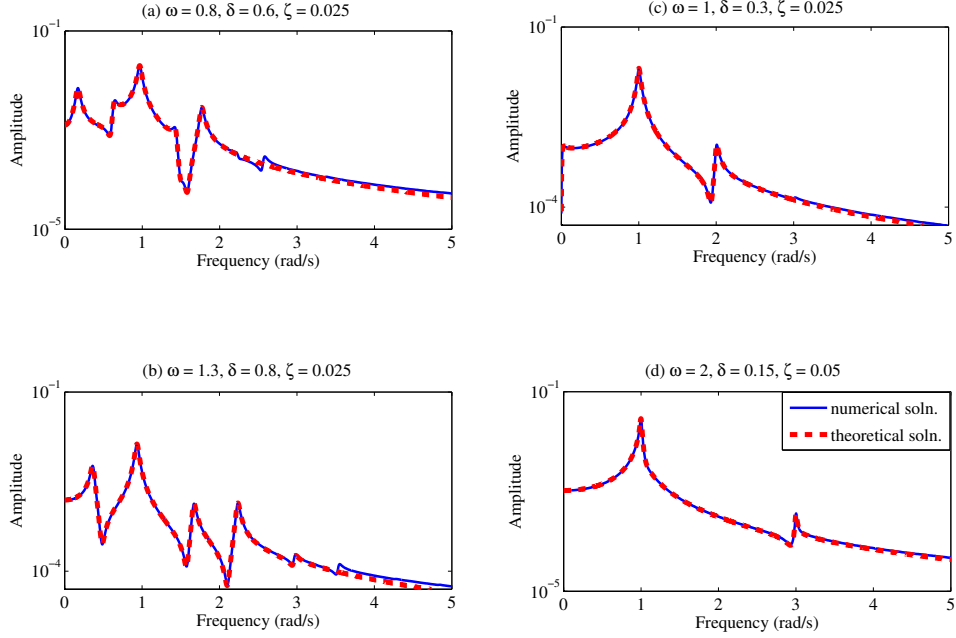
Figure 4.9 FFT of numerical and theoretical ($n = 2$) stable solutions of the damped Mathieu equation.

This system is suspected to have possible simultaneous interactions with the effects of ω and 2ω excitation terms.

Performing harmonic balance, the matrix equation is found as

$$
\begin{bmatrix}
k_{-2} & \frac{\delta}{2} & \frac{\gamma\delta}{2} & 0 & 0 \\
\frac{\delta}{2} & k_{-1} & \frac{\delta}{2} & \frac{\gamma\delta}{2} & 0 \\
\frac{\gamma\delta}{2} & \frac{\delta}{2} & k_0 & \frac{\delta}{2} & \frac{\gamma\delta}{2} \\
0 & \frac{\gamma\delta}{2} & \frac{\delta}{2} & k_1 & \frac{\delta}{2} \\
0 & 0 & \frac{\gamma\delta}{2} & \frac{\delta}{2} & k_2
\end{bmatrix}
\begin{pmatrix}
c_{-21} \\
c_{-11} \\
c_{01} \\
c_{11} \\
c_{21}
\end{pmatrix}
=
\begin{pmatrix}
0 \\
0 \\
0 \\
0 \\
0
\end{pmatrix},
\tag{4.27}
$$

where $k_j = 1 - (\mu_1 + j\omega)^2$. The characteristic exponents are found by equating the determinant to zero. As in the undamped Mathieu equation, the condition given in Equation (4.6) results in $\mu_1 = -\mu_2$.

For $(\omega = 0.8, \delta = 0.6, \gamma = 0.5)$ and $n = 3$, and for $(\omega = 1.5, \delta = 0.5, \gamma = 1)$ and $n = 2$, the responses for $x(0) = 0$, $\dot{x}(0) = 1$ initial conditions and FFT plots are given in Figure 4.10.

The results are consistent with the numerical results, which means the proposed method can predict the response for this problem as well. Comparing Figure 4.10 (a) with Figure 4.3 (c) shows that, in this case, the second parametric excitation harmonic results in a slightly suppressed response. It is possible that multiple harmonic excitations may have some useful effects. Future research will be conducted to examine the behavior of this system.
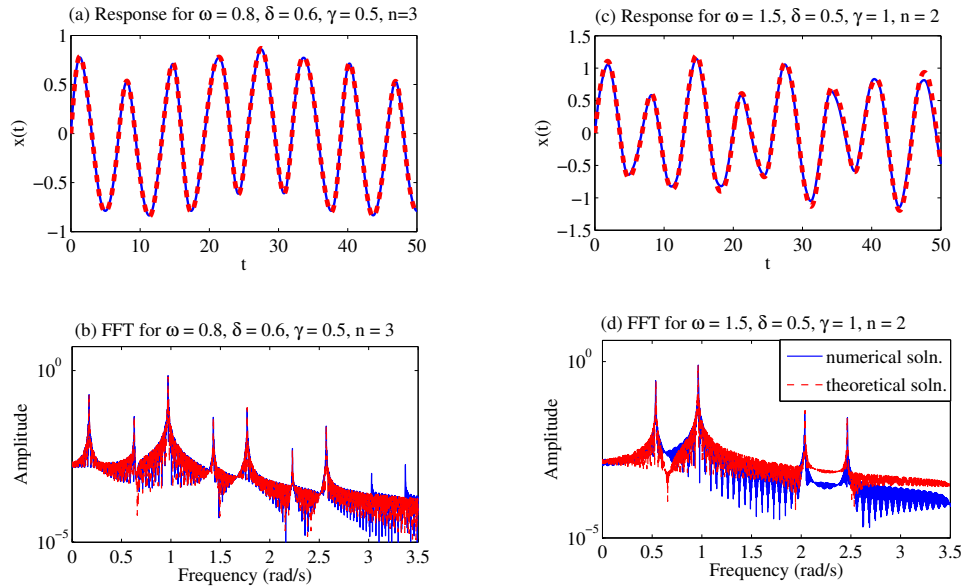
Figure 4.10 Numerical and theoretical solutions of the two-frequency Mathieu equation.

4.6   Conclusions

A truncated Floquet solution has been applied to the analysis of the Mathieu equation. The form of the solution involves an unknown Floquet exponential term times a truncated Fourier series with unknown coefficients. The Floquet exponent and Fourier coefficients are then determined by an eigenvalue problem. From this information, the stability and the response frequencies and their relative strengths can be approximated.

This approach was applied to the undamped Mathieu equation and the frequencies and associated strengths were estimated as functions of the excitation amplitude and frequency.

The theoretical approximation to the response frequencies and amplitudes compared favorably to numerical simulations. Information about the stability transitions was also extracted and compared to existing approximations. The approach was then successfully applied to the damped Mathieu equation and a two-frequency Mathieu equation.

The approach given here is a simplification of an existing but uncommon solution involving an infinite series, which results in an infinite determinant approximation which is applicable only to the undamped Mathieu equation. This infinite-series approach had been applied in an effort to obtain stability transition curves. The truncated series approach of this paper is expected to be applicable to other parametrically excited oscillators, such as Ince's equation, or parametric excitation with multiple harmonics. It also does not involve the enigmatic analysis of the infinite determinant, thereby making the approach more accessible to engineers and scientists with broad backgrounds.

CHAPTER 5

APPROXIMATE GENERAL RESPONSES OF MULTI-DEGREE-OF-FREEDOM SYSTEMS WITH PARAMETRIC STIFFNESS

5.1 Introduction

In this study, general solutions to Mathieu-type multi-degree-of-freedom (MDOF) systems of the form

$$\mathbf{M}\ddot{\mathbf{x}} + \mathbf{K}(t)\mathbf{x} = \mathbf{0}, \tag{5.1}$$

are investigated, where $\mathbf{x}$ is a $d \times 1$ vector of coordinate displacements, where d is the number of degrees of freedom, and $\mathbf{M}$ and $\mathbf{K}(t)$ are the mass and time-varying stiffness matrices. The aim is to obtain a general initial condition response as well as the stability characteristics of the system. To this end, instead of assuming a periodic solution, a Floquet-type solution is assumed as

$$\mathbf{x}_r = e^{i\mu_r t} \sum_{l=-n}^{n} \mathbf{c}_l^{(r)} e^{il\omega t}, \qquad r = 1, \dots, 2d \tag{5.2}$$

where the index r distinguishes between $2d$ independent Floquet solution terms for an d-degree-of-freedom system. The assumed solution is plugged into the equations of motion, and by applying harmonic balance, the characteristic exponents, μ_r, and associated Fourier coefficients, $\mathbf{c}_l^{(r)}$, are determined. The response to an arbitrary initial condition can then be found by considering a linear combination of the $\mathbf{x}_r$. The same method was applied to the SDOF undamped and damped Mathieu equations [88] (See also Chapter 4).

5.2 Analysis

We demonstrate the response analysis procedure can be explained by going over example MDOF systems, namely a two-DOF case and a three-DOF system.

5.2.1   Two-Degree-of-Freedom Example

To this end, a mass-spring chain as shown in Figure 5.1, with periodic stiffness is used. The
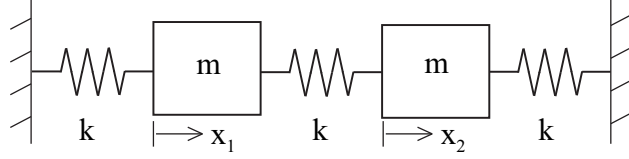
Figure 5.1 A two DOF spring-mass chain.

equations of motion are

$$\ddot{x}_1 + k(2x_1 - x_2) = 0, \tag{5.3}$$

$$\ddot{x}_2 + k(2x_2 - x_1) = 0, \tag{5.4}$$

where $m = 1$ and $k = 1 + \delta \cos \omega t$. For the case of $\delta = 0$, the system has constant coefficients and the modal frequencies are well defined as $\omega_1 = 1$ and $\omega_2 = \sqrt{3}$, with mode shapes $\mathbf{u}_1 = (1 \quad 1)^{\mathrm{T}}$ and $\mathbf{u}_2 = (1 \quad -1)^{\mathrm{T}}$.

To find the response, a Floquet type solution with finite harmonics, as given in Equation (5.2), is assumed and plugged into the equations. Specifically, in this example, we seek elements of $\mathbf{x}(t) = [x_1(t) \quad x_2(t)]^{\mathrm{T}}$ as $x_1(t) = \mathrm{e}^{\mathrm{i}\mu t} \sum_{l=-n}^{n} c_{1,l}\mathrm{e}^{\mathrm{i}l\omega t}$ and $x_2(t) = \mathrm{e}^{\mathrm{i}\mu t} \sum_{l=-n}^{n} c_{2,l}\mathrm{e}^{\mathrm{i}l\omega t}$. Applying harmonic balance, governing equations for $c_{j,l}$'s are found. In matrix form,

$$\mathbf{Ac} = \begin{bmatrix} A_{11} & A_{12} \\ A_{21} & A_{22} \end{bmatrix} \begin{pmatrix} \mathbf{c}_1 \\ \mathbf{c}_2 \end{pmatrix} = \begin{pmatrix} \mathbf{0} \\ \mathbf{0} \end{pmatrix}, \tag{5.5}$$

where $\mathbf{c}_j = [c_{j,-n} \ldots c_{j,-1} \quad c_{j,0} \quad c_{j,1} \ldots c_{j,n}]^{\mathrm{T}}$, and A_{pq}'s correspond to $(2n+1) \times (2n+1)$ block matrices. Since there is a structural symmetry in this example, the coefficient matrix is symmetric with $A_{11} = A_{22}$ and $A_{12} = A_{21}$ as given below:

$$A_{11} = A_{22} = \begin{bmatrix} \ddots & \ddots & 0 & \cdots & & 0 \\ \ddots & 2-(\mu-\omega)^2 & \delta & & \ddots & \vdots \\ 0 & \delta & 2-\mu^2 & \ddots & & \vdots \\ \vdots & \ddots & & \ddots & 2-(\mu+\omega)^2 & \delta \\ 0 & \cdots & & 0 & \delta & \ddots \end{bmatrix}, \qquad (5.6)$$

$$A_{12} = A_{21} = \begin{bmatrix} -1 & -\delta/2 & 0 & \cdots & & 0 \\ -\delta/2 & -1 & -\delta/2 & \ddots & & \vdots \\ 0 & \ddots & \ddots & \ddots & & 0 \\ \vdots & \ddots & \ddots & \ddots & & -\delta/2 \\ 0 & \cdots & & 0 & -\delta/2 & -1 \end{bmatrix}. \qquad (5.7)$$

To have a nonzero $\mathbf{c}$ solution, the determinant of the coefficient matrix, $A(\mu)$, must be zero. This constitutes a characteristic equation for μ, in terms of the parameters δ and ω. The characteristic equation yields $2d(2n+1)$ roots for μ ($d = 2$ in this example), where n is the number of assumed harmonics. Yet, Floquet theory implies that there are effectively $2d$ principal roots, and the other ones are related to the principal roots via the relation $\mu_i = \mu_j \pm p\omega$, where p is an integer. Notice that these extra roots do not contribute to extra solutions, since the corresponding exponential part can be written as $e^{i\mu_j t}e^{ip\omega t}$ and the second part can be plugged into the periodic part.

By inserting μ_js into the coefficient matrix, solutions for $\mathbf{c}^{(j)} = [\mathbf{c}_1^{(j)} \quad \mathbf{c}_2^{(j)}]^{\mathrm{T}}$ can be found as the null space of $A(\mu_j)$. The relations $A_{11} = A_{22}$ and $A_{12} = A_{21}$ lead to the relation $\mathbf{c}_1^{(j)} = \mathbf{c}_2^{(j)}$. Furthermore, the principal roots come in pairs as $\mu_{j+1} = -\mu_j$, and this leads to the diagonal elements $A(\mu_{j+1})$ be the same as those of $A(\mu_j)$, but in reverse order. This relation results in a $\mathbf{c}^{(j+1)}$ having the same elements as $\mathbf{c}^{(j)}$, in the reversed order.

The roots of the characteristic equation give information about both the stability and the frequency content of the solution. If any one of the roots μ has a negative imaginary part, the exponential part, $e^{i\mu t}$ makes the solution grow unstable, whereas if all roots have

a non-negative imaginary part, the solution is bounded. More specifically, if the roots are real, the solution is either periodic or quasi-periodic. The stability transition curves for the 2DOF mass-spring chain are plotted by evaluating the imaginary parts of the characteristic roots, as given in Figure 5.2.

The frequency content can be determined by combining the frequencies of the exponential part and the periodic part, as $|Re(\mu) \pm l\omega|$. For this 2 DOF system, there are four distinct μ's as $\mu_2 = -\mu_1$ and $\mu_4 = -\mu_3$. In the frequency content of the response, half of the frequencies are determined by the first pair, and the other half are determined by the other pair. In this case, symmetric initial conditions (i.e. $x_1(0) = x_2(0)$, $\dot{x}_1(0) = \dot{x}_2(0)$) excite the frequencies associated with μ_1 and μ_2, whereas anti-symmetric initial conditions (i.e. $x_1(0) = -x_2(0)$, $\dot{x}_1(0) = -\dot{x}_2(0)$) excite those associated with μ_3 and μ_4. These two responses can be used to represent the response in terms of "modal components", such as $\mathbf{x}(t) = a_1 \mathbf{x}^{(1)}(t) + a_2 \mathbf{x}^{(2)}(t)$, where a_1 and a_2 are to be determined from the initial conditions.

As an example, for $\omega = 2.3$ and $\delta = 0.4$, from a computation with $n = 2$, the characteristic roots are approximated as $\mu_1 = -\mu_2 = 0.599$ and $\mu_3 = -\mu_4 = 1.035$. The symmetric initial conditions excite the frequencies $|1.035 \pm 2.3l|$, whereas the anti-symmetric initial conditions excite the frequencies $|0.599 \pm 2.3l|$, for $l = -2, -1, 0, 1, 2$, as shown in the FFT plots of m_1 in Figure 5.3. Arbitrary initial conditions produce responses with all of the frequencies contributing to the fast Fourier transforms plotted in Figure 5.3. The eigenvectors are $\mathbf{c}^{(1)} = [0.03179 \quad 0.68947 \quad -0.1527 \quad -0.01701 \quad -0.000425]^{\mathrm{T}}$ and $\mathbf{c}^{(3)} = [0.003834 \quad 0.22452 \quad 0.67037 \quad 0.013249 \quad 0.000086]^{\mathrm{T}}$. Since the 5th elements in both vectors are small, the 5th frequencies ($\mu_j + 2\omega$) are not visible in the FFT plots. More generally, five frequencies would show up from an $n = 2$ approximation.

The 2DOF spring-mass chain was analyzed with $n = 2$ harmonics, for different sets of parameters and initial conditions. The results were compared to those obtained from a numerical study, and the response and FFT plots are given in Figures 5.4 and 5.5 for an example.
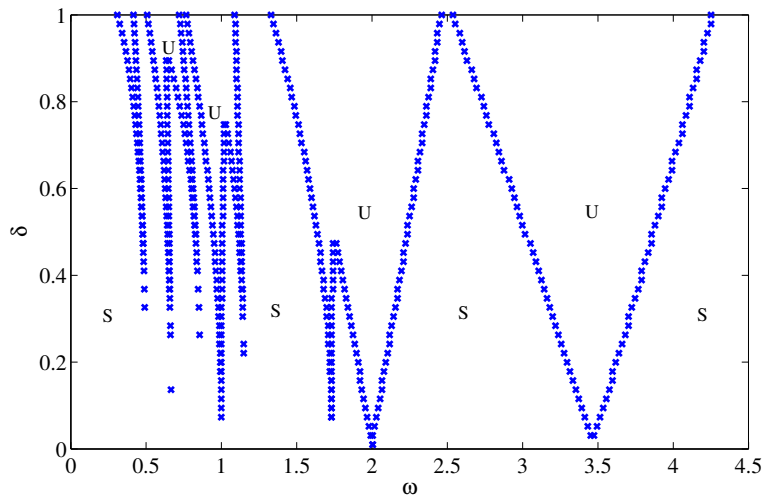
Figure 5.2 Stability regions for the 2 DOF mass spring chain.
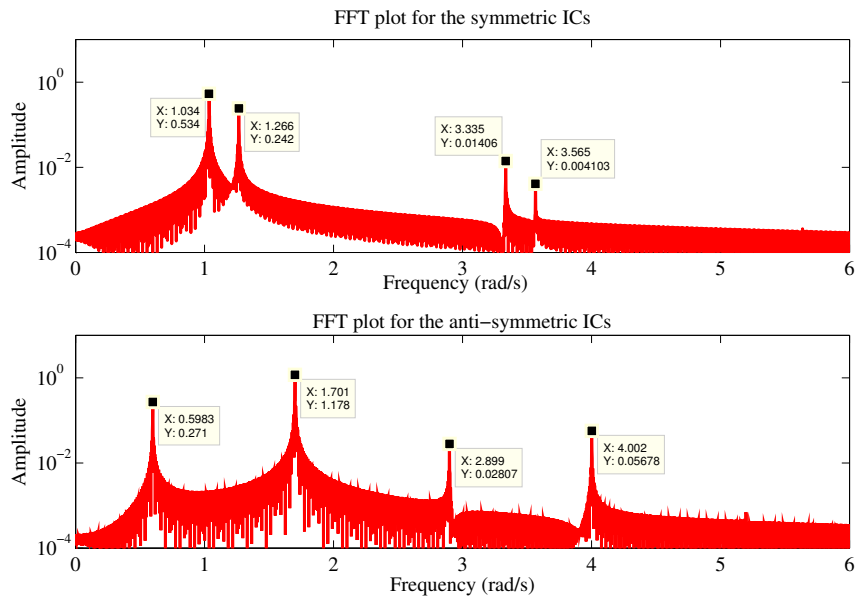
Figure 5.3 Modes excited by the symmetric and the anti-symmetric initial conditions, for $\omega = 2.3$ and $\delta = 0.4$. Amplitude FFT plots of displacements of m_1, generated with $n = 2$ truncated solution.

5.2.2 Three-Degree-of-Freedom Example

Another MDOF system with parametric stiffness is given in Figure 5.6. Two masses are connected to a main mass through parametric springs, which are driven out of phase, and the main mass is grounded with a regular spring. This system is analogous to a horizontal-
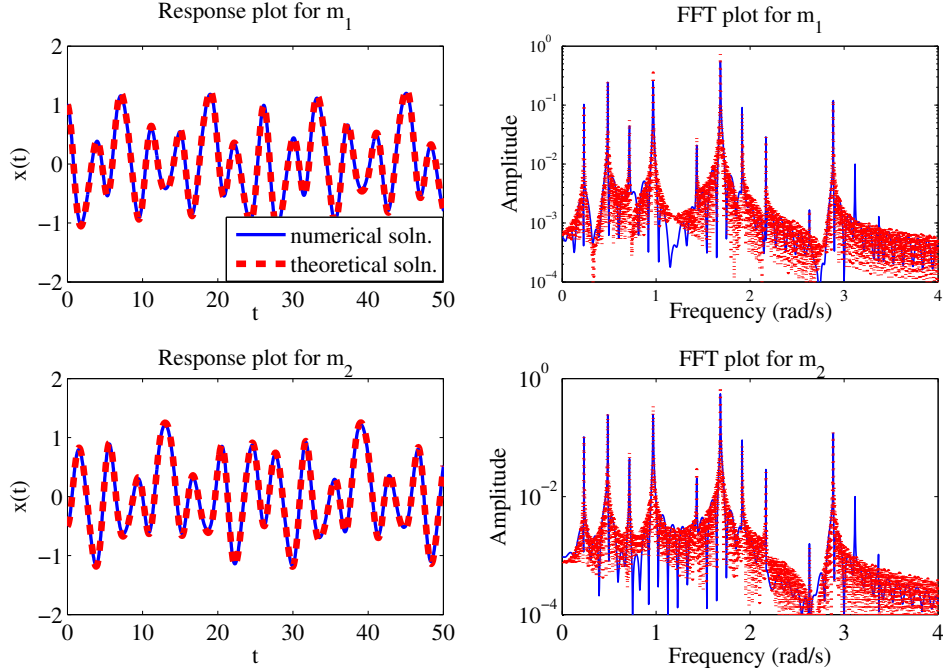
Figure 5.4 Response and amplitude FFT plots for $n = 2$, $\omega = 1.2$, $\delta = 0.6$, $\mathbf{x}(0) = [1 \quad -0.5]^T$ and $\dot{\mathbf{x}}(0) = [0 \quad 0]^T$.

axis turbine with two blades under a constant rotation rate, where the main mass represents the hub, and the other masses represent the blades.

For a normalized system, the parameters are assumed as $m_1 = m_2 = 1$, $M = \beta m_1$, $K = \gamma$, $k_1 = 1 - \delta \cos \omega t$ and $k_2 = 1 + \delta \cos \omega t$. Equations of motion representing this system are

$$\ddot{x}_1 + (1 - \delta \cos \omega t)(x_1 - x_3) = 0$$

$$\ddot{x}_2 + (1 + \delta \cos \omega t)(x_2 - x_3) = 0 \tag{5.8}$$

$$\beta \ddot{x}_3 - (1 - \delta \cos \omega t)x_1 - (1 + \delta \cos \omega t)x_2 + (2 + \gamma)x_3 = 0.$$

Plugging the approximate solution given in Equation (5.2) into the equations (5.8), and applying the steps explained in the previous section, characteristic exponents and the corresponding eigenvectors are found. By examining the imaginary parts of the characteristic exponents, the stability regions of the 3DOF system are plotted for $\gamma = 1$, $\beta = 1$ in Figure 5.7.
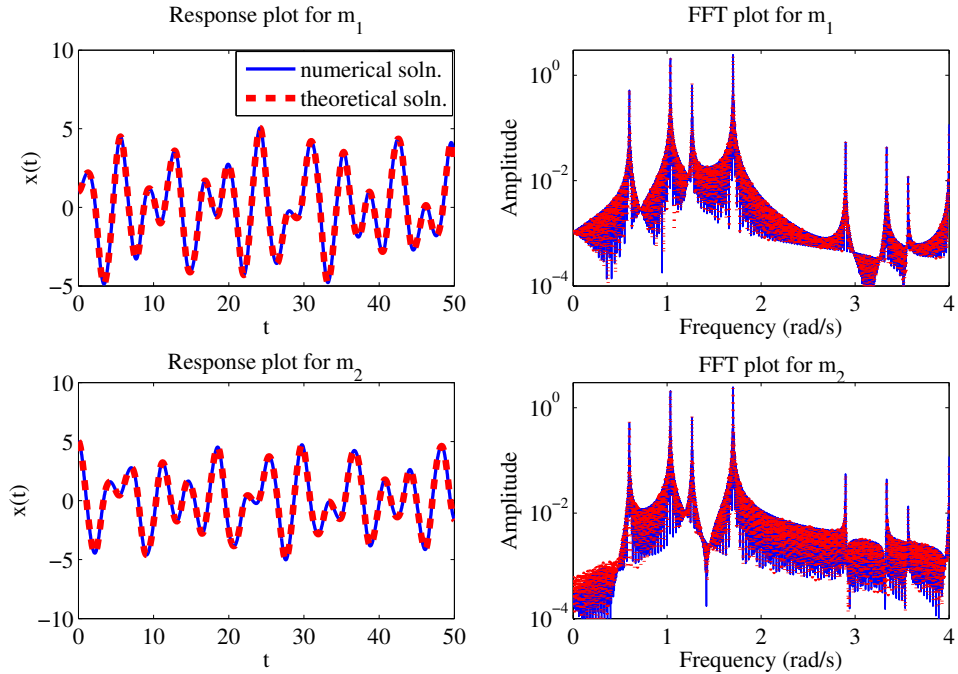
Figure 5.5 Response and FFT plots for $n = 2$, $\omega = 2.3$, $\delta = 0.4$, $\mathbf{x}(0) = \begin{bmatrix} 1 & 5 \end{bmatrix}^T$ and $\dot{\mathbf{x}}(0) = \begin{bmatrix} 0 & 0 \end{bmatrix}^T$.
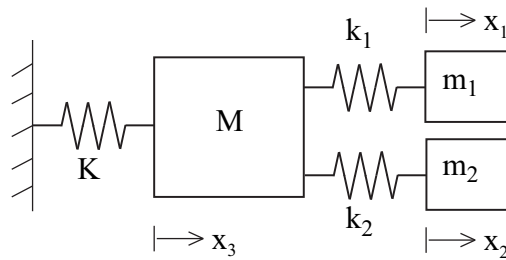
Figure 5.6 A 3 DOF mass-spring system.

In order to find the "modal solutions", as done in the previous section, the following procedure is applied.

There are six principal characteristic roots and so the general solution can be written as

$$\mathbf{x}(t) = \sum_{j=1}^{6} a_j \mathbf{x}_j(t), \tag{5.9}$$

where

$$\mathbf{x}_j(t) = \sum_{l=-n}^{n} \mathbf{c}_{j,l} e^{il\omega t}. \tag{5.10}$$
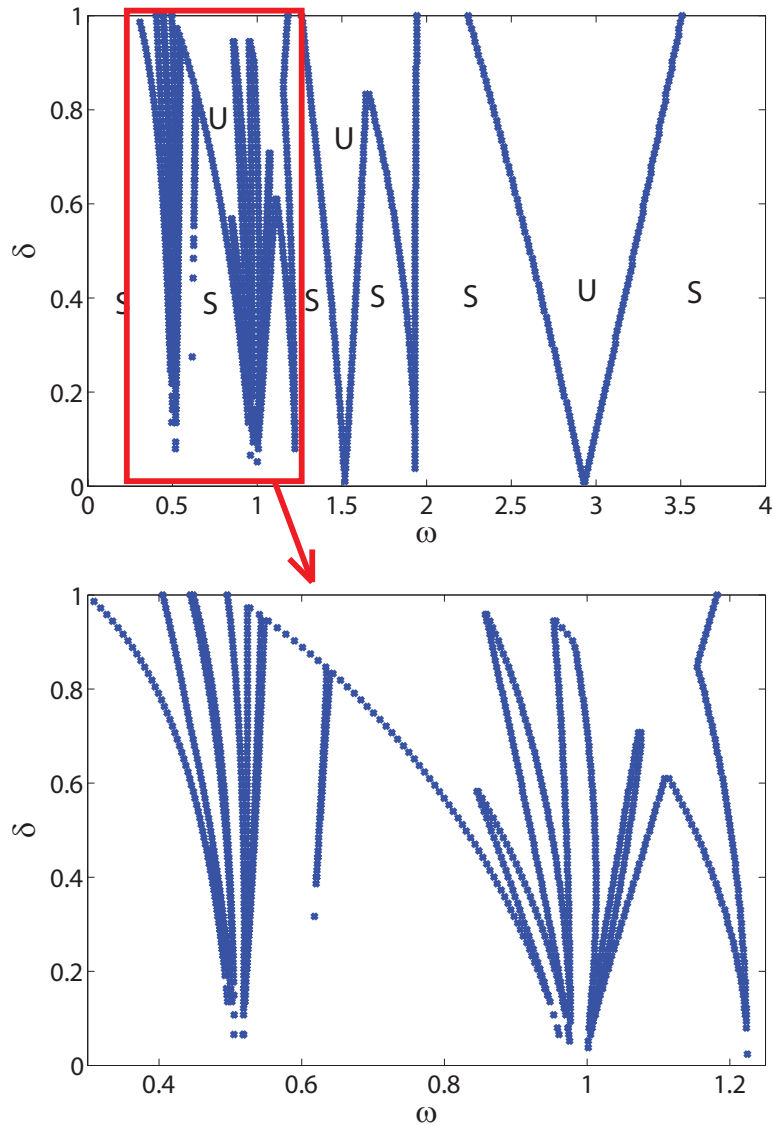
Figure 5.7 Stability regions for the 3 DOF mass spring system, for $\beta = 1$ and $\gamma = 1$.

Arbitrary initial conditions can be expressed as a set of linear equations in terms of the constants a_j, as

$$\begin{bmatrix} \mathbf{x}_0 \\ \dot{\mathbf{x}}_0 \end{bmatrix} = \begin{bmatrix} \mathbf{x}_1(0) & \dots & \mathbf{x}_6(0) \\ \dot{\mathbf{x}}_1(0) & \dots & \dot{\mathbf{x}}_6(0) \end{bmatrix} \begin{bmatrix} a_1 \\ \vdots \\ a_6 \end{bmatrix}. \tag{5.11}$$

Notice that the initial condition $\begin{bmatrix} \mathbf{x}_0^T & \dot{\mathbf{x}}_0^T \end{bmatrix}^T = \begin{bmatrix} \mathbf{x}_j(0)^T & \dot{\mathbf{x}}_j(0)^T \end{bmatrix}^T$ results in $a_j = 1$ and $a_{l \neq j} = 0$. Therefore a scalar multiple of each column can be used as an initial condi-

tion to find the separate modal functions. For example for $\beta = 1$, $\gamma = 1$, $\delta = 0.5$ and $\omega = 2.2$, the characteristic exponents are $\mu = \pm 0.975, \pm 0.520, \pm 0.315$. The initial condition vector $\mathbf{x}_1(0) = \begin{bmatrix} -1.388 & 1.364 & 0.263 & 0 & 0 & 0 \end{bmatrix}$ excites the frequencies $|0.975 \pm 2.2l|$, $\mathbf{x}_2(0) = \begin{bmatrix} 1.195 & 1.311 & 0.926 & 0 & 0 & 0 \end{bmatrix}$ excites the frequencies $|0.520 \pm 2.2l|$, and $\mathbf{x}_3(0) = \begin{bmatrix} -1.072 & -0.001 & 1.513 & 0 & 0 & 0 \end{bmatrix}$ excites the frequencies $|0.315 \pm 2.2l|$, as shown in Figure 5.8. By writing an initial condition as a linear combination of $\begin{bmatrix} \mathbf{x}_j(0)^T & \dot{\mathbf{x}}_j(0)^T \end{bmatrix}^T$'s, the response can be found as the same linear combination of the corresponding modal functions.
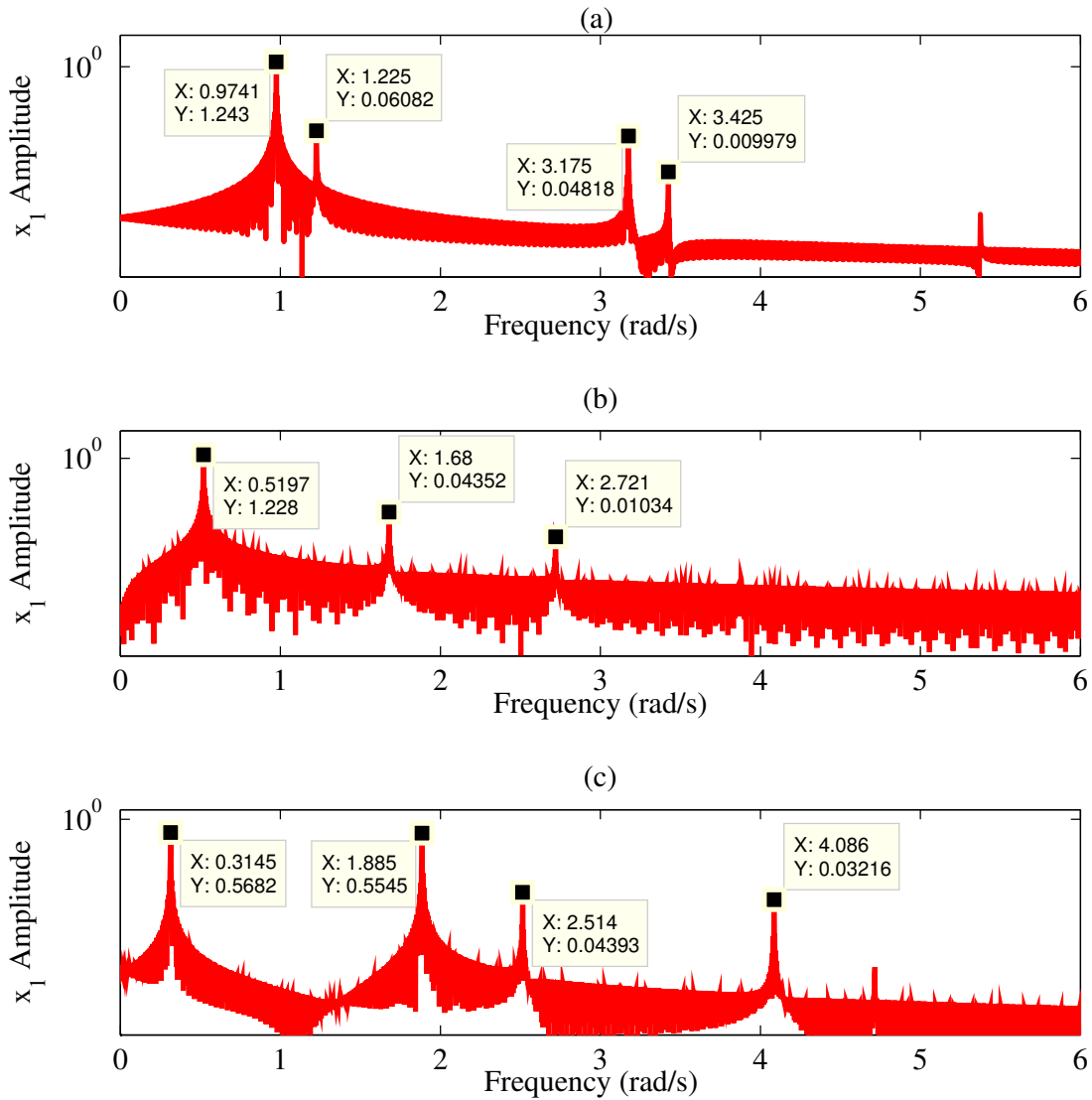
Figure 5.8 Modes excited by the initial conditions which resonate the frequencies that are associated with (a) $\mu_1 = 0.975$, (b) $\mu_2 = 0.520$, (c) $\mu_3 = 0.315$.

The initial condition responses and amplitude FFT plots were obtained assuming $n = 2$ harmonics, for various parameter sets, and were compared to those obtained from a numerical study, as shown in Figures 5.9 and 5.10.
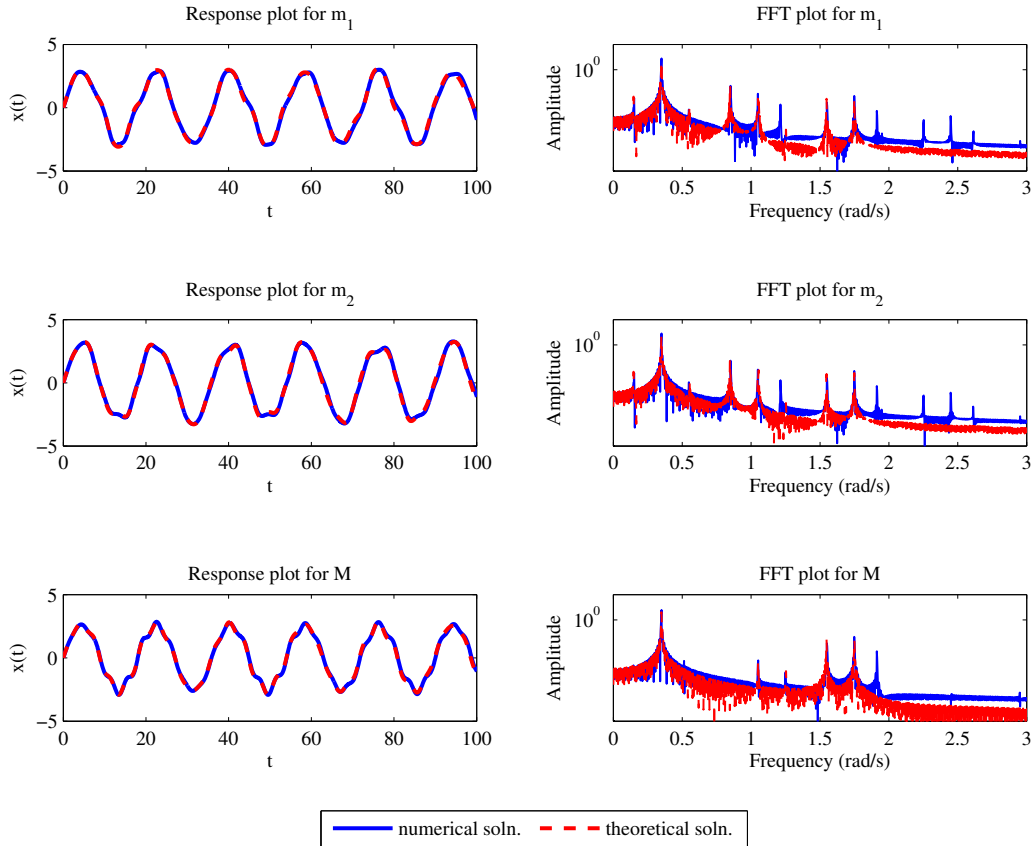
Figure 5.9 Response and FFT plots for $n = 2$, $\omega = 0.7$, $\delta = 0.5$, $\gamma = 0.4$, $\mathbf{x}(0) = \begin{bmatrix} 0 & 0 & 0 \end{bmatrix}^T$ and $\dot{\mathbf{x}}(0) = \begin{bmatrix} 1 & 1 & 1 \end{bmatrix}^T$.

5.3 Discussion

In the MDOF examples we presented, close examination of the stability wedges suggests that they may be based at $\omega = (\omega_i + \omega_j)/N$, where N is a positive integer.

For the two-DOF case, with $\omega_1 = 1$ and $\omega_2 = \sqrt{3} = 1.73$, we see the major wedges at $2\omega_1 = 2$ and $2\omega_2 = 3.46$, representing the subharmonic instability of each "mode". The
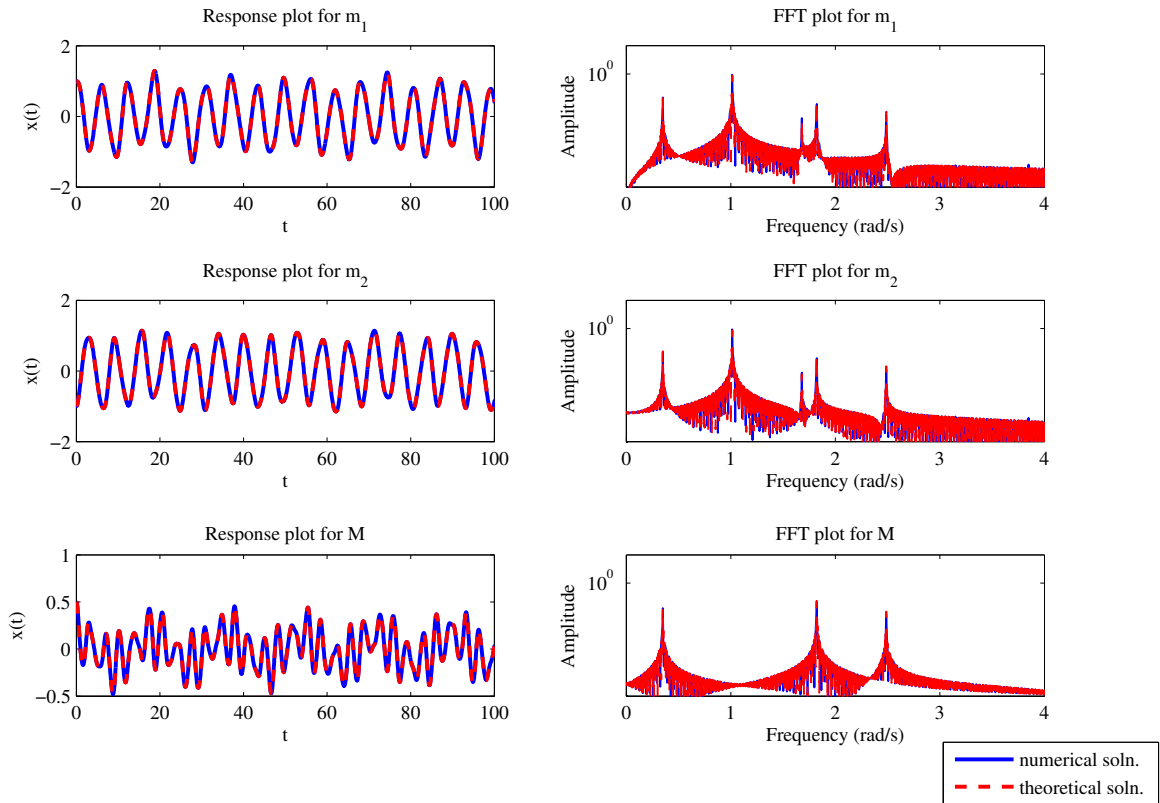
Figure 5.10 Response and FFT plots for $n = 2$, $\omega = 3.5$, $\delta = 0.3$, $\gamma = 0.4$, $\mathbf{x}(0) = [1 \quad -1 \quad 0.5]^T$ and $\dot{\mathbf{x}}(0) = [0 \quad 0 \quad 0]^T$.

symmetry in the two-DOF model drives the resonances such that $\omega_i = \omega_j$ (i.e. $i = j$) in the suggested instability condition. We also see the other slender instability wedges for mode one at $\omega = \omega_1$, $\omega = 2/3$, and even $\omega = 1/2$, and likewise for mode two at $\omega = \omega_2$, $\omega = 2\omega_2/3 \approx 1.15$, and $\omega = \omega_2/2 \approx 0.87$.

In the three-DOF system, for $\beta = 1$ and $\gamma = 1$, the modal frequencies are $\omega_1 = 0.518$, $\omega_2 = 1$, $\omega_3 = 1.932$. We see two major subharmonic instability wedges originating at frequencies $\omega \approx \omega_2 + \omega_3 = 2.93$ and $\omega \approx \omega_2 + \omega_1 = 1.52$. Some of the superharmonic wedges are also based at frequencies that match the pattern, such as $\omega_3 = 1.93$, $(\omega_1 + \omega_3)/2 = 1.22$, $\omega_1 = 1$, $(\omega_2 + \omega_3)/3 = 0.98$, $\omega_3/2 = 0.97$, $(\omega_1 + \omega_3)/2 = 1.22$, $\omega_1 = 0.52$, and $(\omega_1 + \omega_2)/3 = 0.51$.

Simulations were done at various parameter values to check consistency. In the 3-DOF

example, at $\delta = 0.3$ and $\omega = 3.1$, the simulation was unstable, while at $\omega = 3.2$, the simulation was stable, consistent with the stability wedge in Figure 5.7.

Based on the Floquet solution as a linear combination of terms of the form $e^{i\mu t}\mathbf{p}(t)$, where $\mathbf{p}(t)$ is a periodic function, it is clear that initial conditions can be specified such that only one of these terms is active. In this sense, we can call them "modal responses". Each of these modes has its own frequency content, but the $\mathbf{p}(t)$ are not synchronous, and not described using simple shape vectors like traditional modes. We have demonstrated such independent oscillation solutions in the two examples given here. We might consider whether a coordinate transformation exists such that a given modal response can be isolated as a single degree of freedom, and then whether each modal degree of freedom is parametrically excited and follows the stability pattern of a Hill's equation (or more generally an Ince equation, which has a periodic coordinate transformation between it and a Hill's equation [52]). Complicating these speculations is the entanglement of the reference modal frequencies (those from the $\delta = 0$ system) in the excited system's stability wedge patterns.

The analysis presented here involves the solution to a nonstandard eigenvalue problem in the form of Equation (5.5), in which matrix $\mathbf{A}$ includes elements with quadratic μ terms. The resulting characteristic equation is a polynomial of degree $2d(2n+1)$ in μ. There may be computational limits on finding symbolic solutions for the μ as the degree of freedom, d, or the number of harmonics, n, increases, although $n = 2$ harmonics was able to predict the response for the systems analyzed above.

5.4   Conclusion

In this work, a procedure for finding an approximate solution to a MDOF system with parametric stiffness has been represented. A Floquet-type solution composed of an exponential and a periodic part was assumed, and applying harmonic balance to the system equations, an eigenvalue problem resulted, with eigenvalues that provide the Floquet characteristic

exponents and the eigenvectors that provide the Fourier coefficients.

The initial-conditions response was expressed in terms of independent modal components, which were demonstrated by separating the initial conditions exciting the modes associated with separate characteristic exponents. The stability transition curves were obtained by examining the imaginary parts of the characteristic exponents. The response and FFT plots were generated for various parameters and initial conditions, and compared to numerical results for validation.

The method used in this study was applied to determine the initial condition response as well as the stability of the system, whereas the commonly applied analyses seen in previous studies reflect interest only in the latter. The procedure is to be applied to three-blade wind turbine models to find the response characteristics.

CHAPTER 6

CONCLUSIONS AND FUTURE WORK

6.1 Concluding Remarks

This thesis aimed to study some aspects of the dynamics of wind turbines, and fundamental dynamic systems relevant to wind turbine dynamics. An analysis of a horizontal-axis wind-turbine blade under bend-bend-twist vibrations, and in plane coupled blade-hub vibrations of a three-blade turbine were studied. Inspired by the periodically varying stiffness terms in blade equations, solutions to the Mathieu equation, and MDOF systems with parametric stiffness were investigated.

Modeling the blade as a straight beam with a varying cross-section and pretwist, the energy expressions were found in terms of bending and torsional displacements. The energies were expressed in terms of familiar beam parameters. Then assuming uniform cantilever beam modes as shape functions for each displacement, the energy formulations were written in terms of the assumed modal coordinates. The bend-bend-twist coupled equations of motion were found via Lagrange's method. The rotor speed was assumed to be constant for this analysis, so it was not taken as one of the modal coordinates. Natural frequencies and mode shapes were found for existing blade models by applying a modal analysis. The first two mode shapes are dominantly in-plane and out-of-plane bending modes. Blade stiffness varies with rotor angle due to parametric effects of the gravity. To show the stiffness changes, blades were analyzed at horizontal and vertical orientations. Parametric stiffness terms were found to be more significant for longer blades, and they are important since they can introduce secondary resonances to the system.

Equations of motion for a three-blade turbine and hub were found by applying Lagrange's method to the system's total energies. For this analysis, only in-plane vibrations were taken

into account, and the variation in hub speed was included as a variable. Assuming one mode for each blade, the rotor and blade equations were derived. Then the time domain equations were transformed into rotor angle-based equations. Variations in the rotor speed were assumed to be small, and applying a nondimensionalization and a scaling scheme, the rotor equation was decoupled from the leading-order blade equations. Interdependent blade equations were analyzed with a first-order method of multiple scales. Parametric and direct excitations introduced a superharmonic and a subharmonic resonance to the system. The superharmonic resonance occurs near $2\Omega = \omega_{n2}$, where Ω is the rotor speed, and ω_{n2} is the blade stiffness. For a cyclicly symmetric turbine (i.e. all three blades have the same inertia and stiffness), the blades have a unison amplitude response with a phase difference. The subharmonic resonance occurs near $\Omega = 2\omega_{n2}$, with zero amplitude blade response. The stability of the blade response for subharmonic resonance was investigated.

The Mathieu equation is similar to a SDOF model of blade equations, and it represents many other mechanical systems as well. Approximate general solutions to the undamped, damped and two-harmonic-excitation Mathieu equations were studied. A truncated Floquet-type solution was assumed, and inserted into the equations. Then, applying harmonic balance, the characteristic exponents and the Fourier coefficients were approximated. The general responses and stability of the solution can be found for any parameter values. The initial condition responses were found for a set of parameter values, and they agreed well with the simulations done via the ODE solver on MATLAB. For the damped Mathieu equation, the decay rate of the response was also quantified through the characteristic exponents. In general, this approximate solution is applicable to SDOF systems with parametric excitation.

To show that the method used in Chapter 4 is also applicable to MDOF systems, example 2DOF and 3DOF systems with parametric stiffness were studied. A MDOF Floquet-type solution was applied to find the general responses and the stability characteristics. The 3DOF system showed stability characteristics different than expected. The instability regions are based at $(\omega_j + \omega_k)/N$ ($j = 1 \ldots d$ and $k = 1 \ldots d$, where d is the degree of freedom) points,

whereas for the SDOF Mathieu equation they are based at $2\omega_j/N$.

Aeroelastic modeling was reviewed as an appendix to this work. Aerodynamic forces depend on the blade angle, blade velocity, and blade motion histories. Thus the aeroelastic model will affect the predicted vibration responses and stabilities. As such it is important to study aeroelastic models for wind-turbine blade vibration analysis. When operating at high angles of attack, turbine blades might experience stall, where at a critical angle the lift force drops suddenly. Furthermore rapid variations in the angle of attack can introduce dynamic stall where the lift force has a hysteresis. Semi-empirical models of the lift force in dynamic stall were studied. These models use differential equations to express the dynamics of the lift force. Coefficients of these equations and their dependence on state variables were explained for two different models (ONERA's [2] and that of Larsen *et al.* [4]) existing in the literature.

In summary, this thesis provided a modal analysis of a single blade and a perturbation analysis of a three-blade turbine. An extensive review on two aerodynamic stall models was given. Also to investigate the transient dynamics, an analysis of the Mathieu equation and MDOF systems with parametric stiffness were studied.

6.2 Future Work

The work done in this thesis can be extended to the following:

- The results found through the modal analysis using a bend-bend-twist beam model can be verified by experiments. A simple beam can be analyzed at various orientations to show the parametric effects. Also it can be spun at a constant speed to investigate the secondary resonances, analyzed in the literature for single beams, and for coupled beam-rotor systems, as modeled in Chapter 3.

- The three-blade model used in Chapter 3 has a cyclic symmetry which results in symmetric blade responses. To understand the effects of broken symmetry, which is

likely to be seen in real systems with imperfections, the analysis can be extended to a model where one or two of the blades are mistuned. Also the analysis for in-plane three-blade dynamics can be extended to bend-bend-twist analysis of three-blade turbines. The tower motion and rotor stiffness can be taken into account.

- One of the aerodynamic stall models can be applied to an existing blade to find the effect on the forced response, and on possible generation of limit cycle oscillations.

- The Floquet-type solution assumed in Chapter 4 can be extended to other parametrically excited systems, to find their initial condition responses, and stability. For example vertical axis wind turbine blades may show periodic damping characteristics [89], and the Floquet-type solution can be assumed to model their transient dynamics.

- The analysis on MDOF systems with parametric stiffness can be applied to three-blade turbine equations, to examine whether there may exist parametric instabilities in the transient dynamics of coupled blade-hub turbine models, and to model stable transient responses and predict the frequency content.

APPENDICES

APPENDIX A

EQUATIONS OF MOTION OF A BLADE

A.1 Strains

The Lagrangian strain tensor of an inextensible straight beam under bend-bend-twist vibrations is determined using Green's formula [66]. Strains are expressed in terms of displacements as

$$\varepsilon_{xx} = -\eta v'' - \zeta w'' + \frac{(\eta v'' + \zeta w'')^2}{2} + \frac{(\eta^2 + \zeta^2)\theta_x'^2}{2} + (\eta w' - \zeta v')\theta_x' + \mathcal{O}(\epsilon^3), \qquad \text{(A.1)}$$

$$\varepsilon_{\eta\eta} = \frac{v'^2}{2} + \frac{\theta_x^2}{2} + \mathcal{O}(\epsilon^3), \qquad \text{(A.2)}$$

$$\varepsilon_{\zeta\zeta} = \frac{w'^2}{2} + \frac{\theta_x^2}{2} + \mathcal{O}(\epsilon^3), \qquad \text{(A.3)}$$

$$\gamma_{x\eta} = -\zeta\theta_x' + v'(v''\eta + w''\zeta) + \theta_x(w' + \theta_x'\eta) + \mathcal{O}(\epsilon^3), \qquad \text{(A.4)}$$

$$\gamma_{x\zeta} = \eta\theta_x' + w'(v''\eta + w''\zeta) + \theta_x(-v' + \theta_x'\zeta) + \mathcal{O}(\epsilon^3), \qquad \text{(A.5)}$$

$$\gamma_{\eta\zeta} = v'w' + \mathcal{O}(\epsilon^3). \qquad \text{(A.6)}$$

A.2 Kinetic and Potential Energies

For a linear straight inextensible nonuniform with bend-bend-twist deformations, rotating about an axis through the attachment point, perpendicular to both the gravity vector and the centroidal axis $\hat{x}$, the energy expressions arising from Equations (2.3) through (2.5), after incorporating Equations (A.1) - (A.6) and the Equations for $\mathbf{r}_{P1}$ and $\mathbf{v}_{P1}$ from Section 2.2.1, written in terms of deflections of the centroid are

$$U = \frac{1}{2}\int_0^L \left[I_{\eta\eta}(x)(Ew''^2 + G\theta_x'^2) + I_{\zeta\zeta}(x)(Ev''^2 + G\theta_x'^2) + 2EI_{\eta\zeta}(x)v''w'' \right] dx, \qquad \text{(A.7)}$$

$$T = \frac{1}{2} \int_0^L \left[J_{\zeta\zeta}(x)(\dot{\theta}_x{}^2 + (\dot{\phi} + \dot{v}')^2 + \dot{\phi}^2 v'^2) + J_{\eta\eta}(x)\left((\dot{\theta}_x + \dot{\phi}w')^2 + (\theta_x\dot{\phi} - \dot{w}')^2\right) \right.$$

$$-2J_{\eta\zeta}(x)\left(\dot{\phi}^2\theta_x - \dot{\phi}\dot{\theta}_x v' - \dot{\phi}^2 v'w' + \dot{\phi}\theta_x\dot{v}' - \dot{\phi}\dot{w}' - \dot{v}'\dot{w}'\right)$$

$$\left. +m(x)\left(\dot{\phi}^2 v^2 + (\dot{\phi}(x+u) + \dot{v})^2 + \dot{w}^2\right)\right] dx, \quad \text{(A.8)}$$

$$V_g = \int_0^L -m(x)g\left[(x+u)\cos\phi - v\sin\phi\right]dx, \quad \text{(A.9)}$$

where I_{ij} are second moments of area, J_{ij} are moments of inertia, $A(x)$ is cross-sectional area, $m(x)$ is mass per unit length, E is elastic modulus and G is shear modulus.

When written in terms of shear center deflections, the energy expressions are as follows:

$$U_s = \frac{1}{2} \int_0^L \left[I_{\eta\eta s}(x)(Ew_s''^2 + G\theta_x'^2) + I_{\zeta\zeta s}(x)(Ev_s''^2 + G\theta_x'^2) + 2EI_{\eta\zeta s}(x)v_s''w_s'' \right] dx, \quad \text{(A.10)}$$

$$T_s = \frac{1}{2} \int_0^L \left[J_{\zeta\zeta s}(x)(\dot{\theta}_x{}^2 + (\dot{\phi} + \dot{v}_s')^2 + \dot{\phi}^2 v_s'^2) + J_{\eta\eta s}(x)\left((\dot{\theta}_x + \dot{\phi}w_s')^2 + (\theta_x\dot{\phi} - \dot{w}_s')^2\right) \right.$$

$$-2J_{\eta\zeta s}(x)\left(\dot{\phi}^2\theta_x - \dot{\phi}\dot{\theta}_x v_s' - \dot{\phi}^2 v_s'w_s' + \dot{\phi}\theta_x\dot{v}' - \dot{\phi}\dot{w}_s' - \dot{v}_s'\dot{w}_s'\right) + m(x)\left(\dot{\phi}^2 v_s^2 \right.$$

$$+(\dot{\phi}(x+u_s) + \dot{v}_s)^2 + \dot{w}_s{}^2 + \eta_s(x)(\dot{w}_s\dot{\theta}_x - x\dot{\phi}^2 v_s' - \Omega v_s'\dot{v}_s - \Omega\dot{u}_s + \Omega^2 v_s + \Omega v_s\dot{v}_s')$$

$$\left. \left. +\zeta_s(x)(-x\Omega\dot{\theta}_x - \dot{v}_s\dot{\theta}_x - x\Omega^2 w_s' - \Omega\dot{v}_s w_s' - \Omega^2\theta_x v_s + \Omega v_s\dot{w}_s')\right)\right] dx, \quad \text{(A.11)}$$

$$V_{gs} = \int_0^L -m(x)g\left[(x+u_s)\cos\phi - v_s\sin\phi + \eta_s(x)(v_s'\cos\phi + \sin\phi)\right.$$

$$\left. +\zeta_s(x)(w_s'\cos\phi - \theta_x\sin\phi)\right] dx, \quad \text{(A.12)}$$

where I_{ijs} and J_{ijs} are second moments of area and moments of inertia about the shear center, and u_s, v_s and w_s are displacements of the shear center.

A.3 Equations of Motion

For the case of a single assumed mode for each deformation coordinate, the equations of motion for the deflections centered at the centroid are

$$
\ddot{q}_{v1} \int_0^L \left(m(x)\gamma_{v1}^2(x) + J_{\zeta\zeta}(x)\gamma_{v1}'^2(x) \right) dx + \ddot{q}_{w1} \int_0^L J_{\eta\zeta}(x)\gamma_{v1}'(x)\gamma_{w1}'(x)dx
$$

$$
+ q_{v1} \int_0^L \left[EI_{\zeta\zeta}(x)\gamma_{v1}''^2(x) + \dot{\phi}^2 \left(xm(x) \int_0^x \gamma_{v1}'^2(\xi)d\xi - J_{\zeta\zeta}(x)\gamma_{v1}'^2(x) - m(x)\gamma_{v1}^2(x) \right) \right.
$$

$$
\left. + m(x)g\cos\phi \int_0^x \gamma_{v1}(\xi)'^2 d\xi \right] dx + q_{w1} \int_0^L \left(EI_{\eta\zeta}\gamma_{v1}''(x)\gamma_{w1}''(x) - \dot{\phi}^2 J_{\eta\zeta}\gamma_{v1}'(x)\gamma_{w1}'(x) \right) dx
$$

$$
- 2\dot{q}_{\theta1} \int_0^L \dot{\phi}J_{\eta\zeta}\gamma_{v1}'\gamma_{\theta1}dx + \int_0^L gm(x)\sin\phi\gamma_{v1}(x)dx = Q_{v1}, \quad \text{(A.13)}
$$

$$
\ddot{q}_{w1} \int_0^L \left(m(x)\gamma_{w1}^2(x) + J_{\eta\eta}(x)\gamma_{w1}'^2(x) \right) dx + \ddot{q}_{v1} \int_0^L J_{\eta\zeta}(x)\gamma_{v1}'(x)\gamma_{w1}'(x)dx
$$

$$
+ q_{w1} \int_0^L \left[EI_{\eta\eta}(x)\gamma_{w1}''^2(x) + \dot{\phi}^2 \left(xm(x) \int_0^x \gamma_{w1}'^2(\xi)d\xi - J_{\eta\eta}(x)\gamma_{w1}'^2(x) \right) \right.
$$

$$
\left. + m(x)g\cos\phi \int_0^x \gamma_{w1}(\xi)'^2 d\xi \right] dx + q_{v1} \int_0^L \left(EI_{\eta\zeta}\gamma_{v1}''(x)\gamma_{w1}''(x) - \dot{\phi}^2 J_{\eta\zeta}\gamma_{v1}'(x)\gamma_{w1}'(x) \right) dx
$$

$$
- 2\dot{q}_{\theta1} \int_0^L \dot{\phi}J_{\eta\eta}\gamma_{w1}'\gamma_{\theta1}dx = Q_{w1}, \quad \text{(A.14)}
$$

$$
\ddot{q}_{\theta1} \int_0^L (J_{\eta\eta}(x) + J_{\zeta\zeta}(x))\gamma_{\theta1}^2(x)dx + q_{\theta1} \int_0^L \left[G(I_{\eta\eta}(x) + I_{\zeta\zeta}(x))\gamma_{\theta1}'^2(x) - \dot{\phi}^2 J_{\eta\eta}(x)\gamma_{\theta1}^2(x) \right] dx
$$

$$
+ 2\dot{q}_v \int_0^l J_{\eta\zeta}\dot{\phi}\gamma_{v1}'\gamma_{\theta1}dx + 2\dot{q}_w \int_0^L J_{\eta\eta}\dot{\phi}\gamma_{w1}'\gamma_{\theta1}dx + \int_0^L \dot{\phi}^2 J_{\eta\zeta}\gamma_{\theta1}(x)dx = Q_{\theta1}. \quad \text{(A.15)}
$$

APPENDIX B

IN-PLANE THREE BLADE TURBINE EQUATIONS

B.1 In-Plane Energy Expressions

In this analysis only in-plane vibrations are taken into account. $v(x,t)$ is approximated with a single mode. For each blade it is assumed that $v_j(x,t) = \gamma_v(x)q_j(t)$, where $\gamma_v(x)$ is the first cantilever beam mode, and $q_j(t)$ is the assumed modal coordinate for the jth blade.

In-plane energy formulations for a single blade are given in terms of the assumed modal coordinates below.

$$T(q_j, \dot{q}_j, \dot{\phi}) = \frac{1}{2} \int_0^L \left[m(x) \left(\dot{\phi} \left(x + \frac{q_j^2}{2} \int_0^x \gamma_v'(\xi)^2 \, d\xi \right) + \dot{q}_j \gamma_v(x) \right)^2 \right.$$
$$\left. + m(x)(\dot{\phi} q_j \gamma_v(x))^2 + J_{\zeta\zeta}(x) \left((\dot{\phi} + \dot{q}_j \gamma_v'(x))^2 + (\dot{\phi} q_j \gamma_v'(x))^2 \right) \right] dx, \quad \text{(B.1)}$$

$$U(q_j) = \frac{1}{2} \int_0^L EI_{\zeta\zeta}(x) q_j^2 \gamma_v''(x)^2 \, dx, \quad \text{(B.2)}$$

$$V_g(q_j, \phi_j) = \int_0^L -m(x)g \left[\left(x + \frac{q_j^2}{2} \int_0^x \gamma_v'(\xi)^2 \, d\xi \right) \cos\phi_j - q_j \gamma_v(x) \sin\phi_j \right] dx. \quad \text{(B.3)}$$

B.2   Parameters used in the Equations of Motion

Expressions for the parameters in Equations (3.4) and (3.5) are given below:

$$m_b = \int_0^L \left(m(x)\gamma_v(x)^2 + J_{\zeta\zeta}(x)\gamma_v'(x)^2 \right) dx,$$

$$k_0 = \int_0^L \mathrm{EI}_{\zeta\zeta}(x)\gamma_v''(x)^2 \, dx,$$

$$k_1 = \int_0^L \left(xm(x)\int_0^x \gamma_v'(\xi)^2 \, d\xi - m(x)\gamma_v(x)^2 - J_{\zeta\zeta}(x)\gamma_v'(x)^2 \right) dx,$$

$$k_2 = \int_0^L gm(x) \left(\int_0^x \gamma_v'(\xi)^2 \, d\xi \right) dx,$$

$$d = \int_0^L gm(x)\gamma_v(x) \, dx,$$

$$e = \int_0^L \left(xm(x)\gamma_v(x) + J_{\zeta\zeta}(x)\gamma_v'(x) \right) dx,$$

$$J_r = J_{hub} + 3\int_0^L \left(x^2 m(x) + J_{\zeta\zeta}(x) \right) dx,$$

$$Q_j = \int_0^L f_j(x)\gamma_v(x) \, dx,$$

$$Q_\phi = \sum_{j=1}^3 \int_0^L x f_j(x) \, dx.$$

where x is the axis along the length of the undeformed blade, $m(x)$ is mass per unit length, $EI_{\zeta\zeta}$ and $J_{\zeta\zeta}$ are the in-plane bending stiffness and mass moment of inertia per length about the neutral axis, J_{hub} is the hub inertia, γ_v is the assumed modal function, which is the first uniform cantilever beam mode, and $f_j(x)$ accounts for the distributed aerodynamic loads on the jth blade. In these expressions, $(\ )' = d(\ )/dx$.

A simplified model is used where the flow is assumed to be steady, and the wind speed is assumed to be slightly increasing linearly with height h (i.e. $u_{wind} = u_0 + \epsilon h u_1 = u_0 - \epsilon x \cos\phi_j u_1$). Neglecting the contribution of state variations on the angle of attack, the lift force is proportional to $|\vec{u}_{rel}|^2$, where $\vec{u}_{rel} = \vec{u}_{wind} - \vec{u}_{blade}$ and $\vec{u}_{blade} = x\dot{\phi}\hat{y}_j$. $\vec{u}_{rel}$ and

$f_j(x)$ are found as

$$\vec{u}_{rel} = (u_0 - \epsilon x \cos \phi_j u_1)\hat{z} - x\dot{\phi}\hat{y}_j,$$

$$f_j(x) = c_p \left[(u_0 - \epsilon x \cos \phi_j u_1)^2 + (x\dot{\phi})^2 \right],$$

where c_p is a constant which is composed of the air density, lift coefficient, and other geometric parameters, $\hat{x}_j$ and $\hat{y}_j$ are the axial and the in-plane bending directions of the jth blade, and z is the out-of plane direction, as shown in Figure 3.1. Plugging $f_j(x)$ into the Q_j and Q_ϕ expressions, we obtain

$$Q_j = \int_0^L c_p \left(u_0^2 - 2\epsilon u_0 u_1 x \cos \phi_j + \dot{\phi}^2 x^2 + O(\epsilon^2) \right) \gamma_v(x)\, dx,$$

$$Q_\phi = \sum_{j=1}^{3} c_p \left(u_0^2 \frac{L^2}{2} + \dot{\phi}^2 \frac{L^4}{4} - 2\epsilon u_0 u_1 \cos \phi_j \frac{L^3}{3} + O(\epsilon^2) \right).$$

Note that $\sum_{j=1}^{3} \cos \phi_j = 0$, therefore Q_ϕ can be written as $Q_\phi = \hat{Q}_{\phi 0} + \hat{Q}_{\phi 1}\dot{\phi}^2$. For small ϵ, one can assume that Q_j has the form $Q_j = \hat{Q}_{j0} + \epsilon \hat{Q}_{j1} \cos \phi_j + \hat{Q}_{j2}\dot{\phi}^2$. Plugging $\dot{\phi} = \Omega \nu = \Omega(1 + \epsilon^2 \nu_1)$, we obtain $Q_\phi = \hat{Q}_{\phi 0} + \hat{Q}_{\phi 1}\Omega^2 + O(\epsilon^2)$ and $Q_j = \hat{Q}_{j0} + \hat{Q}_{j2}\Omega^2 + \epsilon \hat{Q}_{j1} \cos \phi_j + O(\epsilon^2)$. Since Ω is constant, one can simply write $Q_\phi = Q_{\phi 0} + O(\epsilon^2)$ and $Q_j = Q_{j0} + \epsilon Q_{j1} \cos \phi_j + O(\epsilon^2)$.

B.3   An Alternative Scaling Scheme

An alternative scaling scheme is investigated where

$$\nu = 1 + \epsilon \nu_1, \quad \tilde{c}_b = \epsilon \hat{c}_b, \quad \tilde{k}_2 = \epsilon \hat{k}_2, \quad \tilde{d} = \epsilon \hat{d}, \quad \tilde{c}_r = \epsilon \hat{c}_r,$$

$$\chi = \epsilon, \quad q_j = \epsilon s_j, \quad \tilde{Q}_j = \epsilon \hat{Q}_j \quad \tilde{Q}_\phi = \epsilon \hat{Q}_\phi.$$

These relations lead to

$$\frac{d^2 s_j}{d\phi^2} + \hat{k}_0 s_j + \hat{d} \sin \phi_j + \tilde{e}\frac{d\nu_1}{d\phi} + \epsilon \left[2\nu_1 \frac{d^2 s_j}{d\phi^2} + \frac{d\nu_1}{d\phi}\frac{ds_j}{d\phi} \right.$$

$$\left. + \hat{c}_b \frac{ds_j}{d\phi} + \hat{k}_2 \cos \phi_j s_j + \tilde{e}\nu_1 \frac{d\nu_1}{d\phi} \right] = \hat{Q}_j, \quad \text{(B.4)}$$

$$\frac{d\nu_1}{d\phi} + \hat{c}_r + \epsilon \left[\nu_1 \frac{d\nu_1}{d\phi} + \hat{c}_r \nu_1 + \epsilon \sum_{k=1}^{3} \tilde{e} \frac{d^2 s_k}{d\phi^2} \right] = \hat{Q}_\phi. \tag{B.5}$$

Note that ν_1 stands for the small oscillations from the mean speed. Therefore speed variations introduced by the external forces $(\hat{Q}_\phi - \hat{c}_r)$ can be considered as a variation in the mean speed, and can be omitted from the ν_1 equation.

The blade and rotor equations can not be decoupled at this stage. Instead a first order multiple scales analysis can be applied directly. Writing the equations in ψ domain, one can find

$$s_j'' + s_j + \frac{\tilde{e}}{p_1} \nu_1' = F_j - \delta \sin \phi_j + \epsilon \left[2\nu_1 s_j'' + \nu_1' s_j' + \frac{\hat{c}_b}{p_1} s_j' + \frac{\hat{k}_2}{\hat{k}_0} \cos \phi_j s_j + \frac{\tilde{e}}{p_1} \nu_1 \nu_1' \right], \tag{B.6}$$

$$\nu_1' = -\epsilon \left[\nu_1 \nu_1' + \frac{\hat{c}_r}{p_1} \nu_1 + \epsilon \sum_{k=1}^{3} \tilde{e} p_1 s_k'' \right], \tag{B.7}$$

where $F_j = \frac{\hat{Q}_j}{\hat{k}_0}$ and $\delta = \frac{\hat{d}}{\hat{k}_0}$. To apply the method of multiple scales, one can write $s_j = s_{j0} + \epsilon s_{j1}$ and $\nu_1 = \nu_{10} + \epsilon \nu_{11}$.

The ϵ^0 and ϵ^1 equations are:

ϵ^0 :

$$D_0^2 s_{j0} + s_{j0} + \frac{\tilde{e}}{p_1} D_0 \nu_{10} = F_{j0} - \delta \sin \left(r_1 \psi_0 + \frac{2\pi}{3} \right), \tag{B.8}$$

$$D_0 \nu_{10} = 0, \tag{B.9}$$

ϵ^1 :

$$D_0^2 s_{j1} + 2D_0 D_1 s_{j0} + s_{j1} + \frac{\tilde{e}}{p_1}(D_0 \nu_{11} + D_1 \nu_{10}) + D_0 \nu_{10} D_0 s_{j0}$$

$$= -2\nu_{10} D_0^2 s_{j0} - \frac{\hat{c}_b}{p_1} D_0 s_{j0} - \frac{\hat{k}_2}{\hat{k}_0} \cos{(r_1 \psi_0 + \frac{2\pi}{3})} s_{j0} - \frac{\tilde{e}}{p_1} \nu_{10} D_0 \nu_{10} \qquad (B.10)$$

$$D_0 \nu_{11} = -D_1 \nu_{10} - \nu_{10} D_0 \nu_{10} - \frac{\hat{c}_r}{p_1} \nu_{10} - \tilde{e} p_1 \sum_{k=1}^{3} D_0^2 s_{k0}. \qquad (B.11)$$

Equation (B.9) implies that ν_{10} is not a function of ψ_0, it is only a function of ψ_1 ($\nu_{10} = \nu_{10}(\psi_1)$ and $D_0 \nu_{10} = 0$). This leads to $\frac{\tilde{e}}{p_1} D_0 \nu_{10}$ term to drop off from the Equation (B.8). Therefore the leading order s_j equation, as well as the solution, are the same as those in Chapter 3. Also the Equation (B.11) reduces to

$$D_0 \nu_{11} = -D_1 \nu_{10} - \frac{\hat{c}_r}{p_1} \nu_{10} - \tilde{e} p_1 \sum_{k=1}^{3} D_0^2 s_{k0}. \qquad (B.12)$$

Integrating both sides, one can obtain

$$\nu_{11} = (-D_1 \nu_{10} - \frac{\hat{c}_r}{p_1} \nu_{10}) \psi_0 - \tilde{e} p_1 \sum_{k=1}^{3} \int D_0^2 s_{k0} \, d\psi_0. \qquad (B.13)$$

The terms that are multiplied by ψ_0 can lead to unbounded ν_{10} solution. Equating these terms (i.e. secular terms) to 0, the following equation for ν_{10} is found.

$$D_1 \nu_{10} = -\frac{\hat{c}_r}{p_1} \nu_{10}, \qquad (B.14)$$

which has a solution of the form: $\nu_{10} = h e^{-\frac{\hat{c}_r}{p_1} \psi_1}$. Therefore ν_{10} decays with time (or rotor angle), and in the steady state it goes to 0. So, the assumption made in Chapter 3 is legitimate.

APPENDIX C

A REVIEW ON DYNAMIC STALL MODELS

The aerodynamic loads (lift, drag and moment) are functions of the relative wind speed and the angle of attack, the angle between the chord of the blade cross-section and the relative wind velocity. In terms of the blade parameters, the lift force can be written as

$$F_L = \frac{1}{2}c_L\rho V^2 cL, \tag{C.1}$$

where ρ is air density, V is the relative wind speed, c is the chord length, L is the length of the blade and c_L is lift coefficient, which is a function of angle of attack, airfoil shape, air compressibility etc. For small angles of attack, the lift force usually increases with the angle. However, at a critical angle of attack (i.e. stall angle), it drops dramatically. This phenomenon is called aerodynamic stall, shown in Figure C.1.
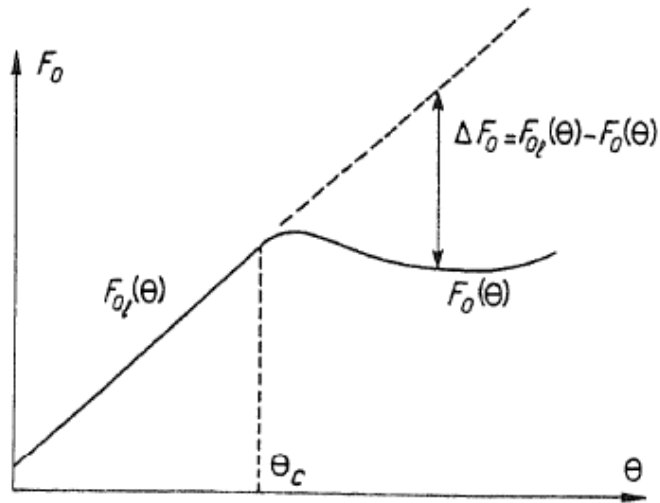

Figure C.1 A representative plot showing stall phenomenon [2].

C.1 Static Stall

When the angle of attack changes slowly, and there are no oscillations, static stall occurs. In this case, the lift coefficient is a direct function of the angle of attack as shown in Figure C.1. The relation can be determined by fitting a mathematical model to the lift data obtained from static tests. Static stall models can be used for systems in which the angle of attack varies quasi-statically.

C.2 Dynamic Stall

In a wind turbine blade, the angle of attack changes rapidly due to variations in angular speed, pitching motion and the vibrations of the blade. Rapid variations in angle of attack make lift force history dependent, meaning that a hysteresis occurs in lift force curve between increasing and decreasing angle of attack cases, as shown in Figure C.2. To model the lift force in dynamic stall conditions, semi-empirical methods are widely used [2, 4, 63]. These methods require experiments in different ranges of angle of attack and a mathematical model to define the behavior of the empirical lift curves.

C.3 ONERA's Dynamic Stall Model

This model is developed by French Aerospace Lab ONERA [2], and here is a summary given.

The model is used for helicopter blades in forward flight where the relative velocity can be separated into two parts $\underline{v} = \underline{v}_0 + \underline{v}_1$; average rotor speed (constant) and variations due to oscillations, blade flap and changes in the rotor speed [2].

The motion of the airfoil is defined by three functions; the angle of attack $\alpha(\tau)$, the pitch rate $\dot{\theta}(\tau)$ and the velocity ratio $\sigma(\tau) = v/v_0$, where τ is reduced time, $\tau = 2|\underline{v_0}|t/c$. A diagram showing these parameters is given in Figure C.3. The velocity ratio is directly proportional to Mach number, and accounts for compressibility effects. The lift, drag and
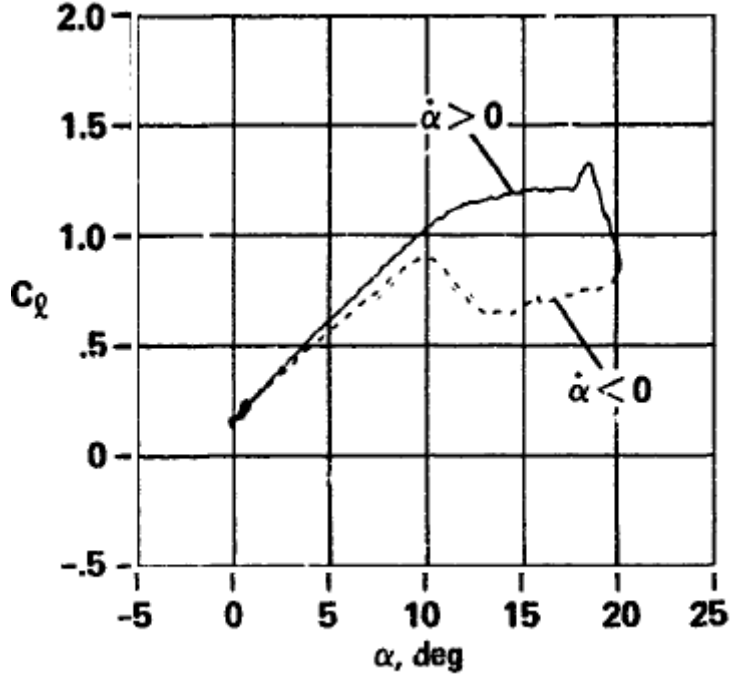
Figure C.2 A representative figure showing dynamic stall [3].

moment coefficients are given as
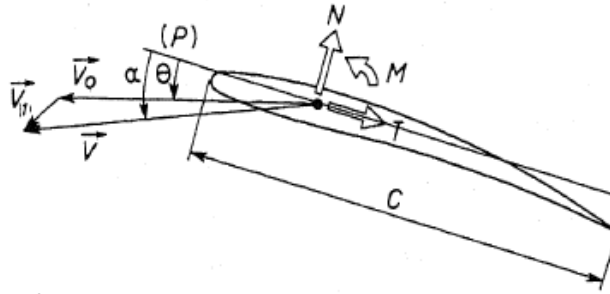
Figure C.3 Airfoil diagram used in ONERA's model [2].

$$\text{Normal} \quad \text{lift} \quad \text{coefficient}: \quad c_L = \frac{N}{\frac{1}{2}\rho|v|^2 cL} \tag{C.2}$$

The coefficient depends on the time history of σ, α, $\dot{\theta}$ and their successive derivatives. To introduce the time history effects, the behavior of coefficients are expressed with a differential equation, as

$$A_L(c_L, \sigma, \alpha, \dot{\theta}, \dot{c_L}, \dot{\sigma}, \dot{\alpha}, \ddot{\theta}, \ldots) = 0. \tag{C.3}$$

96

According to the experience acquired at ONERA

- Unsteady movements of an airfoil are limited either in frequency or in amplitude. It is assumed $\dot{\sigma}, \dot{\alpha}, \dot{\theta}, \dot{c}_L$, and their higher derivatives are "small".

- In most cases, c_L deviates only slightly from its static characteristics c_{L0}.

Admitting A_L is differentiable, Eq. (C.3) can be written as

$$A_L(P_0) + \sum_k \left[A_{Lc_L}(c_L - c_{L0}) + A_{L\dot{c}_L}\dot{c}_L + \ldots \right] + A_{L\dot{\theta}}\dot{\theta} + A_{L\dot{\alpha}}\dot{\alpha} + A_{L\dot{\sigma}}\dot{\sigma} + \ldots = 0, \quad \text{(C.4)}$$

where $P_0(c_{L0}, \sigma, \alpha, 0, \ldots)$ is the set of parameters in the static case, c_{L0} is the static (mean) value of c_L and $\dot{\sigma}_0 = \dot{\alpha}_0 = \dot{\theta}_0 = \ldots = 0$. A_{Lx} are partial derivatives as $A_{Lc_L} = \partial A_L / \partial c_L$, $A_{L\dot{c}_L} = \partial A_L / \partial \dot{c}_L$. $A_L(P_0) = 0$ equations define $c_{L0} = C_L(\alpha, \sigma)$, found from static wind tunnel tests. The stationary limit of A_L can be written as $A_L(P_0) = c_{L0} - C_L(\alpha, \sigma) = 0$. Rewriting Eq. (C.4), we get

$$\sum_{k=1}^{3} (A_{Lc_L} c_L + A_{L\dot{c}_L} \dot{c}_L + \ldots) = \sum_{k=1}^{3} A_{Lc_L} C_L - A_{L\dot{\theta}}\dot{\theta} - A_{L\dot{\alpha}}\dot{\alpha} - \ldots \quad \text{(C.5)}$$

Note that the coefficients vary with α and σ.

If the motion of an airfoil is imposed, $\dot{\theta}(\tau)$, $\alpha(\tau)$ and $\sigma(\tau)$ are known, and Eq. (C.5) can be written as

$$\sum_{k=1}^{3} (A_{Lc_L} c_L + A_{L\dot{c}_L} \dot{c}_L + \ldots) = S_r(\tau). \quad \text{(C.6)}$$

Presumably the coefficients are known from experiments, and thus $S_r(\tau)$ can be known explicitly. If A_L is such that A_{Lc_L}, $A_{L\dot{c}_L}$ are constants, then we have a linear forced ODE with constant coefficients.

The experience acquired at ONERA justifies

- The derivatives of α, σ and θ of order higher than two can be neglected.

- In general, one single real pole and two complex conjugate poles are sufficient to evaluate correctly the evolution of harmonic responses.

Then, Eq. (C.5) can be rewritten as

$$A_{Lc_L}c_L + A_{L\dot{c}_L}\dot{c}_L + A_{L\ddot{c}_L}\ddot{c}_L + A_{L\dddot{c}_L}\dddot{c}_L = A_{Lc_L}C_L(\sigma,\alpha) - A_{L\dot{\theta}}\dot{\theta} - A_{L\dot{\alpha}}\dot{\alpha}$$

$$- A_{L\dot{\sigma}}\dot{\sigma} - A_{L\ddot{\theta}}\ddot{\theta} - A_{L\ddot{\alpha}}\ddot{\alpha} - A_{L\ddot{\sigma}}\ddot{\sigma}. \quad \text{(C.7)}$$

$C_L(\alpha,\sigma)$ can be measured for various incidences. A least square curve fitting can be applied to find approximate analytical formula. This formula has two domains: linear and stall. Between the two, the continuity of C_L must be insured. Identification of the other coefficients requires unsteady flow testing.

C.3.1   ONERA's Model Applied on a Helicopter Airfoil Cross-section

This is an application of ONERA's model to a helicopter blade. All the work was conducted by NASA [3].

   A helicopter blade was tested under various mean incidences [3], oscillating with various amplitudes. The movement is defined by only the pitch angle ($\alpha = \theta$) and the constant speed ($\underline{v} = \underline{v_0}$). The lift coefficient is composed of two parts $c_L = c_{L1} + c_{L2}$. In the linear region, changes in the lift coefficient are smooth and can be represented by c_{L1}, dynamics of which is governed by a single negative real pole, whereas in stall region, rapid variations occur and c_{L2} is introduced which has two complex conjugate poles to represent the behavior. The equations governing the c_{L1} and c_{L2} are

$$\dot{c}_{L1} + \lambda c_{L1} = \lambda c_{L0L} + (\lambda\sigma + \delta)\dot{\theta} + \sigma\ddot{\theta}, \quad \text{(C.8)}$$

$$\ddot{c}_{L2} + 2\alpha\gamma\dot{c}_{L2} + \gamma^2(1+\alpha^2)c_{L2} = -\gamma^2(1+\alpha^2)\left(\Delta c_{L0} + c\frac{d\Delta c_{L0}}{d\tau}\right). \quad \text{(C.9)}$$

where c_{L0L} is the static lift in the linear region and $\Delta c_{L0} = c_{L0L} - c_{L0}$ is the deviation of real static lift curve from the linear lift. By doing tests at small incidences, the real negative pole $-\lambda$ can be found from the first equation. However, to find the poles of the second equation, $-\alpha\gamma \pm i\gamma$, dynamic testing in higher incidences is required.

C.4   A Semi-empirical Model by Larsen *et al.*

The model used by Larsen *et al.* was developed for fully attached and separated flow conditions separately, as shown in Figure C.4 [4]. They modeled the delay effects in separation and re-attachment with differential equations. The contribution of leading edge vortex and its movements were also taken into account.
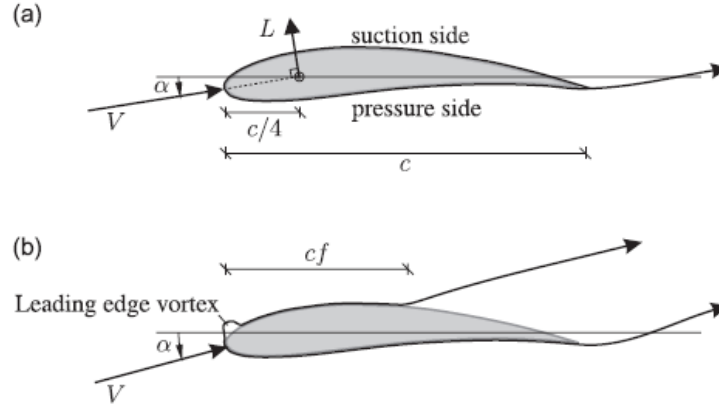
Figure C.4 Diagrams showing fully attached and separated flow conditions [4].

C.4.1   Stationary Lift and Separation

Under fully attached flow, the lift coefficient, c_{L0}, is linearized for small α, as

$$c_{L0} = \left.\frac{\partial c_L}{\partial \alpha}\right|_{\alpha_0} (\alpha - \alpha_0). \tag{C.10}$$

For separated flow, however, the lift coefficient deviates from c_{L0}, via the relation

$$c_L \simeq \left(\frac{1 + \sqrt{f}}{2}\right)^2 c_{L0}, \tag{C.11}$$

where f is the degree of attachment. For fully attached flow, $f = 1$ and $c_L = c_{L0}$, whereas for fully separated flow, $f = 0$ and $c_L = \frac{1}{4}c_{L0}$. Changes in degree of attachment results in changes in c_L via the relation

$$dc_L = \frac{1}{4}\left(1 + \frac{1}{\sqrt{f}}\right) c_{L0} df. \tag{C.12}$$

99

Notice that for fully separated flow conditions ($f = 0$), a very small change in f results in a very large variation in lift coefficient. To get rid of this singularity, the physical profile was mapped on a unit circle, as shown in Figure C.5.

Figure C.5 Mapping from airfoil profile to a unit circle [4].
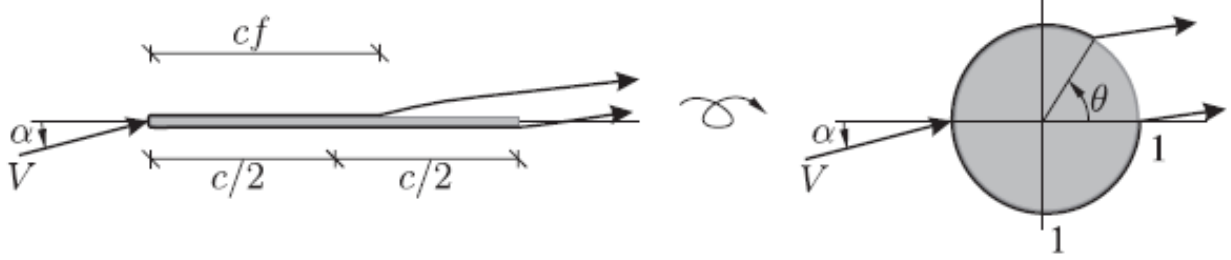
Instead of f, θ is used to define the degree of attachment. The conversion takes place as $2f = 1 + \cos\theta$. Inserting this into Eq. (C.11), we obtain

$$c_L \simeq \cos^4\left(\frac{\theta}{4}\right)c_{L0}. \tag{C.13}$$

C.4.2 Dynamic Lift

For fully attached flow, for a small change in angle of attack, $d\alpha$, a small separation occurs before the attaching is re-established. This constitutes a change in lift force. Hence, the increment dc_{L0} due to $d\alpha$ is not achieved instantaneously, This delay can be modeled via a delay function $\Phi(t)$,

$$dc_{L0,d}(t) = \Phi(t - \tau)dc_{L0}(\tau). \tag{C.14}$$

For incompressible flow, for a thin profile, half the increment is felt instantaneously. So, $\Phi(0) = \frac{1}{2}$ and $\Phi(\infty) = 1$. So, the linear dynamic lift coefficient for attached flow, can be written as

$$c_{L0,d}(t) = \int_{-\infty}^{t} \Phi(t - \tau)\dot{c}_{L0}(\tau)d\tau, \tag{C.15}$$

where the delay function can be expressed as $\Phi(t) = 1 - A_1e^{-\omega_1 t} - A_2e^{-\omega_2 t}$. The coefficients and exponents, A_1, A_2, ω_1 and ω_2 are profile dependent variables describing the time delay.

For a thin profile $A_1 + A_2 = \frac{1}{2}$, and ω_1 and ω_2 represent timescale for low and high frequency contributions, respectively.

$$\dot{c}_j(t) + \omega_j c_j(t) = A_j \dot{c}_{L0}(t) \quad j = 1, 2$$

and

$$c_{L0,d}(t) = c_{L0}(\alpha) - c_1(t) - c_2(t). \tag{C.16}$$

For separated flow, a step chance in α results in a change in θ. Yet, a time interval is observed during which the separation angle moves to its new stationary value. The dynamic attachment angle is governed by the equation

$$\dot{\theta}_d(t) = -\omega_3 \left(\theta_d(t) - \theta(\alpha) \right)$$

Then, the dynamic lift coefficient is

$$c_{L,d} \simeq \cos^4 \left(\frac{\theta_d}{4} \right) c_{L0,d}(t). \tag{C.17}$$

The experimental data indicates that leading edge separation generates a linearly increasing lift curve even at full separation. To model this linear lift curve, a correction term is added to $c_{L,d}(t)$.

$$\Delta c_L(t) = c_{L0,d}(t) - c_{L,d}(t)$$

At a certain angle α_v, the leading edge vortex detaches from the leading edge, and travels downstream over the profile. The traveling vortex builds up strength, and as it reaches the trailing edge, it stops, corresponding to $\Delta \dot{c}_L(t) = 0$ and a vortex with opposite circulation starts to develop at the trailing edge. The trailing edge vortex counteracts the leading edge vortex and the lift starts diminishing.

$$\dot{c}_{L,v}(t) + \omega_4 c_{L,v}(t) = \begin{cases} \Delta \dot{c}_L(t) & \text{for} \quad \alpha > \alpha_v \quad \text{and} \quad \dot{\alpha} > 0 \\ 0 & \text{otherwise} \end{cases} \tag{C.18}$$

and

$$c_L(t) = c_{L,d}(t) + c_{L,v}(t). \tag{C.19}$$

101

The equations governing the lift coefficients can be written in state variable form, as

$$\underline{\dot{z}}(t) = A\underline{z}(t) + \underline{b}_0(\alpha) + \underline{b}_1 \dot{c}_{L0}(t), \qquad (C.20)$$

where

$$\underline{z}(t) = \begin{pmatrix} c_1(t) \\ c_2(t) \\ \theta_d(t) \\ c_{L,v}(t) \end{pmatrix}, \quad A = \begin{bmatrix} -\omega_1 & 0 & 0 & 0 \\ 0 & -\omega_2 & 0 & 0 \\ 0 & 0 & -\omega_3 & 0 \\ 0 & 0 & 0 & -\omega_4 \end{bmatrix},$$

$$\underline{b}_0(\alpha) = \begin{pmatrix} 0 \\ 0 \\ \omega_3\theta(\alpha) \\ \Delta\dot{c}_L \mathrm{H}(\alpha_v - \alpha)\mathrm{H}(\dot{\alpha}) \end{pmatrix}, \quad \underline{b}_1 = \begin{pmatrix} A_1 \\ A_2 \\ 0 \\ 0 \end{pmatrix}.$$

C.5   Conclusions

Examples of semi empirical aerodynamic stall models are reviewed. ONERA's model was used on helicopter blades where the relative wind velocity is assumed to oscillate around a mean speed. The behavior of lift force is expressed via a third order differential equation, taking pitching motion and compressibility effects into account. To find the coefficients of the equation, the airfoil must be tested under steady and unsteady flow conditions. The model used by Larsen *et al.*, on the other hand, was applied to wind turbine blades. Since turbine blades operate at small speeds, compressibility effects are omitted. The mathematical model takes flow separation, leading edge vortex and delay effects into account. Larsen's model is simpler than ONERA's, and more suitable for wind turbines. One of the above methods can be used on an existing blade model to find the lift coefficient as a function of angle of attack.

BIBLIOGRAPHY

BIBLIOGRAPHY

[1] R. Wiser, L. Eric, T. Mai, J. Zayas, E. DeMeo, E. Eugeni, J. Lin-Powers, and R. Tusing. Wind vision: A New Era for Wind Power in the United States. *The Electricity Journal*, 28(9):120–132, 2015.

[2] C.T. Tran and D. Petot. Semi-empirical model for the dynamic stall of airfoils in view of the application to the calculation of responses of a helicopter blade in forward flight. *Vertica*, 23:35–53, 1980.

[3] K. W. McAlister, O. Lambert, and D. Petot. Application of the ONERA model of dynamic stall. Technical report, DTIC Document, 1984.

[4] J.W. Larsen, S.R.K. Nielsen, and S. Krenk. Dynamic stall model for wind turbine airfoils. *Journal of Fluids and Structures*, 23(7):959–982, 2007.

[5] Monthly energy review. U.S. Energy Information Administration (EIA). Published online, 2015. `http://www.eia.gov/totalenergy/data/monthly/`.

[6] DOE/GO-102008-2578. *20% Wind Energy By 2030: Increasing wind energy's contribution to U.S. electricity supply.* U.S. Department of Energy, 2008.

[7] C. Lindenburg. Aeroelastic modelling of the LMH64-5 blade. *Energieonderzoek Centrum Nederland, 02-KL-083 , Petten, December*, 2002.

[8] J.M. Jonkman, S. Butterfield, W. Musial, and G. Scott. *Definition of a 5-MW reference wind turbine for offshore system development.* National Renewable Energy Laboratory Golden, CO, 2009.

[9] D.T. Griffith and T.D. Ashwill. The sandia 100-meter all-glass baseline wind turbine blade: Snl100-00. *Sandia National Laboratories, Albuquerque, Report No. SAND2011-3779*, 2011.

[10] P.J. Tavner, F. Spinato, G.J.W. Van Bussel, and E. Koutoulakos. Reliability of different wind turbine concepts with relevance to offshore application. In *Proceedings of European Wind Energy Conference, Brussels, Belgium, March*, 2008.

[11] V. Ramakrishnan and B.F. Feeny. In-plane nonlinear dynamics of wind turbine blades. In *ASME 2011 International Design Engineering Technical Conferences and Computers and Information in Engineering Conference*, pages 761–769. American Society of Mechanical Engineers, 2011.

[12] J. Cheng, H. Xu, and A. Yan. Frequency analysis of a rotating cantilever beam using assumed mode method with coupling effect. *Mechanics based design of structures and machines*, 34(1):25–47, 2006.

[13] B. Dawson. Coupled bending-bending vibrations of pre-twisted cantilever blading treated by the rayleigh-ritz energy method. *Journal of Mechanical Engineering Science*, 10(5):381–388, 1968.

[14] E. Dokumaci. An exact solution for coupled bending and torsion vibrations of uniform beams having single cross-sectional symmetry. *Journal of Sound and Vibration*, 119(3):443–449, 1987.

[15] R.E.D. Bishop, S.M. Cannon, and S. Miao. On coupled bending and torsional vibration of uniform beams. *Journal of Sound and Vibration*, 131(3):457–464, 1989.

[16] D.W. Lobitz and P.S. Veers. Aeroelastic behavior of twist-coupled hawt blades. *American Institute of Aeronautics and Astronautics, Albuquerque, NM*, 1998.

[17] C.G. Cooley and R.G. Parker. Vibration of spinning cantilever beams undergoing coupled bending and torsional motion. In *ASME 2013 International Design Engineering Technical Conferences and Computers and Information in Engineering Conference*, pages V008T13A068–V008T13A068. American Society of Mechanical Engineers, 2013.

[18] D. H. Hodges and E.H. Dowell. *Nonlinear equations of motion for the elastic bending and torsion of twisted nonuniform rotor blades*. National Aeronautics and Space Administration, TN D-7818, 1974.

[19] B. S. Kallesøe. Equations of motion for a rotor blade, including gravity, pitch action and rotor speed variations. *Wind Energy*, 10(3):209–230, 2007.

[20] G.C. Larsen, M. H. Hansen, A. Baumgart, and I. Carlén. Modal analysis of wind turbine blades. Technical report, Risø–R–1181, 2002.

[21] Y. Zhiquan, M. Haomin, B. Nengsheng, C. Yan, and D. Kang. Structure dynamic analysis of a horizontal axis wind turbine system using a modal analysis method. *Wind engineering*, 25(4):237–248, 2001.

[22] D.L. Laird, F.C. Montoya, and D.J. Malcolm. Finite element modeling of wind turbine blades. In *43rd AIAA Aerospace Sciences Meeting and Exhibit*, volume 6, pages 10–13, 2005.

[23] M.H. Hansen. Aeroelastic stability analysis of wind turbines using an eigenvalue approach. *Wind Energy*, 7(2):133–143, 2004.

[24] G. Bir. Multiblade coordinate transformation and its application to wind turbine analysis. In *ASME Wind Energy Symposium*, 2008.

[25] M.R.M. Crespo da Silva. Nonlinear flexural-flexural-torsional-extensional dynamics of beams. i. formulation. *International Journal of Solids and Structures*, 24(12):1225–1234, 1988.

[26] A.S. Alsuwaiyan and S.W. Shaw. Performance and dynamic stability of general-path centrifugal pendulum vibration absorbers. *Journal of Sound and Vibration*, 252(5):791–815, 2002.

[27] W.K. Wilson. *Pratical Solution of Torsional Vibration Problems Chapter XXX*. Chapman & Hall, London, 1968.

[28] B.J. Olson, S.W. Shaw, C. Shi, C. Pierre, and R.G. Parker. Circulant matrices and their application to vibration analysis. *Applied Mechanics Reviews*, 66(4):040803, 2014.

[29] C.P. Chao, S.W. Shaw, and C.T. Lee. Stability of the unison response for a rotating system with multiple tautochronic pendulum vibration absorbers. *Journal of Applied Mechanics*, 64(1):149–156, 1997.

[30] C.P. Chao, C.T. Lee, and S.W. Shaw. Non-unison dynamics of multiple centrifugal pendulum vibration absorbers. *Journal of Sound and Vibration*, 204(5):769–794, 1997.

[31] T.M. Theisen. Gravity's effect on centrifugal pendulum vibration absorbers. Thesis, Michigan State University, 2011.

[32] V. Ramakrishnan and B.F. Feeny. Resonances of a forced Mathieu equation with reference to wind turbine blades. *Journal of Vibration and Acoustics*, 134(6):064501, 2012.

[33] G. Acar and B.F. Feeny. Linear modal analysis of a horizontal-axis wind turbine blade. In *Special Topics in Structural Dynamics*, volume 6, pages 125–131. Springer, 2015.

[34] T. Inoue, Y. Ishida, and T. Kiyohara. Nonlinear vibration analysis of the wind turbine blade (occurrence of the superharmonic resonance in the out of plane vibration of the elastic blade). *Journal of Vibration and Acoustics*, 134(3):031009, 2012.

[35] L. Ruby. Applications of the Mathieu equation. *American Journal of Physics*, 64(1):39–44, 1996.

[36] Y. Li, S. Fan, Z. Guo, J. Li, L. Cao, and H. Zhuang. Mathieu equation with application to analysis of dynamic characteristics of resonant inertial sensors. *Communications in Nonlinear Science and Numerical Simulation*, 18(2):401–410, 2013.

[37] J.F. Rhoads, N.J. Miller, S.W. Shaw, and B.F. Feeny. Mechanical domain parametric amplification. *Journal of Vibration and Acoustics*, 130(6):061006, 2008.

[38] A.H. Nayfeh and D.T. Mook. *Nonlinear Oscillations*. John Wiley & Sons, New York, 2008.

[39] J.H. Taylor and K.S. Narendra. Stability regions for the damped Mathieu equation. *SIAM Journal on Applied Mathematics*, 17(2):343–352, 1969.

[40] D. Younesian, E. Esmailzadeh, and R. Sedaghati. Existence of periodic solutions for the generalized form of Mathieu equation. *Nonlinear Dynamics*, 39(4):335–348, 2005.

[41] W. Thomson. *Theory of Vibration with Applications*. CRC Press, Englewood Cliffs, 1996.

[42] A.H. Nayfeh. *Perturbation Methods*. John Wiley & Sons, New York, 2008.

[43] H. Benaroya and M.L. Nagurka. *Mechanical Vibration: Analysis, Uncertainties, and Control*. CRC Press, Englewood Cliffs, 2011.

[44] H.L. Turrittin. Asymptotic expansions of solutions of systems of ordinary linear differential equations containing a parameter. In *Contributions to the Theory of Nonlinear Oscillations, vol. II*, pages 81–116. Princeton University Press Princeton, 1952.

[45] R.H. Rand. On the stability of Hill's equation with four independent parameters. *Journal of Applied Mechanics*, 36(4):885–886, 1969.

[46] Y. Ishida, T. Inoue, and K. Nakamura. Vibration of a wind turbine blade (theoretical analysis and experiment using a single rigid blade model). *Journal of Environment and Engineering*, 4(2):443–454, 2009.

[47] H. Ecker. Parametric excitation in engineering systems. In *20th International Congress of Mechanical Engineering, COBEM*, pages 15–20, 2009.

[48] H. Ecker. Beneficial effects of parametric excitation in rotor systems. In *IUTAM Symposium on Emerging Trends in Rotor Dynamics*, pages 361–371. Springer, 2011.

[49] K. Klotter and G. Kotowski. Über die Stabilität der Lösungen Hillscher Differentialgleichungen mit drei unabhängigen Parametern. *ZAMM-Journal of Applied Mathematics and Mechanics/Zeitschrift für Angewandte Mathematik und Mechanik*, 23(3):149–155, 1943.

[50] A. Sofroniou and S. Bishop. Dynamics of a parametrically excited system with two forcing terms. *Mathematics*, 2(3):172–195, 2014.

[51] M.S. Allen, M.W. Sracic, S. Chauhan, and M.H. Hansen. Output-only modal analysis of linear time-periodic systems with application to wind turbine simulation data. *Mechanical Systems and Signal Processing*, 25(4):1174–1191, 2011.

[52] R. Rand. Lecture notes on nonlinear vibrations. Published online, 2012. `http://www.math.cornell.edu/~rand/randdocs/nlvibe52.pdf`.

[53] M.J. Ward. Lecture notes on basic Floquet theory. Published online, 2010. `http://www.emba.uvm.edu/~jxyang/teaching/`.

[54] N.W. McLachlan. *Theory and application of Mathieu functions*. Dover, New York, 1961.

[55] A. Peterson and M. Bibby. *Accurate Computation of Mathieu Functions*. Morgan & Claypool Publishers, San Rafael, 2013.

[56] D.B. Hodge. *The calculation of the eigenvalues and eigenfunctions of Mathieu's equation*, volume 1937. National Aeronautics and Space Administration, 1972.

[57] J.D. Anderson. *Aircraft Performance and Design*, volume 1. WCB/McGraw-Hill Boston, 1999.

[58] E.H. Dowell, R. Clark, D. Cox, H.C. Curtiss Jr., J.W. Edwards, K.C. Hall, D.A. Peters, R. Scanlan, E. Simiu, F. Sisto, and T.W. Strganac. *A Modern Course In Aeroelasticity*, volume 3. Springer New york, 2004.

[59] W.J. McCroskey, K.W. McAlister, L.W. Carr, S.L. Pucci, O. Lambert, and R.F. Indergrand. Dynamic stall on advanced airfoil sections. *Journal of the American Helicopter Society*, 26(3):40–50, 1981.

[60] T. Theodorsen. *General theory of aerodynamic instability and the mechanism of flutter*. National Advisory Committee for Aeronautics, Report 496, 1949.

[61] C.E. Lan. A quasi-vortex-lattice method in thin wing theory. *Journal of Aircraft*, 11(9):518–527, 1974.

[62] D.A. Peters, D.D. Boyd, and C.J. He. Finite-state induced-flow model for rotors in hover and forward flight. *Journal of the American Helicopter Society*, 34(4):5–17, 1989.

[63] J.G. Leishman and T.S. Beddoes. A semi-empirical model for dynamic stall. *Journal of the American Helicopter Society*, 34(3):3–17, 1989.

[64] H.H. Yoo and S.H. Shin. Vibration analysis of rotating cantilever beams. *Journal of Sound and Vibration*, 212(5):807–828, 1998.

[65] J.R. Banerjee. Free vibration of centrifugally stiffened uniform and tapered beams using the dynamic stiffness method. *Journal of Sound and Vibration*, 233(5):857–875, 2000.

[66] M.A. Crisfield. *Nonlinear finite element analysis of solids and structures. Volume 1: Essentials*. Wiley, New York, NY, 1991.

[67] K.V. Avramov, C. Pierre, and N. Shyriaieva. Flexural-flexural-torsional nonlinear vibrations of pre-twisted rotating beams with asymmetric cross-sections. *Journal of Vibration and Control*, 13(4):329–364, 2007.

[68] M.H. Sadd. *Elasticity: theory, applications, and numerics*. Academic Press, 2009.

[69] W. Weaver Jr., S.P. Timoshenko, and D.H. Young. *Vibration Problems in Engineering*. John Wiley & Sons, New York, 1990.

[70] L. Meirovitch. *Principles and techniques of vibrations*, volume 1. Prentice Hall New Jersey, 1997.

[71] V. Ramakrishnan and B.F. Feeny. Second order perturbation analysis of a forced nonlinear Mathieu equation. In *ASME 2012 International Design Engineering Technical Conferences and Computers and Information in Engineering Conference*, pages 1073–1082. American Society of Mechanical Engineers, 2012.

[72] G.S. Bir and F. Oyague. *Estimation of blade and tower properties for the gearbox research collaborative wind turbine.* National Renewable Energy Laboratory, TP-500-42250, 2007.

[73] S. Chauhan, M.H. Hansen, and D. Tcherniak. Application of operational modal analysis and blind source separation/independent component analysis techniques to wind turbines. In *Proceedings of XXVII International Modal Analysis Conference, Orlando (FL), USA*, 2009.

[74] L. Meirovitch. *Computational methods in structural dynamics*, volume 5. Springer Science & Business Media, 1980.

[75] J.J. Stoker. *Nonlinear Vibrations in Mechanical and Electrical Systems*, volume 2. Interscience Publishers, New York, 1950.

[76] G. Acar and B.F. Feeny. Approximate general responses of multi-degree-of-freedom systems with parametric stiffness. In *Special Topics in Structural Dynamics*, volume 6, pages 211–219. Springer, 2016.

[77] P. Hagedorn. *Non-linear Oscillations.* Clarendon Press, Oxford, 1988.

[78] J.K. Hale. *Oscillations in Nonlinear Systems.* McGraw-Hill, New York, 1963.

[79] C. Hayashi. *Nonlinear Oscillations in Physical Systems.* Princeton University Press, Princeton, 2014.

[80] G. Schmidt and A. Tondl. *Non-linear Vibrations*, volume 66. Cambridge University Press, Cambridge, 1986.

[81] J.P. Den Hartog. *Mechanical Vibrations.* Dover, New York, 1985.

[82] W. Magnus and S. Winkler. *Hill's Equation.* Dover, New York, 1979.

[83] E.T. Whittaker. On the general solution of Mathieu's equation. *Proceedings of the Edinburgh Mathematical Society*, 32:75–80, 1913.

[84] J.M. Malasoma, C.H. Lamarque, and L. Jezequel. Chaotic behavior of a parametrically excited nonlinear mechanical system. *Nonlinear Dynamics*, 5(2):153–160, 1994.

[85] R. Coisson, G. Vernizzi, and X. Yang. Mathieu functions and numerical solutions of the mathieu equation. In *Open-source Software for Scientific Computation (OSSC), 2009 IEEE International Workshop on*, pages 3–10. IEEE, 2009.

[86] T Insperger and G Stépán. Stability chart for the delayed Mathieu equation. *Proceedings of the Royal Society of London A: Mathematical, Physical and Engineering Sciences*, 458(2024):1989–1998, 2002.

[87] T. Insperger and G. Stépán. Stability of the damped Mathieu equation with time delay. *Journal of Dynamic Systems, Measurement, and Control*, 125(2):166–171, 2003.

[88] G. Acar and B.F. Feeny. Floquet-based analysis of general responses of the Mathieu equation. *Journal of Vibration and Acoustics*, 138(4):041017, 2016.

[89] F. Afzali, O. Kapucu, and B.F. Feeny. Vibrational analysis of vertical axis wind turbine blades. In *ASME 2016 International Design Engineering Technical Conferences and Computers and Information in Engineering Conference*. American Society of Mechanical Engineers, 2016.